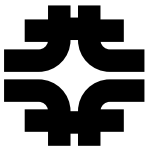

Fermi National Accelerator Laboratory

FERMILAB-FN-660
FERMILAB-EOI-1997-01

BTeV: An Expression of Interest for a Heavy Quark Program at C0

A. Santoro et al.

Fermi National Accelerator Laboratory
P.O. Box 500, Batavia, Illinois 60510

September 1997

Operated by Universities Research Association Inc. under Contract No. DE-AC02-76CH03000 with the United States Department of Energy

Disclaimer

Distribution

BTeV: An Expression of Interest for a Heavy Quark Program at C0 †

May 18, 1997

A. Santoro
Centro Brasileiro de Pesquisas Fisicas, Rua Dr. Xavier Sigaud 150 - URCA, BR-22290-180 Rio de Janeiro, RJ, Brasil

S. Mani
University of California at Davis, Experimental High Energy Group, Davis, CA 95616-8677, USA

M. Procario, J. Russ
Carnegie Mellon University, Pittsburgh, PA 15213, USA

J. Cumalat
University of Colorado, High Energy Physics, Campus Box 390, Boulder, CO 80309, USA

J. A. Appel, C. N. Brown, J. Butler, H. Cheung, D. Christian, I. Gaines, P. Garbincius, L. Garren, N. M. Gelfand, P. Kasper, P. H. Kasper, R. Kutschke, S. W. Kwan, P. Lebrun, P. McBride, L. Stutte, J. Yarba
Fermilab, PO Box 500, Batavia, IL 60510, USA

P. Avery, M. Lohner
University of Florida, Gainesville, FL 32611, USA

R. A. Burnstein, D. M. Kaplan, L. M. Lederman, H. A. Rubin, V. J. Smith
Illinois Institute of Technology, Chicago, IL 60616, USA

M. Selen, J. Wiss
University of Illinois at Urbana-Champaign, High Energy Physics, 441 Loomis Lab. of Physics, 1110 W. Green St., Urbana, IL 61801-3080, USA

D. Menasce, L. Moroni, D. Pedrini, S. Sala
INFN and University of Milano, Italy

G. Boca, G. Liguori, P. Torre
Dipartimento di Fisica Nucleare e Teorica, Universita' di Pavia and INFN, Sez. di Pavia, Italy

Y. Kubota
University of Minnesota, High Energy Physics, Tate Lab of Physics, 116 Church St. S.E., Minneapolis, MN 55455, USA

T. Y. Chen
Nanjing University, Dept. of Physics, Nanjing 210008, China

V. Papavassiliou
New Mexico State University

M. Alam, S. Timm
State University of New York at Albany, Dept. of Physics, Albany, NY 12222, USA

†Spokespersons: Joel Butler and Sheldon Stone

P. Maas
Northwestern University, Dept. of Physics, 2145 Sheridan Road, Evanston, IL 60208, USA
K. Honscheid, H. Kagan, A. Wolf
Ohio State University, HEP Group, Dept. of Experimental or Theoretical Physics, Smith Lab, 174 W. 18th Ave., Columbus, OH 43210, USA
W. Selove, K. Sterner
University of Pennsylvania, Philadelphia, PA 19104, USA
A. Lopez
University of Puerto Rico, Mayaguez, Puerto Rico
X. Q. Yu
University of Science and Technology of China, Dept. of Modern Physics, Joint Institute for High Energy Physics, Hefei, Anhui 230027, China
M. He
Shandong University, High Energy Physics Group, Jinan, Shandong 250100, China
S. Shapiro (emeritus)
Stanford Linear Accelerator Center, PO Box 4349, Stanford, CA 94309, USA
M. Artuso, M. Goldberg, T. Skwarnicki, S. Stone
Syracuse University, 201 Physics Bldg., Syracuse, NY 13244-1130, USA
T. Handler
University of Tennessee, Knoxville, TN 37996-1200, USA
A. Napier
Tufts University, High Energy Physics, Science & Technology Center, 4 Colby St., Medford, MA 02155, USA
D. D. Koetke
Valparaiso University, Neils Science Center, Valparaiso, IN 46383, USA
P. Sheldon, M. Webster
Vanderbilt University, Department of Physics and Astronomy, Nashville, TN 37235, USA
M. Sheaff
University of Wisconsin, Phenomenology Inst., Dept. of Physics, 1150 University Ave., Madison, WI 53706, USA
J. Slaughter
Yale University, High Energy Physics, 219 Prospect St., 554 JWG, Box 6666, New Haven, CT 06511, USA

Contents

1 Opportunities for Heavy Quark Physics in C0 After the Year 2000

BTeV is a program whose long term goal is to carry out precision studies of CP violation, mixing, and rare decays of b and c quarks in the forward direction at the Fermilab Tevatron collider. Using the new Main Injector, now under construction, the collider will produce on the order of 10^{11} b hadrons and 10^{12} c hadrons in 10^7 seconds of running at a luminosity of 10^{32}. This is to be compared with e^+e^- colliders operating at the $\Upsilon(4S)$ resonance. These machines will produce 6×10^7 B mesons in 10^7 seconds at their design luminosities of 3×10^{33}, or three orders of magnitude less than the Tevatron [1].

The next generation of b experiments, which includes BaBar at SLAC, BELLE at KEK, CLEO III at CESR, CDF and D0 at Fermilab, and HERA-B at DESY, are likely to detect CP violation in B meson decays. While they may open up this area of investigation they are unlikely to answer all the important questions. A further generation (or several) of high precision b and charm experiments will be needed. This stage of heavy quark physics will have to be carried out at hadron colliders because they will be the only machines that can produce enough bottom and charmed hadrons to achieve the required precision.

We are offering this Expression Of Interest to develop a program which is well-suited to make precision studies of b and c decays in the Tevatron at high rapidity. The program we propose will be carried out in the new C0 experimental hall to be built at Fermilab. The program is an aggressive one with ambitious goals. However, it can develop in stages that take into account the resources that the lab has available, the rate at which R&D into the key technologies of the experiment can be accomplished, and the impact on the rest of the Fermilab program.

The outline of this EOI is as follows. The remainder of section 1 presents the main physics goals of BTeV, describes the kinematics of forward b production and briefly discusses the advantages of the forward direction for heavy quark studies. It then goes on to review the physics issues in bottom and charm that need to be studied. Section 2 presents the proposed detector and compares it with a possible competitor, LHC-B. Section 3 describes a program for developing this detector in stages so that detector development and physics measurements can be interleaved in a manner which promotes the experiment's final goal while providing significant physics and useful experience in operating the detector along the way. Section 4 presents the results of recent simulations of the sensitivities for carrying out a variety of bottom and charm studies. The results of this section, which represent a status report on work in progress, can be used to begin to compare the physics reach of BTeV with the other efforts with which it might compete – CDF and D0 in its early years and LHC-B later on. Section 5 describes the R&D required to develop the key detector components. Section 6 presents some information on costs, schedules, and manpower to carry out the R&D and the construction of the detector.

Earlier studies of possible dedicated collider b-physics experiments at Fermi-

lab, BCD and P845 (P. Schlein), came to much the same conclusions concerning the large advantages of working in the forward direction.

1.1 The Main Physics Goals of BTeV

Below, we review the important questions in the physics of bottom and charm that should be addressed by experiments over the next decade. Some key measurements, for example $\sin 2\beta$ and some rare decays, may well be measured before BTeV goes into operation. Most of the program, however, will not have been done, and even where initial measurements have been made, more precise measurements are justified by the goal of looking for deviations from the Standard Model. Such deviations, even if small, could be crucial clues in discovering new physics which goes beyond the Standard Model.

People have been thinking about CP violation in heavy quark decays for a long time. Initial optimism that a few measurements would resolve all issues has given way to a more realistic view of the situation. Theoretical complexities make the interpretation of some of the 'benchmark modes' more difficult than first believed. This is especially true for the measurement of $\sin 2\alpha$, where recent experimental information on the large apparent size of $B^o \to K\pi$ relative to $B^o \to \pi\pi$ brings three pieces of bad news [83]: that the branching fraction for $\pi\pi$ may be smaller than people had hoped; that the importance of particle identification to separate the two states where their signals overlap is critical; and that the interpretation of the results may be complicated by a large interference with the Penguin diagram. Moreover, the measurement of γ requires a very high luminosity and will probably be unattainable in the B-factories, HERA-B, or CDF and D0, at least in the current round of experiments. The B_s mixing parameter is large which means that excellent time resolution and large statistics are needed to measure it. All this suggests that the long term future of these investigations lies with hadron collider experiments which provide the much higher rates of b hadrons to work with. We believe that a dedicated forward spectrometer of the kind described below will out-perform the general purpose central region detectors at hadron colliders.

Finally, we want to emphasize that BTeV, because of its powerful trigger and vertexing capability, is a better charm experiment than any current or planned. Since it is important to try to find phenomena which are not expected within the Standard Model, it is essential that searches be undertaken for CP violation, mixing, and rare decays of charm, where the Standard Model predicts very low rates and where a signal from new physics may therefore stand out clearly.

Below, we list some of the measurements that we believe that BTeV can make as well if not better than any other bottom or charm experiment that will be running during this period.

1.1.1 Physics Goals For B's

Here we briefly list the main physics goals for studies of the b quark.

- Precision measurements of B_s mixing, both the time evolution x_s and the lifetime difference, $\Delta\Gamma$, between the positive CP and negative CP final states.

- Measurement of the "CP violating" angles α and γ. We will use $B^o \to \pi^+\pi^-$ for α and measure γ using several different methods including $B^+ \to D^o K^+$, $B^+ \to \overline{D}^o K^+$, where the D^o can decay directly or via a doubly Cabibbo suppressed decay mode. We also need to measure the conjugate B^- decay modes [27, 28].

- Search for rare final states such as $K\mu^+\mu^-$, $K^*\mu^+\mu^-$, $\pi\mu^+\mu^-$, $\rho\mu^+\mu^-$, and similar states with electrons, which could result from new high mass particles coupling to b quarks.

- We assume that the CP violating angle β will have already been measured using $B^o \to \psi K_s$, but we will be able to significantly reduce the error.

- Search for unexpectedly high asymmetries in places where the Standard Model predicts small CP asymmetries. The decay $B_s \to \psi\phi$ is an example.

1.1.2 The Main Physics Goals for charm

According to the standard model, charm mixing and CP violating effects should be "small." Thus charm provides an excellent place for non-standard model effects to appear. Specific goals are listed below.

- Search for mixing in D^o decay, by looking for both the rate of wrong sign decay, r_D and the width difference between positive CP and negative CP eigenstate decays, $\Delta\Gamma$. The current upper limit on r_D is 3.7×10^{-3}, while the standard model expectation is $r_D < 10^{-7}$ [29].

- Search for CP violation in D^o. Here we have the advantage over b decays that there is a large D^{*+} signal which tags the initial flavor of the D^o through the decay $D^{*+} \to \pi^+ D^o$. Similarly D^{*-} decays tag the flavor of inital $\overline{D}^o$. The current experimental upper limits on CP violating asymmetries are on the order of 10%, while the standard model prediction is about 0.1% [30].

- Search for direct CP violation in charm using D^+ and D_s^+ decays.

- Search for rare decays of charm, which if found would signal new physics.

1.1.3 Other b and charm Physics Goals

There are many other physics topics that can be addressed by BTeV. A short list is given here.

- Measurement of the $b\bar{b}$ production cross-section and correlations between the b and the $\bar{b}$ in the forward direction.

- Measurement of the B_c production cross-section and decays.

- The spectroscopy of b baryons.

- Precision measurement of V_{cb} using the baryonic decay mode $\Lambda_b \to \Lambda_c \ell^- \bar{\nu}$ and the usual mesonic decay modes.
- Precision measurement of V_{ub} using the baryonic decay mode $\Lambda_b \to p \ell^- \bar{\nu}$ and the usual mesonic decay modes.
- Measurement of the $c\overline{c}$ production cross-section and correlations between the c and the $\overline{c}$ in the forward direction.
- Precision measurement of V_{cd} and the form-factors in the decays $D \to \pi \ell^+ \nu$ and $D \to \rho \ell^+ \nu$.
- Precision measurement of V_{cs} and the form-factors in the decay $D \to K^* \ell^+ \nu$.

1.2 Characteristics of Hadronic b Production

It is customary to characterize heavy quark production in hadron collisions with the two variables p_t and η. The latter variable was first invented by those who studied high energy cosmic rays and is assigned the value

$$\eta = -ln\left(\tan\left(\theta/2\right)\right), \tag{1}$$

where θ is the angle of the particle with respect to the beam direction.

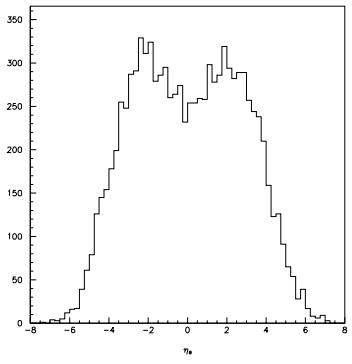

Figure 1: The B yield versus η.

According to QCD calculations of b quark production, the b's are produced "uniformly" in η and have a truncated transverse momentum, p_t, spectrum, characterized by a mean value approximately equal to the B mass [2]. The distribution in η is shown in Fig. 1.

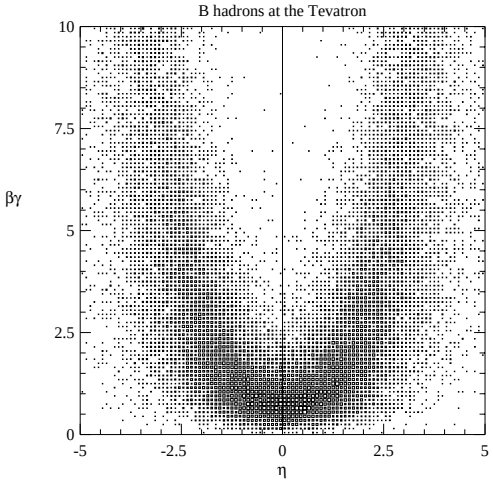

Figure 2: $\beta\gamma$ of the B versus η.

There is a strong correlation between the B momentum and η. Shown in

Fig. 2 is the $\beta\gamma$ of the B hadron versus η from Pythia at $\sqrt{s} = 2$ TeV. It can clearly be seen that near η of zero, $\beta\gamma \approx 1$, while at larger values of $|\eta|$, $\beta\gamma$ can easily reach values of 6. This is important because the observed decay length varies with $\beta\gamma$ and furthermore the absolute momenta of the decay products are larger allowing for a suppression of the multiple scattering error.

Since the detector design is somewhat dependent on the Monte Carlo generated b production distributions, it is important to check that the correlations between the b and the $\bar{b}$ are adequately reproduced. Fig. 3 shows the azimuthal opening angle distribution between a muon from a b quark decay and the $\bar{b}$ jet as measured by CDF [3] and compares it with the MNR predictions [4].

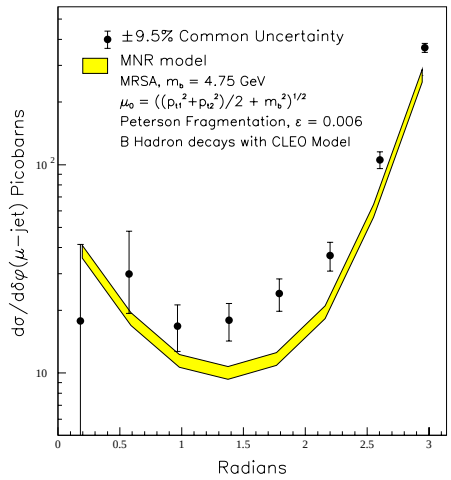

Figure 3: The differential $\delta\phi$ cross-sections for $p_T^{\mu} > 9$ GeV/c, $|\eta^{\mu}| < 0.6$, $E_T^{\bar{b}} > 10$ GeV, $\left|\eta^{\bar{b}}\right| < 1.5$ compared with theoretical predictions. The data points have a common systematic uncertainty of ±9.5%. The uncertainty in the theory curve arises from the error on the muonic branching ratio and the uncertainty in the fragmentation model.

The model does a good job representing the shape which shows a strong back-to-back correlation. The normalization is about a factor of two higher in the data than the theory, which is generally true of CDF b cross-section measurements [5]. In hadron colliders all B species, B^o, B^+, B_s^o, b-baryons, and even B_c mesons, are produced at the same time.

The "flat" η distribution hides an important correlation of $b\bar{b}$ production at hadronic colliders. In Fig. 4 the production angle of the hadron containing the b quark is plotted versus the production angle of the hadron containing the $\bar{b}$ quark. There is a very strong correlation in the forward (and backward) direction: when the B is forward the $\overline{B}$ is also forward. This correlation is not present in the central region (near zero degrees). By instrumenting a relatively small region of angular phase space, a large number of $b\bar{b}$ pairs can be detected. Furthermore the B's populating the forward and backward regions have large

values of $\beta\gamma$ and this permits more accurate separation of the primary and secondary vertices and better overall detection efficiency for b hadrons. In addition, the techniques for particle identification in this kinematic range are very well-developed. Powerful particle identification is a key to high sensitivity bottom and charm experiments. For these reasons, we have designed a detector with 'forward coverage'. This detector is described in detail in Section 2.

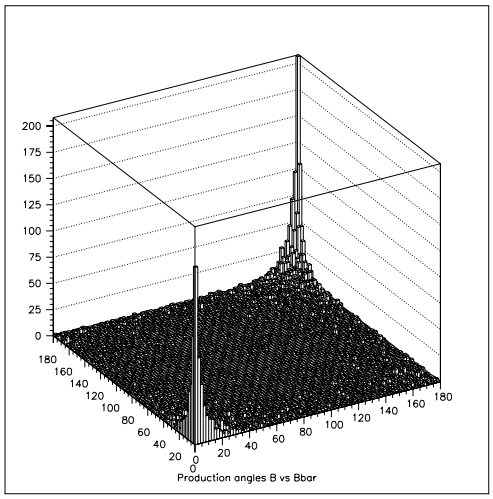

Figure 4: The production angle (in degrees) for the hadron containing a b quark plotted versus the production angle for a hadron containing $\bar{b}$ quark, from the Phythia Monte Carlo generator.

Charm production is similar to b production but has a much larger cross section. Current theoretical estimates are that charm is 1-2% of the total $p\bar{p}$ cross-section. The cross section is even more strongly peaked in the forward and backward direction because the average transverse momentum is of the order of only 1.5 GeV/c. The charm cross section has never been measured because the experiments whose acceptance is in the central region have very low efficiency for triggering and reconstructing charm. The favorable kinematics in the forward direction gives BTeV a very high efficiency for reconstructing charm.

Table 1 gives the relevant Tevatron parameters. We expect to start serious data taking in Fermilab Run II with a luminosity of about $5 \times 10^{31}\mathrm{cm}^{-2}\mathrm{s}^{-1}$; our ultimate luminosity goal, to be obtained in Run III, is $2 \times 10^{32}\mathrm{cm}^{-2}\mathrm{s}^{-1}$.

1.2.1 Fixed Target or Wire-Mode Running

While BTeV is designed to study $p\bar{p}$ collisions at 2 TeV, it can also run in 'Fixed Target' mode. In that mode, a thin wire is inserted into the halo of the circulating beam and the detector studies the collisions of 800 GeV/c protons (or anti-protons) with the nuclei of the wire. For this reason, Fixed Target mode

Table 1: The Tevatron as a b and c source for C0 in Run II.

Luminosity in Run II	$5 \times 10^{31}\text{cm}^{-2}\text{s}^{-1}$
Luminosity (ultimate)	$2 \times 10^{32}\text{cm}^{-2}\text{s}^{-1}$
b cross-section	100μb
# of b's per 10^7 sec (Run II)	10^{11}
b fraction	0.2%
c cross-section	> 500 μb
Bunch spacing	132 ns
Luminous region length	$\sigma_z = 30$ cm
Luminous region length	σ_x $\sigma_y = \approx 50$ μm
Interactions/crossing	$< 0.5 >$

is also referred to as 'wire mode'.

In this mode, particles diffusing laterally out of the beam eventually reach the wire target where they can interact. Since the diffusion is very slow, each particle will traverse the wire many times until it either interacts or multiple scattering blows its orbit up so badly that it escapes from the machine aperture altogether. We are learning from accelerator physicists what overall interaction rate we can expect.

The cross section for fixed target charm production on a proton at 800 GeV/c is about 30 μb. While this is much lower than in the collider, there are some advantages: first, it may not require low-β quadrupoles to be installed so it might be available to us earlier than collider mode; second, it is not expected to affect the luminosity at B0 or D0, which is not the case when the beams collide at C0 and this will translate into longer running times; the region along the beam that has to be instrumented with precision vertex detectors is much smaller which means that a small scale vertex detector prototype is all that is needed for initial experiments; and the fact that the center of mass is boosted towards the spectrometer increases the acceptance. However, this mode is not useful to us for B-physics studies because the cross section is of order 10 nb. While we believe that the most sensitive charm experiment will be using the collider, this mode does give us the opportunity to do physics early with a partially instrumented detector.

1.3 Bottom Physics – Important Questions and Status of the Field in the year 2000 and Later

The physical point-like states of nature that have both strong and electroweak interactions, the quarks, are mixtures of base states described by the Cabibbo-Kobayashi-Maskawa matrix [6];

$$\begin{pmatrix} d' \\ s' \\ b' \end{pmatrix} = \begin{pmatrix} V_{ud} & V_{us} & V_{ub} \\ V_{cd} & V_{cs} & V_{cb} \\ V_{td} & V_{ts} & V_{tb} \end{pmatrix} \begin{pmatrix} d \\ s \\ b \end{pmatrix} \tag{2}$$

The unprimed states are the mass eigenstates, while the primed states denote the weak eigenstates.

There are nine complex CKM elements. These 18 numbers can be reduced to four independent quantities by applying unitarity constraints and the fact that the phases of the quark wave functions are arbitrary. These four remaining numbers are fundamental constants of nature that need to be determined from experiment, like any other fundamental constant such as α or G. In the Wolfenstein approximation the matrix is written as [7]

$$V_{CKM} = \begin{pmatrix} 1-\lambda^2/2 & \lambda & A\lambda^3(\rho - i\eta) \\ -\lambda & 1-\lambda^2/2 & A\lambda^2 \\ A\lambda^3(1-\rho-i\eta) & -A\lambda^2 & 1 \end{pmatrix}. \tag{3}$$

The constants λ and A have been measured using semileptonic s and b decays [8].

The phase η allows for CP violation. CP violation thus far has only been seen in the neutral kaon system. If we can find CP violation in the B system we could see if the CKM model works or perhaps discover new physics that goes beyond the model, if it does not.

1.3.1 Tests of the Standard Model via the CKM triangle

The unitarity of the CKM matrix[1] allows us to construct six relationships. The one most relevant to B-decays is:

$$V_{ud}V_{td}^* + V_{us}V_{ts}^* + V_{ub}V_{tb}^* = 0 \quad . \tag{4}$$

To a good approximation

$$V_{ud} \approx V_{tb}^* \approx 1 \quad \text{and} \quad V_{ts}^* \approx -V_{cb}, \tag{5}$$

then

$$\frac{V_{ub}}{V_{cb}} + \frac{V_{td}^*}{V_{cb}} - V_{us} = 0 \quad . \tag{6}$$

[1] Unitarity implies that any pair of rows or columns are orthogonal.

Since $V_{us} = \lambda$, we can define a triangle with sides

$$1 \tag{7}$$

$$\left|\frac{V_{td}}{A\lambda^3}\right| = \sqrt{(\rho-1)^2+\eta^2} = \frac{1}{\lambda}\left|\frac{V_{td}}{V_{ts}}\right| \tag{8}$$

$$\left|\frac{V_{ub}}{A\lambda^3}\right| = \sqrt{\rho^2+\eta^2} = \frac{1}{\lambda}\left|\frac{V_{ub}}{V_{cb}}\right|. \tag{9}$$

The CKM triangle is depicted in Fig. 5. We know two sides already: the

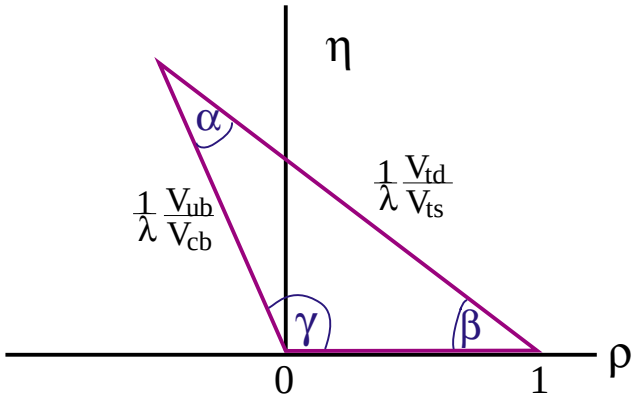

Figure 5: The CKM triangle shown in the $\rho-\eta$ plane. The left side is determined by $|V_{ub}/V_{cb}|$ and the right side can be determined using mixing in the neutral B system. The angles can be found by making measurements of CP violation in B decays.

base is defined as unity and the left side is determined by the measurements of $|V_{ub}/V_{cb}|$. The right side can be determined using mixing measurements in the neutral B system. We will see, however, that there is a large error due to the uncertainty in f_B, the B-meson decay constant. Later we will discuss other measurements that can determine this side. The figure also shows the angles α, β, and γ. These angles can be determined by measuring CP violation in the B system.

To test the Standard Model we can measure all three sides and all three angles. If we see consistency between all of these measurements we have defined the parameters of the Standard Model. If we see inconsistency, the breakdown can point us to physics beyond the Standard Model.

1.3.2 CP Violation

The fact that the CKM matrix is complex allows CP violation. This is not only true for three generations of quark doublets, but for any number greater than

two. CP violation thus far has only been seen in the neutral kaon system.

There is a constraint on ρ and η given by the K_L^o CP violation measurement (ϵ), given by [10]

$$\eta\left[(1-\rho)A^2(1.4\pm 0.2)+0.35\right]A^2\frac{B_K}{0.75}=(0.30\pm 0.06), \tag{10}$$

where the errors arise from uncertainties on m_t and m_c. The constraints on ρ versus η from the V_{ub}/V_{cb} measurement, ϵ and B mixing are shown in Fig. 6. The width of the B mixing band iscaused mainly by the uncertainty on f_B, taken here as $240 > f_B > 160$ MeV. The width of the ϵ band is caused by errors in A, m_t, m_c and B_K. The size of these error sources is shown in Fig. 7. The largest error still comes from the measurement of V_{cb}, with the theoretical estimate of B_K being a close second. The errors on m_t and m_c are less important.

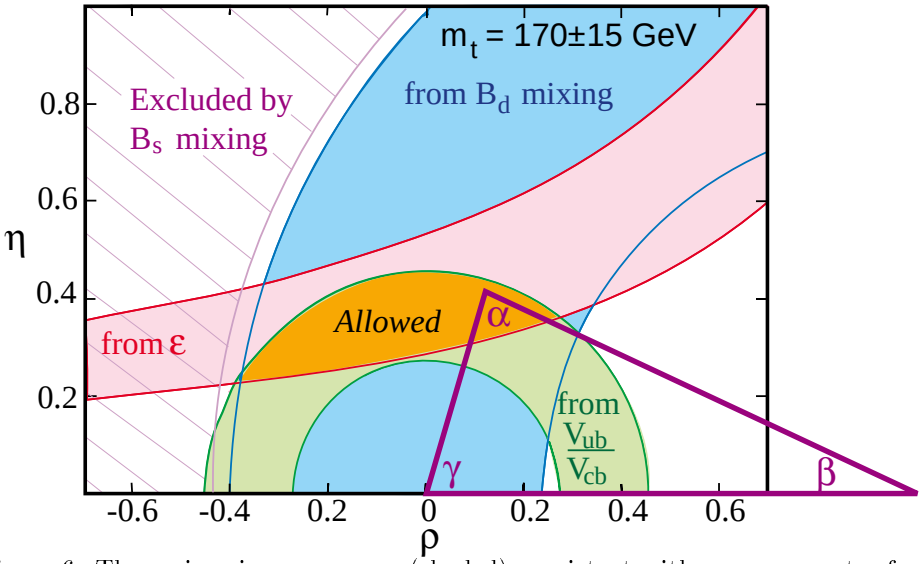

Figure 6: The regions in $\rho-\eta$ space (shaded) consistent with measurements of CP violation in K_L^o decay (ϵ), V_{ub}/V_{cb} in semileptonic B decay, B_d^o mixing, and the excluded region from limits on B_s^o mixing. The allowed region is defined by the overlap of the 3 permitted areas, and is where the apex of the CKM triangle sits.

1.3.3 Ways of Measuring CP violation in B Decays

CP Violation in Charged B Decays

The theoretical basis of the study of CP violation in B decays was given in a series of papers by Carter and Sanda and Bigi and Sanda [11]. We start with charged B decays. Consider the final states $f^{\pm}$ which can be reached by two distinct weak processes with amplitudes $\mathcal{A}$ and $\mathcal{B}$, respectively.

$$\mathcal{A}=a_s e^{i\theta_s}a_w e^{i\theta_w},\quad \mathcal{B}=b_s e^{i\delta_s}b_w e^{i\delta_w}\quad . \tag{11}$$

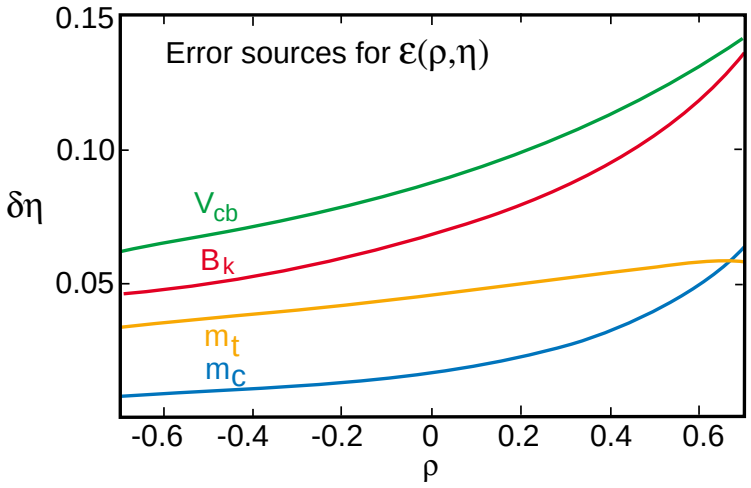

Figure 7: Error sources in units of $\delta\eta$ on the value of η as a function of ρ provided by the CP violation constraint in K_L^o decay.

The strong phases are denoted by the subscript s and weak phases are denoted by the subscript w. Under the CP operation the strong phases remain constant but the weak phases change sign, so

$$\overline{\mathcal{A}} = a_s e^{i\theta_s} a_w e^{-i\theta_w}, \quad \overline{\mathcal{B}} = b_s e^{i\delta_s} b_w e^{-i\delta_w} \quad . \tag{12}$$

The rate difference is

$$\begin{aligned} \Gamma - \overline{\Gamma} &= |\mathcal{A} + \mathcal{B}|^2 - |\overline{\mathcal{A}} + \overline{\mathcal{B}}|^2 & (13) \\ &= 2a_s a_w b_s b_w \sin(\delta_s - \theta_s) \sin(\delta_w - \theta_w) \quad . & (14) \end{aligned}$$

A weak phase difference is guaranteed in the appropriate decay mode (different CKM phases), but the strong phase difference is not; it is very difficult to predict the magnitude of strong phase differences.

As an example consider the possibility of observing CP violation by measuring a rate difference between $B^- \to K^-\pi^o$ and $B^+ \to K^+\pi^o$. The $K^-\pi^o$ final state can be reached either by tree or penguin diagrams as shown in Fig. 8. The tree diagram has an imaginary part coming from the V_{ub} coupling, while the penguin term does not, thus insuring a weak phase difference. This type of CP violation is called "direct." Note also that the process $B^- \to K^o\pi^-$ can only be produced by the penguin diagram in Fig. 8(d). Therefore, we do not expect a rate difference between $B^- \to K^o\pi^-$ and $B^+ \to K^o\pi^+$.

Formalism in neutral B decays

For neutral mesons we can construct the CP eigenstates

$$\left|B_1^o\right\rangle = \frac{1}{\sqrt{2}}\left(\left|B^o\right\rangle + \left|\overline{B}^o\right\rangle\right) \quad , \tag{15}$$

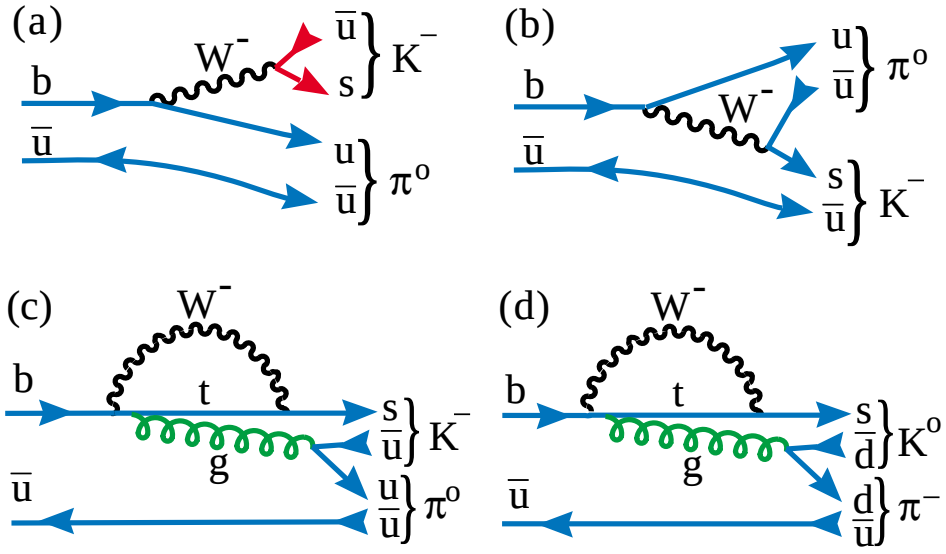

Figure 8: Diagrams for $B^- \to K^- \pi^o$, (a) and (b) are tree level diagrams where (b) is color suppressed; (c) is a penguin diagram. (d) shows $B^- \to K^o \pi^-$, which cannot be produced via a tree diagram.

$$\left|B_2^o\right\rangle \;=\; \frac{1}{\sqrt{2}}\left(\left|B^o\right\rangle - \left|\overline{B}^o\right\rangle\right) \quad , \tag{16}$$

where

$$CP\left|B_1^o\right\rangle \;=\; \left|B_1^o\right\rangle \quad , \tag{17}$$

$$CP\left|B_2^o\right\rangle \;=\; -\left|B_2^o\right\rangle \quad . \tag{18}$$

Since B^o and $\overline{B}^o$ can mix, the mass eigenstates are superpositions of $a\left|B^o\right\rangle + b\left|\overline{B}^o\right\rangle$ which obey the Schrodinger equation

$$i\frac{d}{dt}\begin{pmatrix} a \\ b \end{pmatrix} = H\begin{pmatrix} a \\ b \end{pmatrix} = \left(M - \frac{i}{2}\Gamma\right)\begin{pmatrix} a \\ b \end{pmatrix}. \tag{19}$$

If CP is not conserved then the eigenvectors, the mass eigenstates $\left|B_L\right\rangle$ and $\left|B_H\right\rangle$, are not the CP eigenstates but are

$$\left|B_L\right\rangle = p\left|B^o\right\rangle + q\left|\overline{B}^o\right\rangle, \quad \left|B_H\right\rangle = p\left|B^o\right\rangle - q\left|\overline{B}^o\right\rangle, \tag{20}$$

where

$$p = \frac{1}{\sqrt{2}}\frac{1+\epsilon_B}{\sqrt{1+|\epsilon_B|^2}}, \quad q = \frac{1}{\sqrt{2}}\frac{1-\epsilon_B}{\sqrt{1+|\epsilon_B|^2}}. \tag{21}$$

CP is violated if $\epsilon_B \neq 0$, which occurs if $|q/p| \neq 1$.

The time dependence of the mass eigenstates is

$$\left|B_L(t)\right\rangle = e^{-\Gamma_L t/2} e^{im_L t/2} \left|B_L(0)\right\rangle \quad (22)$$

$$\left|B_H(t)\right\rangle = e^{-\Gamma_H t/2} e^{im_H t/2} \left|B_H(0)\right\rangle, \quad (23)$$

leading to the time evolution of the flavor eigenstates as

$$\left|B^o(t)\right\rangle = e^{-\left(im+\frac{\Gamma}{2}\right)t} \left(\cos\frac{\Delta m t}{2}\left|B^o(0)\right\rangle + i\frac{q}{p}\sin\frac{\Delta m t}{2}\left|\overline{B}^o(0)\right\rangle\right) \quad (24)$$

$$\left|\overline{B}^o(t)\right\rangle = e^{-\left(im+\frac{\Gamma}{2}\right)t} \left(i\frac{p}{q}\sin\frac{\Delta m t}{2}\left|B^o(0)\right\rangle + \cos\frac{\Delta m t}{2}\left|\overline{B}^o(0)\right\rangle\right), \quad (25)$$

where $m = (m_L + m_H)/2$, $\Delta m = m_H - m_L$ and $\Gamma = \Gamma_L \approx \Gamma_H$. Note, that the probability of a B^o decay as a function of t is given by $\left\langle B^o(t)\middle|B^o(t)\right\rangle^*$, and is a pure exponential, $e^{-\Gamma t/2}$, in the absence of CP violation.

Indirect CP violation in the neutral B system

As in the case of K_L decay, we can look for the rate asymmetry

$$a_{sl} = \frac{\Gamma\left(\overline{B}^o(t) \to X\ell^+\nu\right) - \Gamma\left(B^o(t) \to X\ell^-\overline{\nu}\right)}{\Gamma\left(\overline{B}^o(t) \to X\ell^+\nu\right) + \Gamma\left(B^o(t) \to X\ell^-\bar{\nu}\right)} \quad (26)$$

$$= \frac{1 - \left|\frac{q}{p}\right|^4}{1 + \left|\frac{q}{p}\right|^4} \approx O\left(10^{-2}\right). \quad (27)$$

These final states occur only through mixing as the direct decay occurs only as $B^o \to X\ell^+\nu$. To generate CP violation we need an interference between two diagrams. In this case the two diagrams are the mixing diagram with the t-quark and the mixing diagram with the c-quark. This is identical to what happens in the K_L^o case. This type of CP violation is called "indirect." The small size of the expected asymmetry is caused by the off-diagonal elements of the Γ matrix in equation (19) being very small compared to the off-diagonal elements of the mass matrix, i.e. $|\Gamma_{12}/M_{12}| << 1$. This results from the nearly equal widths of the B_L^o and B_H^o [12].

CP violation for B via interference of mixing and decays

Here we choose a final state f which is accessible to both B^o and $\overline{B}^o$ decays. The second amplitude necessary for interference is provided by mixing. Fig. 9 shows the decay into f either directly or indirectly via mixing. It is necessary only that f be accessible directly from either state. However if f is a CP eigenstate the situation is far simpler. For CP eigenstates

$$CP\left|f_{CP}\right\rangle = \pm\left|f_{CP}\right\rangle. \quad (28)$$

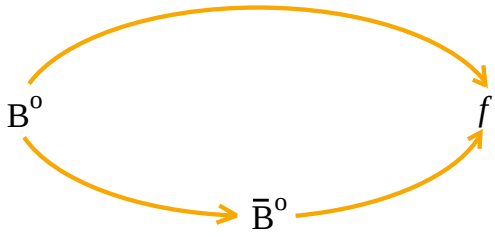

Figure 9: Two interfering ways for a B^o to decay into a final state f.

It is useful to define the amplitudes

$$A = \langle f_{CP}|\mathcal{H}|B^o\rangle, \quad \bar{A} = \langle f_{CP}|\mathcal{H}|\overline{B}^o\rangle. \tag{29}$$

If $\left|\frac{\bar{A}}{A}\right| \neq 1$, then we have "direct" CP violation in the decay amplitude, which was discussed above. Here CP can be violated by having

$$\lambda = \frac{q}{p} \cdot \frac{\bar{A}}{A} \neq 1, \tag{30}$$

which requires only that λ acquire a non-zero phase, i.e. $|\lambda|$ could be unity and CP violation can occur.

The asymmetry, in this case, is defined as

$$a_{f_{CP}} = \frac{\Gamma\left(B^o(t) \to f_{CP}\right) - \Gamma\left(\overline{B}^o(t) \to f_{CP}\right)}{\Gamma\left(B^o(t) \to f_{CP}\right) + \Gamma\left(\overline{B}^o(t) \to f_{CP}\right)}, \tag{31}$$

which for $|q/p| = 1$ gives

$$a_{f_{CP}} = \frac{\left(1 - |\lambda|^2\right)\cos\left(\Delta m t\right) - 2\mathrm{Im}\lambda \sin(\Delta m t)}{1 + |\lambda|^2}. \tag{32}$$

For the cases where there is only one decay amplitude A, $|\lambda|$ equals 1, and we have

$$a_{f_{CP}} = -\mathrm{Im}\lambda \sin(\Delta m t). \tag{33}$$

Only the amplitude, $-\mathrm{Im}\lambda$ contains information about the level of CP violation, the sine term is determined only by B_d mixing. In fact, the time integrated asymmetry is given by

$$a_{f_{CP}} = -\frac{x}{1+x^2}\mathrm{Im}\lambda = -0.48\mathrm{Im}\lambda \quad , \tag{34}$$

where $x = \frac{\Delta m}{\Gamma}$. This is quite lucky as the maximum size of the coefficient is -0.5.

Imλ is related to the CKM parameters. Recall $\lambda = \frac{q}{p} \cdot \frac{\bar{A}}{A}$. The first term is the part that comes from mixing:

$$\frac{q}{p} = \frac{(V_{tb}^* V_{td})^2}{|V_{tb} V_{td}|^2} = \frac{(1-\rho-i\eta)^2}{(1-\rho+i\eta)\,(1-\rho-i\eta)} = e^{-2i\beta} \quad \text{and} \tag{35}$$

$$\mathrm{Im}\frac{q}{p} = -\frac{2(1-\rho)\eta}{(1-\rho)^2+\eta^2} = \sin(2\beta). \tag{36}$$

To evaluate the decay part we need to consider specific final states. For example, consider $f \equiv \pi^+\pi^-$. The simple spectator decay diagram is shown in Fig. 10. For the moment we will assume that this is the only diagram which

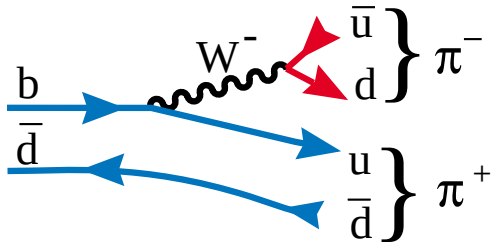

Figure 10: Decay diagram at the tree level for $B^o \to \pi^+\pi^-$.

contributes. Later we will show why this is not true. For this $b \to u\bar{u}d$ process we have

$$\frac{\bar{A}}{A} = \frac{(V_{ud}^* V_{ub})^2}{|V_{ud} V_{ub}|^2} = \frac{(\rho-i\eta)^2}{(\rho-i\eta)(\rho+i\eta)} = e^{-2i\gamma}, \tag{37}$$

and

$$\mathrm{Im}(\lambda) = \mathrm{Im}(e^{-2i\beta} e^{-2i\gamma}) = \mathrm{Im}(e^{2i\alpha}) = \sin(2\alpha), \tag{38}$$

where the last equality is true only if there really is a unitarity triangle.

The final state ψK_s plays an especially important role in the study of CP violation. It is a CP eigenstate and its decay is dominated by only one diagram, shown in Fig. 11. In this case we do not get a phase from the decay part because

$$\frac{\bar{A}}{A} = \frac{(V_{cb} V_{cs}^*)^2}{|V_{cb} V_{cs}|^2} \tag{39}$$

is real. In this case the final state is a state of negative CP, i.e. $CP\left|\psi K_s\right\rangle = -\left|\psi K_s\right\rangle$. This introduces an additional minus sign in the result for Imλ. Before finishing discussion of this final state we need to consider in more detail the presence of the K_S in the final state. Since neutral kaons can mix, we pick up another mixing phase. This term creates a phase given by

$$\left(\frac{q}{p}\right)_K = \frac{(V_{cd}^* V_{cs})^2}{|V_{cd} V_{cs}|^2}, \tag{40}$$

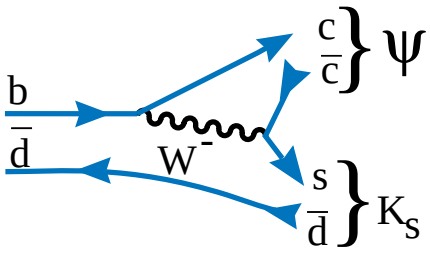

Figure 11: Decay diagram at the tree level for $B^o \to \psi K_S$.

which is real. It necessary to include this term, however, since there are other formulations of the CKM matrix than Wolfenstein, which have the phase in a different location. It is important that the physics predictions not depend on the CKM convention.[2]

In summary, for the case of $f = \psi K_s$, $\mathrm{Im}\lambda = -\sin(2\beta)$.

Comment on Penguin Amplitude

In principle all processes can have penguin components. One such diagram is shown in Fig. 12. The $\pi^+\pi^-$ final state is expected to have a rather large penguin amplitude ~10% of the tree amplitude. Then $|\lambda| \neq 1$ and $a_{\pi\pi}(t)$ develops a $\cos(\Delta mt)$ term. It turns out (see Gronau [13]), that $\sin(2\alpha)$ can be extracted using isospin considerations and measurements of the branching ratios for $B^+ \to \pi^+\pi^o$ and $B^o \to \pi^o\pi^o$. This method, though difficult to apply, has no model dependence. Deshpande and He [14] have shown that a good estimate of the Penguin contribution to $\pi^+\pi^-$ can be made by measuring the difference in rates between $\overline{B^o} \to K^-\pi^+$ versus $B^o \to K^+\pi^-$. This assumes only SU(3) symmetry.

In the ψK_S case, the penguin amplitude is expected to be small since a $c\bar{c}$ pair must be "popped" from the vacuum. Even if the penguin decay amplitude were of significant size, the decay phase is the same as the tree level process, namely zero.

Direct measurement of $\sin\gamma$

The angle γ can also be determined using measured rates in charged B decays to D^0K final states. The method proposed by Gronau and Wyler [15] uses the three related decay modes $B^- \to D^0K^-$, $B^- \to \bar{D}^0K^-$, $B^- \to D_{CP}K^-$, where D_{CP} indicates that the D^0 decays into a CP eigenstate, and the corresponding modes for B^+. The decay $B^- \to D^0K^-$ is a Cabibbo suppressed version of $B^- \to D^0\pi^-$, while the decay $B^- \to \bar{D}^0K^-$ is a color suppressed $b \to u$ transition where the virtual W^- transforms itself into a $\bar{c}s$ pair. Interference is

[2]Here we don't include CP violation in the neutral kaon since it is much smaller than what is expected in the B decay.

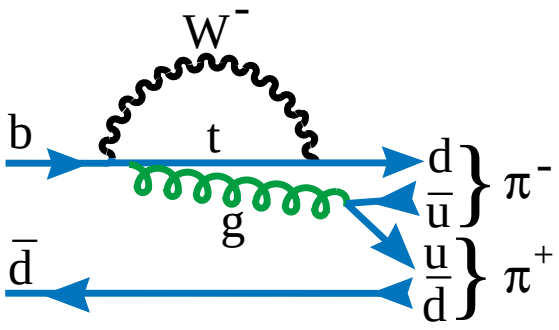

Figure 12: Penguin diagram for $B^o \to \pi^+\pi^-$.

possible between these two decays modes if the D^0 decays into a CP eigenstate. Examples of such final states include K^+K^-, $K_s\pi^0$, and $K_s\eta$. To simplify the discussion only states that are in specific angular momentum configurations are used so that their CP is defined as $+1$ or -1; these states are usually denoted as D_1^0 and D_2^0. We have

$$D_1^0 = \frac{1}{\sqrt{2}}\left[D^0 + \bar{D}^0\right], \quad \text{and} \quad D_2^0 = \frac{1}{\sqrt{2}}\left[D^0 - \bar{D}^0\right].$$

The amplitudes for the three B^- decay modes are related by:

$$\sqrt{2}\mathrm{A}_1^-(B^- \to D_1^0 K^-) = \mathrm{A}(B^- \to \bar{D}^0 K^-) + \overline{\mathrm{A}}(B^- \to D^0 K^-).$$

Denoting the hadronic phase as δ, gives

$$\sqrt{2}\mathrm{A}_1^-(B^- \to D_1^0 K^-) = |\mathrm{A}|e^{i(\phi_s+\delta)} + \overline{\mathrm{A}}e^{i\overline{\delta}}.$$

The decays to D_1^0 need not be equal for B^+ and B^-, and an asymmetry in them is a manifest demonstration of CP violation. A triangle construction serves to determine $\sin\gamma$. For more details see [15, 16].

Recently, Atwood, Dunietz and Soni [28] pointed out that although most authors had considered using the $\bar{D}^o \to K^+\pi^-$ decay to determine the D^o flavor, that the doubly-Cabibbo supressed decay $D^o \to K^+\pi^-$ is actually far larger than the V_{ub} dominated B^- decay and would overwhelm it. They further show that this "problem" is actually a blessing in disguise since it provides a large alternative amplitude and allows one to measure CP violation, though extracting γ requires one to measure something in addition, such as the D^o strong decay phases. There are several other techniques that can be used to measure γ [17].

What actually has to be measured?

We need to measure the angles of the CKM triangle. The expected range of angles derived from Fig. 6 is shown in Fig. 13.

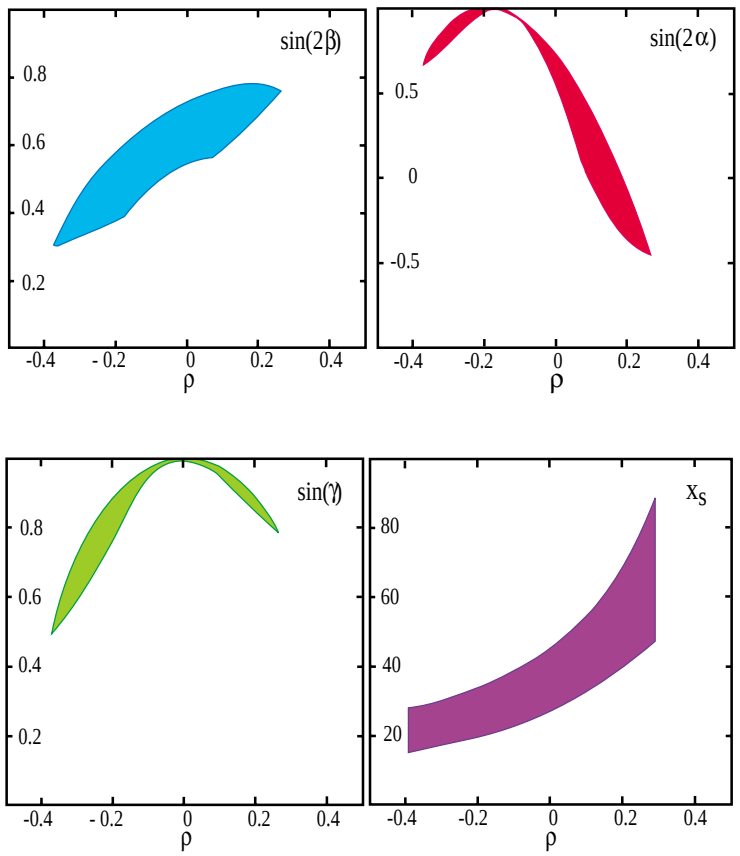

Figure 13: The "allowed" values for the three angles of the CKM triangle and x_s, the B_s mixing parameter, derived from the allowed region of Fig. 6.

These plots show only the most likely values in the Standard Model. Recall that they are based on the overlap of $\pm 1\sigma$ bands from constraints on V_{ub}/V_{cb}, ϵ, and B_d mixing. However, this gives us a good indication on where we should target our measuring potential.

In charged B decays we only have to measure a branching ratio difference between B^+ and B^- to see CP violation. For neutral B decays we must find the flavor of the other b-quark produced in the event (this is called tagging), since we do not have any B^o beams. We then measure a rate asymmetry

$$a_{asy} = \frac{\#(f, \ell^+) - \#(f, \ell^-)}{\#(f, \ell^+) + \#(f, \ell^-)}, \tag{41}$$

where $\ell^\pm$ indicates the charge of the lepton from the "other" b and thus provides a flavor tag. In Fig. 14(a) the time dependence for the B^o and $\bar{B}^o$ are shown as a function of t in the B rest frame for 500 simulated experiments of an average

of 2000 events each with an input asymmetry of 0.3. In Fig. 14(b) the fitted asymmetry is shown for 500 different "experiments."

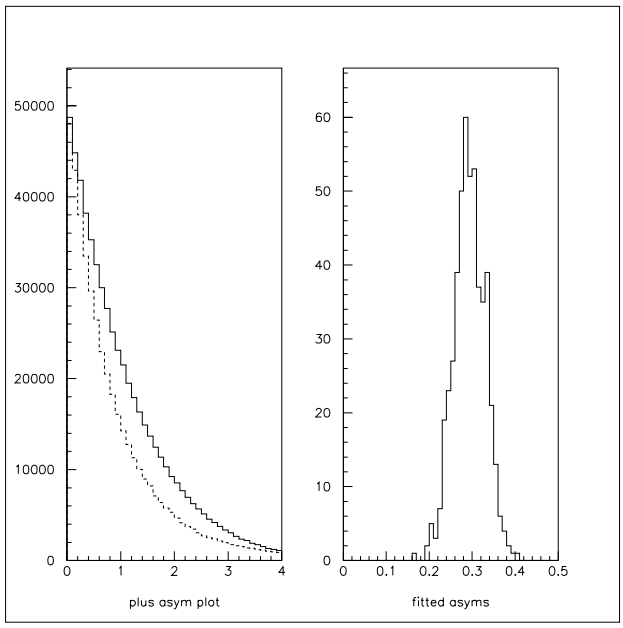

Figure 14: (a) Time dependence of B^o and $\overline{B}^o$ decaying into a CP eigenstate, for an asymmetry of 0.3 for a total of 1 million events. The x-axis is proper time. In (b) the fitted asymmetry results are shown for 500 "experiments" of average of 2000 events each.

1.3.4 Better Measurements of the sides of the CKM triangle

One side of the triangle is determined by $|V_{ub}/V_{cb}|$. It appears that the best way to improve the values now is to measure the form-factors in the reactions $B \to \pi\ell\nu$ and $B \to \rho\ell\nu$. Input from the charm reactions $D \to \pi\ell\nu$ and $D \to \rho\ell\nu$ will also be helpful. This will decrease the model dependence error, still the dominant error, in the V_{ub} determination. Lattice gauge model calculations are appearing and should be quite useful.

The other side of the triangle can determined by measuring B_s mixing, using the ratio

$$\frac{x_s}{x_d} = \left(\frac{B_s}{B}\right)\left(\frac{f_{B_s}}{f_B}\right)^2\left(\frac{\tau_{B_s}}{\tau_B}\right)\left|\frac{V_{td}}{V_{ts}}\right|^2, \qquad (42)$$

where

$$\left|\frac{V_{td}}{V_{ts}}\right|^2 = \lambda^2\left[(\rho-1)^2+\eta^2\right]. \tag{43}$$

The large uncertainty in using the B_d mixing measurement to constrain ρ and η is largely removed as the ratio of the first three factors in equation (42) is already known to 10%.

As an alternative to measuring x_s, we can measure the ratio of the penguin decay rates

$$\frac{\mathcal{B}(B\to\rho\gamma)}{\mathcal{B}(B\to K^*\gamma)} = \xi\left|\frac{V_{td}}{V_{ts}}\right|^2, \tag{44}$$

where ξ is a model dependent correction due to different form-factors. Soni [18] has claimed that "long distance" effects, basically other diagrams, spoil this simple relationship. This is unlikely for $\rho^o\gamma$ but possible for $\rho^+\gamma$.[3] If this occurs, however, then it is possible to find CP violation by looking for a difference in rate between $\rho^+\gamma$ and $\rho^-\gamma$.

The CLEO II data are already background limited. The limit quoted is [19]

$$\frac{\mathcal{B}(B\to\rho\gamma)}{\mathcal{B}(B\to K^*\gamma)} < 0.19 \tag{45}$$

at 90% confidence level.

1.3.5 Rare decays as Probes beyond the Standard Model

Rare decays have loops in the decay diagrams so they are sensitive to high mass gauge bosons and fermions. However, it must be kept in mind that any new effect must be consistent with already measured phenomena such as B_d^o mixing and $b\to s\gamma$.

Let us now consider searches for other rare b decay processes. We start with $b\to s\ell^+\ell^-$. When searching for such decays, care must be taken to eliminate the mass region in the vicinity of the ψ or ψ' resonances, lest these more prolific processes, which are not rare decays, contaminate the sample. The results of searches are shown in Table 2.

B's can also decay into dilepton final states. The Standard Model diagrams are shown in Fig. 15. In (a) the decay rate is proportional to $|V_{ub}f_B|^2$. The diagram in (b) is much larger for B_s than B_d, again the factor of $|V_{ts}/V_{td}|^2$. Results of searches are given in Table 3.

[3] One example is the B^- decay which proceeds via $b\to uW^-$, where the $W^-\to\bar{u}d\to\rho^-$ and the u combines with the spectator $\bar{u}$ to form a photon.

Table 2: Searches for $b \to s\ell^+\ell^-$ decays

b decay mode	90% c.l. upper limit	Group	Ali et al. Prediction[20]
$s\mu^+\mu^-$	50×10^{-6}	UA1[21]	
$K^{*o}\mu^+\mu^-$	25×10^{-6}	CDF[23]	2.9×10^{-6}
	23×10^{-6}	UA1[21]	
	31×10^{-6}	CLEO[22]	
$K^{*o}e^+e^-$	16×10^{-6}	CLEO[22]	5.6×10^{-6}
$K^-\mu^+\mu^-$	9×10^{-6}	CLEO[22]	0.6×10^{-6}
	10×10^{-6}	CDF[23]	
$K^-e^+e^-$	12×10^{-6}	CLEO[22]	0.6×10^{-6}

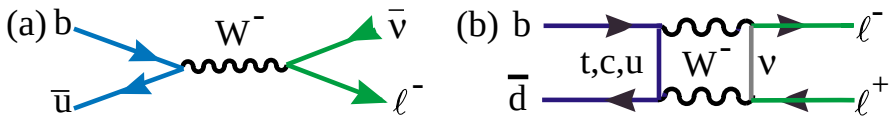

Figure 15: Decay diagrams resulting in dilepton final states. (a) is an annihilation diagram, and (b) is a box diagram.

Table 3: Upper limits on $b \to$ dilepton decays (@90% c.l.)

	$\mathcal{B}(B^o \to \ell^+\ell^-)$		$\mathcal{B}(B_s \to \ell^+\ell^-)$	$\mathcal{B}(B^- \to \ell^-\bar{\nu})$		
	e^+e^-	$\mu^+\mu^-$	$\mu^+\mu^-$	$e^-\bar{\nu}$	$\mu^-\bar{\nu}$	$\tau^-\bar{\nu}$
SM†	2×10^{-15}	8×10^{-11}	2×10^{-9}	10^{-15}	10^{-8}	10^{-5}
UA1[21]		8.3×10^{-6}				
CLEO[24]	5.9×10^{-6}	5.9×10^{-6}		1.5×10^{-5}	2.1×10^{-5}	2.2×10^{-3}
CDF[23]		1.6×10^{-6}	8.4×10^{-6}			
ALEPH[25]						1.8×10^{-3}

†SM is the Standard Model prediction.[26]

1.4 Charm Physics in BTeV

While the Standard Model predicts large effects in mixing and CP violation for b-decays, it predicts very small effects in charm. Thus, the charm sector presents an opportunity to observe non-standard model effects without the complications of large standard model 'backgrounds'.

Charm sensitivities have increased dramatically over the last two decades. Current experiments (FOCUS, SELEX, and CLEO-II) aim to reconstruct $\sim 10^6$ events, and the B factories and COMPASS facility [31], could achieve 10^7-event sensitivity. In the BTeV/C0 program, the expected charm sensitivity is 10^8 to 10^9 decays per year reconstructed with signal/background comparable to or better than that of existing experiments. Sensitivity at this level will give substantial new-physics reach in the areas of CP violation, flavor-changing neutral-current and lepton-number-violating decays, and $D^0\overline{D^0}$ mixing. In the case of CP violation, this reach extends all the way from existing limits (see below) to the Standard Model prediction for CP violation. If no new physics appears, direct CP violation in Cabibbo-suppressed D decays at the level predicted by the Standard Model could be observable in the BTeV experiment.

1.4.1 Importance of Charm CP-Violation, Mixing, and Rare-Decay Studies

As discussed above, CP violation is recognized as one of the central problems of particle physics. The mechanism(s) responsible for it have yet to be definitively established. The Cabibbo-Kobayashi-Maskawa (CKM) model, described above, has the attractive feature of explaining the small size of K^0 CP asymmetries while predicting large CP asymmetries in the beauty sector. It predicts very small asymmetries in charm decays. Other models attribute CP violation to the exchange of massive particles such as W's with right-handed coupings or extra Higgs scalars [32]. In these models CP asymmetries should be more "democratic". Many of these models predict large mixing and/or CP violation in charm.

We do not know whether CP violation arises exclusively from any one of these mechanisms, whether many contribute, or whether some other mechanism not yet thought of is the answer. Studies in charm are important precisely because the small Standard Model predictions can allow new physics to appear in a striking manner. By carrying out sensitive studies in both the charm and beauty sectors, BTeV can make important contributions towards the establishment of the (Standard Model) CKM mechanism or of new-physics mechanisms.

Similarly, the Standard Model predicts very small $D^o\bar{D}^o$ mixing because the box diagram describing mixing depends on V_{cb} and V_{ub} whose product is of order λ^5 and is therefore small. Further, the magnitude of the mixing is proportional to the mass-squared of the heavy quark in the box diagram and the coupling to the very massive top quark (which helps explain the large size of $B^o\bar{B}^o$ mixing) is absent. The fact that the top cannot appear in the loop diagrams and that only small CKM elements do appear suppresses flavor changing decays such as

those that have been observed in the b sector such as $b \to s\gamma$. Other effects, commonly called 'long range effects', may enhance these processes a little bit in charm but generally predictions based on the Standard Model are quite small.

1.4.2 Charm *CP* Violation

Standard Model CP Violation

Direct *CP* violation in charm decay is expected in the Standard Model (SM) at the few 10^{-3} level [33, 34] (see Table 4). It is significant only for singly Cabibbo-suppressed decays (SCSD), for which tree-level graphs can interfere with penguin diagrams, leading to partial-decay-rate asymmetries, which can occur in either charged or neutral D decays.

As in bottom, these asymmetries reflect interference due to the CKM phase in combination with phase differences from final-state interactions. Experimental evidence suggests substantial final-state effects in charm decay. For example, the mode $D^0 \to K^0\overline{K^0}$ occurs with a branching ratio [37]

$$\frac{B(D^0 \to K^0\overline{K^0})}{B(D^0 \to K^+K^-)} = 0.24 \pm 0.09\,, \tag{46}$$

even though no spectator diagram can produce this final state, and the two possible W-exchange diagrams cancel each other (by the GIM mechanism) to good approximation. This mode could be fed by rescattering of K^+K^- into $K^0\overline{K^0}$. Large final-state effects are also evident in the case of multibody charm decays, where Dalitz-plot analyses reveal appreciable phase differences [38]. These and similar observations underlie the expectation of $\mathcal{O}(10^{-3})$ direct *CP* asymmetries in charm.

At present the best limits on direct *CP* violation in Cabibbo-suppressed charm decay come from Fermilab E687 [39] and E791 [40] and CLEO [41] (Table 4). In fixed-target experiments, to correct for the production asymmetry of D *vs.* $\overline{D}$, the asymmetry in a Cabibbo-suppressed mode is normalized to that observed in the corresponding Cabibbo-favored (CFD) mode; this also has the effect of reducing sensitivity to such systematic effects as trigger, reconstruction, and particle-identification efficiency differences for particles *vs.* antiparticles. In E687 $\approx$10% sensitivity is achieved. By extrapolation from E687, the definitive establishment of an asymmetry of a few 10^{-3} requires $\gtrsim 10^8$ reconstructed D's, to give $\sim 10^6$ reconstructed charged and (tagged) neutral D's in SCSD modes.

Since the asymmetries are measured by taking double ratios, they are intrinsically insensitive to systematic effects. However, at the 10^{-3} level careful attention will still be required to keep systematic uncertainties from dominating.

1.4.3 CP Violation Beyond the Standard Model

For several reasons, the charm sector is an excellent place to look for *CP* violation arising from physics beyond the Standard Model:

Table 4: Sensitivity to high-impact charm physics.*

Topic	Limit†	Reach of "10^8-charm" exp't†	SM prediction
Direct *CP* Viol.			
$D^0 \to K^-\pi^+$	-0.009<A<0.027		≈ 0 (CFD)
$D^0 \to K^-\pi^+\pi^-\pi^+$		few $\times 10^{-4}$	≈ 0 (CFD)
$D^0 \to K^+\pi^-$		$10^{-3} - 10^{-2}$	≈ 0 (DCSD)
$D^+ \to K^+\pi^+\pi^-$		few $\times 10^{-3}$	≈ 0 (DCSD)
$D^0 \to K^-K^+$	-0.11<A<0.16	10^{-3}	$(0.13 \pm 0.8) \times 10^{-3}$
	-0.028<A<0.166		
$D^+ \to K^-K^+\pi^+$	-0.062<A<0.034	10^{-3}	
$D^+ \to \overline{K^{*0}}K^+$	-0.092<A<0.072	10^{-3}	$(2.8 \pm 0.8) \times 10^{-3}$
$D^+ \to \phi\pi^+$	-0.087<A<0.031	10^{-3}	
$D^+ \to \pi^-\pi^+\pi^+$	-0.086<A<0.052	10^{-3}	
$D^+ \to \rho^0\pi^+$			$(-2.3 \pm 0.6) \times 10^{-3}$
$D^+ \to \eta\pi^+$			$(-1.5 \pm 0.4) \times 10^{-3}$
$D^+ \to K_S\pi^+$		few $\times 10^{-4}$	3.3×10^{-3}
Indirect *CP* Viol.			
$D^0 \to \pi^+\pi^-$		few $\times 10^{-3}$	≈ 0
FCNC			
$D^0 \to \mu^+\mu^-$	7.6×10^{-6}	10^{-7}	$< 3 \times 10^{-15}$
$D^0 \to \pi^0\mu^+\mu^-$	1.7×10^{-4}	10^{-6}	
$D^0 \to \overline{K^0}e^+e^-$	17.0×10^{-4}	10^{-6}	$< 2 \times 10^{-15}$
$D^0 \to \overline{K^0}\mu^+\mu^-$	2.5×10^{-4}	10^{-6}	$< 2 \times 10^{-15}$
$D^+ \to \pi^+e^+e^-$	6.6×10^{-5}	few $\times 10^{-7}$	$< 10^{-8}$
$D^+ \to \pi^+\mu^+\mu^-$	1.8×10^{-5}	few $\times 10^{-7}$	$< 10^{-8}$
$D^+ \to K^+e^+e^-$	4.8×10^{-3}	few $\times 10^{-7}$	$< 10^{-15}$
$D^+ \to K^+\mu^+\mu^-$	8.5×10^{-5}	few $\times 10^{-7}$	$< 10^{-15}$
$D \to X_u + \gamma$			$\sim 10^{-5}$
$D^0 \to \rho^0\gamma$	1.4×10^{-4}		$(1-5) \times 10^{-6}$
$D^0 \to \phi\gamma$	2×10^{-4}		$(0.1-3.4) \times 10^{-5}$
LF or LN Viol.			
$D^0 \to \mu^\pm e^\mp$	1.0×10^{-4}	10^{-7}	0
$D^+ \to \pi^+\mu^\pm e^\mp$	3.3×10^{-3}	few $\times 10^{-7}$	0
$D^+ \to K^+\mu^\pm e^\mp$	3.4×10^{-3}	few $\times 10^{-7}$	0
$D^+ \to \pi^-\mu^+\mu^+$	2.2×10^{-4}	few $\times 10^{-7}$	0
$D^+ \to K^-\mu^+\mu^+$	3.3×10^{-4}	few $\times 10^{-7}$	0
$D^+ \to \rho^-\mu^+\mu^+$	5.8×10^{-4}	few $\times 10^{-7}$	0
Mixing			
$(\overline{D^0}) \to K^\mp\pi^\pm$	$r < 0.0037$	$r < 10^{-5}$	
	$\Delta M_D < 1.3 \times 10^{-4}$ eV	$\Delta M_D < 10^{-5}$ eV	10^{-7} eV
$(\overline{D^0}) \to K\ell\nu$		$r < 10^{-5}$	

* Sources for the measurements and predictions in this table may be found in Refs. [35] and [36].

† at 90% confidence level.

- The top-quark loops that in the Standard Model dominate CP violation in the strange and beauty sectors [42] are absent, creating a low-background window for new physics.
- New physics may couple differently to up-type and down-type quarks [43] or couple to quark mass [44].
- Compared to beauty, the large production cross sections [45], the larger branching ratios to states of interest and "self tagging," via D^{*+} decays, allow much larger event samples to be acquired.
- Many extensions of the Standard Model predict observable effects in charm.

Direct CP violation in Cabibbo-favored or doubly Cabibbo-suppressed (DCSD) modes would be a clear signature for new physics [34, 46]. Asymmetries in these as well as in SCSD modes could reach $\sim 10^{-2}$ in such scenarios as non-minimal supersymmetry [46] and in left-right-symmetric models [47, 48]. Bigi has pointed out that a small new-physics contribution to the DCSD rate could amplify the SM K^0-induced asymmetries to $\mathcal{O}(10^{-2})$ as well [46].

1.4.4 Rare Decays

Charm-changing neutral currents are forbidden at tree level in the Standard Model due to the GIM mechanism [49]. They can proceed via loops at rates which are predicted to be unobservably small, *e.g.* for $D^0 \to \mu^+\mu^-$ (which suffers also from helicity suppression in the SM) the predicted branching ratio is $\sim 10^{-19}$ [50, 48, 51], and for $D^+ \to \pi^+\mu^+\mu^-$ it is $\sim 10^{-10}$ [52, 51]. Long-distance effects increase these predictions by some orders of magnitude, but they remain of order 10^{-15} to 10^{-8} [48, 53, 54]. Various extensions of the SM [52, 55] predict effects substantially larger than this, for example in models with a fourth generation, both $B(D^+ \to \pi^+\mu^+\mu^-)$ and $B(D^0 \to \mu^+\mu^-)$ can be as large as 10^{-9} [52]. Experimental sensitivities are now in the range $\sim 10^{-4}$ to 10^{-5} [37, 56, 57, 58, 59] and are expected to reach $\sim 10^{-5}$ to 10^{-6} in E831 [60]. While 10^8 reconstructed charm implies a single-event branching-ratio sensitivity of $\approx 10^{-9}$, FCNC limits are typically background-limited, so sensitivites can be expected to improve as the square root of the number of events reconstructed.

1.4.5 Lepton-number-violating decays

There are two lepton-number-violating effects which can be sought: decays violating conservation of lepton number (LNV) and decays violating conservation of lepton-family number (LFNV). LFNV decays (such as $D^0 \to \mu^\pm e^\mp$) are expected in theories with leptoquarks [55], heavy neutrinos [51], extended technicolor [61], etc. LNV decays (such as $D^+ \to K^- e^+ e^+$ or $\Sigma^+\pi^+ e^-$) can arise in GUTs and have been postulated to play a role in the development of the baryon asymmetry of the Universe [62]. Since no known fundamental principle forbids either type of decay, it is of interest to search for them as sensitively as possible.

Although much smaller decay widths can be probed in K decays, there are simple theoretical arguments why LFNV charm decays are nevertheless worth seeking. For example, if these effects arise through Higgs exchange, whose couplings are proportional to mass, they will couple more strongly to charm than to strangeness [44]. Furthermore, LFNV currents may couple to up-type quarks more strongly than to down-type [55, 63].

As shown in Table 4, the best existing limits come in most cases from the e^+e^- experiments Mark II, ARGUS, and CLEO (although the hadroproduction experiment Fermilab E653 dominates in modes with same-sign dimuons) and are typically at the $10^{-3} - 10^{-4}$ level [58, 59]. E831 expects to lower these limits to $\sim 10^{-6}$ [60], and we estimate sensitivity (in the first year of running) of $\sim 10^{-7}$.

1.4.6 Mixing and Indirect *CP* Violation

$D^0\overline{D^0}$ mixing may be one of the more promising places to look for low-energy manifestations of physics beyond the Standard Model. Mixing has been investigated by looking for the decays $D^o \to K^+\pi^-$ and $D^o \to K^+\pi^-\pi^+\pi^-$. The situation regarding $D^0\overline{D^0}$ mixing is complicated by the presence of Double Cabbibo Suppressed Decays. Since both effects can lead to the same final states, one needs to distinguish them using measurements [44] of the rate *vs* proper time, which tends to reduce the sensitivity. Semileptonic decays offer a way to study mixing free from the effects of DCSD. A preliminary result from E791 using D^*-tagged $D^0 \to Ke\nu$ events indicates sensitivity at the $\approx$0.5% level [64]. Extrapolation of existing limits to 10^8 charm suggests 10^{-4} to 10^{-5} sensitivity.

We also think that it is important to see if we can measure a lifetime difference between CP odd and CP even eigenstates in D^o decay, this is called $\Delta\Gamma$. Although typical extensions of the SM which predict large ΔM_D also predict $\Delta M_D \gg \Delta\Gamma$ [65, 66], from an experimentalist's viewpoint both should be measured if possible. This can be done quite straightforwardly by comparing the lifetime measured for *CP*-even modes (such as $K^+K^-, \pi^+\pi^-$) with that for *CP*-odd modes or (more simply) with modes of mixed *CP* (such as $K^-\pi^+$). Liu has estimated sensitivity at $\sim 10^{-5} - 10^{-6}$ in $y^2 \equiv (\Delta\Gamma/2\Gamma)^2$ [67].

SM contributions to $|\Delta M_D|$ are estimated [34, 68] to give $r_{\rm mix} \sim (\Delta M_D/\Gamma_D)^2 < 10^{-8}$. Many nonstandard models predict much larger effects. Any observation at a substantially higher level will be clear evidence of new physics.[4] An interesting example is the multiple-Higgs-doublet model lately expounded by Hall and Weinberg [71], in which $|\Delta M_D|$ can be as large as 10^{-4} eV, approaching the current experimental limit. In this model K^0 *CP* violation arises from the Higgs sector, and *CP* violation in the beauty sector is expected to be small, which emphasizes the importance of exploring rare phenomena in *all* quark sectors. The large mixing contribution arises from flavor-changing neutral-Higgs exchange (FCNE) [72], which can be constrained to satisfy the GIM mechanism for K^0 decay by assuming small phase factors

[4] Earlier estimates [69] that long-distance effects can give $\Delta M_D/\Gamma_D \sim 10^{-2}$ are claimed to have been disproved [34], though there remain skeptics [46, 70].

($\sim 10^{-3}$).[5] Many other authors have also considered multiple-Higgs effects in charm mixing [63, 74, 75, 76, 77]. Large mixing in charm can also arise in theories with supersymmetry [74, 78], technicolor [61], leptoquarks [55], left-right symmetry [79], or a fourth generation [48, 52].

1.4.7 Other Charm Physics

In addition to searches for effects due to new physics, high-sensitivity charm measurements address a variety of Standard-Model issues. These have been discussed recently by Sokoloff [80], Sokoloff and Kaplan [81], and Wiss [82]. These include

- testing the heavy-quark effective theory;
- measurement of semileptonic form factors;
- study of the CKM matrix with semileptonic decays to measure the CKM-matrix elements V_{cs} and V_{cd}. Currently, $|V_{cd}|$ and $|V_{cs}|$ are known to $\pm 5\%$ and $\pm 15\%$ respectively [42].
- Study of hadronic decays.

[5] This is in distinction to the original "Weinberg model" of *CP* violation [73], in which FCNE was suppressed by assuming a discrete symmetry such that one Higgs gave mass to up-type quarks and another to down-type.

References

[1] The CESR B Physics Working Group, K. Lingel *et al*, "Physics Rationale For a B Factory", Cornell Preprint CLNS 91-1043 (1991); SLAC Preprint SLAC-372 (1991); "Progress Report on Physics and Detector at KEK Asymmetric B Factory," KEK Report 92-3 (1992)

[2] M. Artuso, "Experimental Facilities for b-Quark Physics," in *B Decays* revised 2nd Edition, Ed. S. Stone, World Scientific, Sinagapore (1994).

[3] F. Abe *et al*, *Phys. Rev.* D **53**, 1051 (1996).

[4] M. Mangano, P. Nason and G. Ridolfi, *Nucl. Phys.* B **373**, 295 (1992).

[5] F. Abe *et al*, *Phys. Rev. Lett.* **75**, 1451 (1995). Previous UA1 measurements agreed with the theoretical predictions, see C. Albajar *et al*, *Phys. Lett.* B **256**, 121 (1991). Recent D0 measurements agree with both the CDF measurements and the high side of the theoretically allowed range. See S. Abachi *et al*, *Phys. Rev. Lett.* **74**, 3548 (1995).

[6] N. Cabibbo, *Phys. Rev. Lett.* **10**, 531 (1963); M. Kobayashi and K. Maskawa, *Prog. Theor. Phys.* **49**, 652 (1973).

[7] L. Wolfenstein, *Phys. Rev. Lett.* **51**, 1945 (1983).

[8] S. Stone, "Prospects For B-Physics In The Next Decade," presented at *NATO Advanced Study Institute on Techniques and Concepts of High Energy Physics*, Virgin Islands, July 1996, to be published in procedings.

[9] P. Langacker, "CP Violation and Cosmology," in *CP Violation*, ed. C. Jarlskog, World Scientific, Singapore p 552 (1989).

[10] A. J. Buras, "Theoretical Review of B-physics," in *BEAUTY '95* ed. N. Harnew and P. E. Schlein, *Nucl. Instrum. Methods* **A368**, 1 (1995).

[11] A. Carter and A. I. Sanda, *Phys. Rev. Lett.* 45, 952 (1980); *Phys. Rev.* D23, 1567 (1981); I. I. Bigi and A. I. Sanda, *Nucl. Phys.* B193, 85 (1981); ibid B281, 41 (1987).

[12] I. Bigi, V. Khoze, N. Uraltsev, in **CP Violation**, ed. C. Jarlskog, World Scientific, Singapore 175 (1989).

[13] M. Gronau, *Phys. Rev. Lett.* 63, 1451 (1989); M. Gronau and D. London, *Phys. Rev. Lett.* 65, 3381 (1990).

[14] N. G. Deshpande, X-G. He, *Phys. Rev. Lett.* **75**, 1703 (1995).

[15] M. Gronau and D. Wyler, *Phys. Lett.* B **265**, 172 (1991).

[16] S. Stone, *Nucl. Instrum. Methods* **A333**, 15 (1993).

[17] R. Fleischer, *Phys. Lett.* B **365**, 399 (1996); R. Fleischer and I. Dunietz, *Phys. Lett.* B **387**, 361 (1996). R. Fleischer and I. Dunietz, *Phys. Rev.* D **259**, 1997 (.)

[18] D. Atwood, B. Blok and A. Soni, *Int. J. Mod. Phys.* A11, 3743 (1996); see also N. Deshpande, X. He & J. Trampetic, Preprint OITS-564-REV (1994); see also J. M. Soares, *Phys. Rev.* D53, 241 (1996). G. Eilam, A. Ioannissian R. R. Mendel and P. Singer, *Phys. Rev.* D53, 3629 (1996).

[19] R. Ammar *et al*, "Radiative Penguin Decays of the B Meson," CLEO-CONF 96-6 (1996).

[20] A. Ali, C. Greub and T. Mannel, "Rare B Decays in the Standard Model, " in Hamburg 1992, Proceedings, ECFA Workshop on a European B-meson Factory, Eds. R. Aleksan and A. Ali, p155 (1993).

[21] C. Albajar *et al*, *Phys. Lett.* B262, 163 (1991).

[22] R. Balest *et al*, "Search for $B \to K\ell^+\ell^-$ and $B \to K^*\ell^+\ell^-$ decays," CLEO-CONF 94-4 (1994).

[23] F. Abe *et al*, *Phys. Rev. Lett.* 76, 2015 (1996).

[24] R. Ammar *et al*, *Phys. Rev.* D49, 5701 (1994); M. Artuso, *et al*, *Phys. Rev. Lett.* 75, 785 (1995).

[25] D. Buskulic *et al*, *Phys. Lett.* B343, 444 (1995).

[26] A. Ali and T. Mannel, *Phys. Lett.* B264, 447 (1991). Erratum, ibid, B274, 526 (1992).

[27] M. Gronau and D. Wyler, *Phys. Lett.* B **265**, 172 (1991).

[28] D. Atwood, I. Dunietz and A. Soni, *Phys. Rev. Lett.* **78**, 3257 (1997).

[29] Private communication from I. Bigi and G. Burdman.

[30] M. Golden and B. Grinstein *Phys. Lett.* B **222**, 501 (1989); F. Buccella *et al*, *Phys. Rev.* D **51**, 3478 (1995).

[31] G. Baum *et al.*, CERN-SPSLC-96-14, Mar. 1996.

[32] J. F. Donoghue, B. R. Holstein, and G. Valencia, Int. J. Mod. Phys. A, **2**, 319 (1987).

[33] M. Golden and B. Grinstein, Phys. Lett. B **222**, 501 (1989); F. Buccella *et al.*, Phys. Lett. B **302**, 319 (1993); A. Pugliese and P. Santorelli, in *Proc. Third Workshop on the Tau/Charm Factory*, Marbella, Spain, 1–6 June 1993, Edition Frontieres (1994), p. 387; F. Buccella *et al.*, Phys. Rev. D **51**, 3478 (1995); F. Buccella, M. Lusignoli, and A. Pugliese, Phys. Lett. B **379**, 249 (1996).

[34] G. Burdman, in **The Future of High-Sensitivity Charm Experiments**, D. Kaplan and S. Kwan, *eds.*, FERMILAB-Conf-94/190 (1994) p. 75, and in **Workshop on the Tau/Charm Factory**, J. Repond, *ed.*, Argonne National Laboratory, June 21–23, 1995, AIP Conf. Proc. No. 349 (1996), p. 409.

[35] C. N. Brown *et al.*, "Expression of Interest for a High-Sensitivity Charm Experiment" (1996).

[36] D. M. Kaplan, in *Proc. Conf. on Production and Decay of Hyperons, Charm and Beauty Hadrons*, Strasbourg, France, 5–8 Sept. 1995, Nucl. Phys. Proc. Suppl. **50**, 260 (1996).

[37] R. M. Barnett *et al.*, (Particle Data Group), Phys. Rev. D **54**, 1 (1996).

[38] P. Frabetti *et al.*, Phys. Lett. B **331**, 217 (1994); J. E. Wiss, in **Workshop on the Tau/Charm Factory**, Argonne National Laboratory, June 21–23, 1995, J. Repond, *ed.*, AIP Conf. Proc. No. 349 (1996), p. 345.

[39] P. L. Frabetti *et al.*, Phys. Rev. D **50**, R2953 (1994).

[40] E. M. Aitala *et al.*, submitted to Phys. Rev. Lett. (1996).

[41] J. Bartelt *et al.*, Phys. Rev. D **52**, 4860, (1995).

[42] For a recent review see J. L. Rosner, in *Proc. 8th Jorge Andre Swieca Summer School*, Sao Paulo, Brazil, 5–18 Feb. 1995, p. 116.

[43] A. Hadeed and B. Holdom, Phys. Lett. **159B**, 379 (1985); W. Buchmuller and D. Wyler, Phys. Lett. **177B**, 377 (1986) and Nucl. Phys. **B268**, 621 (1986); M. Leurer, Phys. Rev. Lett. **71**, 1324 (1993).

[44] I. I. Bigi, in **Charm Physics**, *Proc. Int. Symp. on Charm Physics*, Beijing, China, June 4–16, 1987, Gordon and Breach (1987), p. 339.

[45] R. Ammar *et al.*, Phys. Rev. Lett. **61**, 2185 (1988); K. Kodama *et al.*, Phys. Lett. B **263**, 573 (1991); M. J. Leitch *et al.*, Phys. Rev. Lett. **72**, 2542 (1994).

[46] I. I. Bigi, hep-ph/9412227, in **Heavy Quarks at Fixed Target**, *Proc. HQ94 Workshop*, Charlottesville, VA, Oct. 7–10, 1994, B. Cox, *ed.*, Frascati Physics Series (1994), p. 235.

[47] A. Le Yaouanc, L. Oliver, and J.-C. Raynal, Phys. Lett. B **292**, 353 (1992); M. Gronau and S. Wakaizumi, Phys. Rev. Lett. **68**, 1814 (1992); A. Le Yaouanc *et al.*, LPTHE-Orsay/95-15, hep-ph/9504270 (1995).

[48] S. Pakvasa, in **The Future of High-Sensitivity Charm Experiments**, D. Kaplan and S. Kwan, *eds.*, FERMILAB-Conf-94/190 (1994), p. 85.

[49] S. L. Glashow, J. Iliopoulos, and L. Maiani, Phys. Rev. D **2**, 1285 (1970);
S. L. Glashow and S. Weinberg, Phys. Rev. D **15**, 1958 (1977);
E. A. Paschos, Phys. Rev. D **15**, 1966 (1977).

[50] M. Gorn, Phys. Rev. D **20**, 2380 (1979).

[51] J. L. Hewett, "Searching for New Physics with Charm," SLAC-PUB-95-6821, hep-ph/9505246, to appear in *Proc. LISHEP95 Workshop*, Rio de Janeiro, Brazil, Feb. 20–22, 1995.

[52] K. S. Babu *et al.*, Phys. Lett. B **205**, 540 (1988);
T. G. Rizzo, Int. J. Mod. Phys. **A4**, 5401 (1989).

[53] A. J. Schwartz, Mod. Phys. Lett. **A8**, 967 (1993).

[54] G. Burdman, E. Golowich, J. L. Hewett, and S. Pakvasa, Phys. Rev. D **52**, 6383 (1995).

[55] W. Buchmuller and D. Wyler, Phys. Lett. **177B**, 377 (1986) and Nucl. Phys. **B268**, 621 (1986);
M. Leurer, Phys. Rev. Lett. **71**, 1324 (1993).

[56] E. M. Aitala *et al.*, Phys. Rev. Lett. **76**, 364 (1996).

[57] M. Adamovich *et al.*, Phys. Lett. B **353**, 563 (1995).

[58] P. D. Sheldon, "Searching for *CP* Violation, Flavor Changing Neutral Currents, and Lepton Number Violation in Charm Decay," in **The Future of High-Sensitivity Charm Experiments**, *op. cit.*, p. 25.

[59] K. Kodama *et al.*, Phys. Lett. B **345**, 85 (1995).

[60] J. Cumalat, "Fermilab Fixed-Target Charm Program," in **Proceedings: The Tau-Charm Factory in the Era of B-Factories and CESR**, Stanford Linear Accelerator Center, Stanford, CA, Aug. 15–16, 1994, L. V. Beers and M. L. Perl, *eds.*, SLAC-Report-451 (1994), p. 335.

[61] E. Eichten, I. Hinchliffe, K.D. Lane, and C. Quigg, Phys. Rev. D **34**, 1547 (1986).

[62] A. D. Sakharov, Pis'ma Zh. Eksp. Teor. Fiz. **5**, 32 (1967) [JETP Lett. **5**, 24 (1967)];
E. W. Kolb and M. S. Turner, "Baryogenesis," in **The Early Universe**, Addison-Wesley, 1990, p. 157.

[63] A. Hadeed and B. Holdom, Phys. Lett. **159B**, 379 (1985).

[64] A. Tripathi, "A Search for $D^0 - \overline{D^0}$ Mixing in the Mode $D^0 \to K^- e^+ \nu_e$ ($\overline{D^0} \to K^+ e^- \bar{\nu}_e$)," presented at the *General Meeting of the American Physical Society*, Washington, DC, April 18–21, 1995.

[65] G. Blaylock, A. Seiden, and Y. Nir, Phys. Lett. B **355**, 555 (1995).

[66] T. E. Browder and S. Pakvasa, Phys. Lett. B **383**, 475 (1996).

[67] T. Liu, "The $D^0 - \overline{D^0}$ Mixing Search – Current Status and Future Prospects," in **The Future of High-Sensitivity Charm Experiments**, *op cit.*, p. 375, and
T. Liu, Ph.D. Thesis, Harvard University, HUHEPL-20 (1995).

[68] See also Ref. [69]; J. F. Donoghue *et al.*, Phys. Rev. D **33**, 179 (1986); H. Georgi, Phys. Lett. B **297**, 353 (1992); and T. Ohl, G. Ricciardi, and E. H. Simmons, Nucl. Phys. **B403**, 605 (1993).

[69] L. Wolfenstein, Phys. Lett. **164B**, 170 (1985).

[70] L. Wolfenstein, Phys. Rev. Lett. **75**, 2460, (1995).

[71] L. Hall and S. Weinberg, Phys. Rev. D **48**, R979 (1993); such models were previously considered by S. Pakvasa and H. Sugawara, Phys. Lett. **73B**, 61 (1978); S. Pakvasa *et al.*, Phys. Rev. D **25**, 1895 (1982); T. P. Cheng and M. Sher, Phys. Rev. D **35**, 3484 (1987); and M. Shin, M. Bander, and D. Silverman, in *Proc. Tau-Charm Factory Workshop*, Stanford Linear Accelerator Center, Stanford, CA, May 23–27, 1989, SLAC-Report-343, p. 686.

[72] Y. L. Wu and L. Wolfenstein, Phys. Rev. Lett. **73**, 1762 (1994) and references therein.

[73] S. Weinberg, Phys. Rev. Lett. **37**, 657 (1976).

[74] A. Datta, Phys. Lett. **154B**, 287 (1985).

[75] I. I. Bigi and A. F. Sanda, Phys. Lett. B **171**, 320 (1985).

[76] L. F. Abbott, P. Sikivie, and M. B. Wise, Phys. Rev. D **21**, 1393 (1980);
V. Barger, J. L. Hewett, and R. J. N. Phillips, Phys. Rev. D **41**, 3421 (1990);
J. L. Hewett, Phys. Rev. Lett. **70**, 1045 (1993).

[77] I. I. Bigi, F. Gabbiani, and A. Masiero, Z. Phys. **C48**, 633 (1990).

[78] Y. Nir and N. Seiberg, Phys. Lett. B **309**, 337 (1993).

[79] A. S. Joshipura, Phys. Rev. D **39**, 878 (1989).

[80] M. D. Sokoloff, "Prospects for Very High Statistics Fixed-Target Charm," presented at the *Int. Symp. on Heavy Flavours*, Pisa, Italy, June 6–10, 1995.

[81] M. D. Sokoloff and D. M. Kaplan, "Physics of an Ultrahigh-Statistics Charm Experiment," hep-ex/9508015, in **Heavy Quarks at Fixed Target,***Proc. HQ94 Workshop*, Charlottesville, VA, Oct. 7–10, 1994, B. Cox, *ed.*, Frascati Physics Series (1994), p. 411.

[82] J. E. Wiss, "Charm Decay in Fixed Target: Present and Future," in **Workshop on the Tau/Charm Factory**, Argonne National Laboratory, June 21–23, 1995, J. Repond, *ed.*, AIP Conference Proceedings No. 349 (1996), p. 345.

[83] J. Alexander, "$B \to K\pi$, $\pi\pi$, KK", presented at "Hawaii Conf. on B Physics and CP Violation," Honolulu, Hawaii, March 24-27, 1997.

2 C0 Baseline Detector Description

The C0 program goals include detector R&D towards an eventual state of the art B-physics detector and doing 'competitive' charm and B-physics along the path to this ultimate goal during collider Run II. Below, we describe a detector, which is compatible with the C0 interaction region (IR), which can achieve these goals. Various options for staged implementations which still lead to an excellent detector that can do significant physics are discussed further on in this EOI.

The challenges for any future hadron collider B experiment are:

- To achieve high efficiency in the hostile and complex environment of a hadron collider. This requires the effective and aggressive use of the most modern technologies.
- To represent a significant step beyond what will be achieved by the upcoming generation of B experiments and their possible extensions and upgrades.
- To be competitive with e^+e^- experiments running on the $\Upsilon(4S)$ and other hadron collider experiments which could be taking data in the same time frame. In the case of BTeV, the 'long-term' competition is LHC-B.

Over the last year, BTeV/C0 has begun to take shape based on an understanding of what needs to be done to meet these challenges. These are the key design features of BTeV/C0:

- a dipole located on the IR, which gives BTeV an effective 'two arm' acceptance;
- a precision vertex detector based on planar pixel arrays;
- a vertex trigger at Level I which makes BTeV very efficient for many final states, even if they have no leptons in them; and
- excellent particle identification. Especially important is the requirement of very good charged hadron identification. Many of the states that will be of interest in this phase of bottom and charm physics will only be separable from other states if this capability exists. Also, it will allow for the possibility of kaon tagging. Muon and electron identification are important for tagging and for studies of decay modes involving leptons, too.

The parameters of the Tevatron that must be taken into account in creating a design for meeting these challenges are given in Table 5. A schematic of the experiment is given in Fig. 16. We now discuss the key elements of the baseline design.

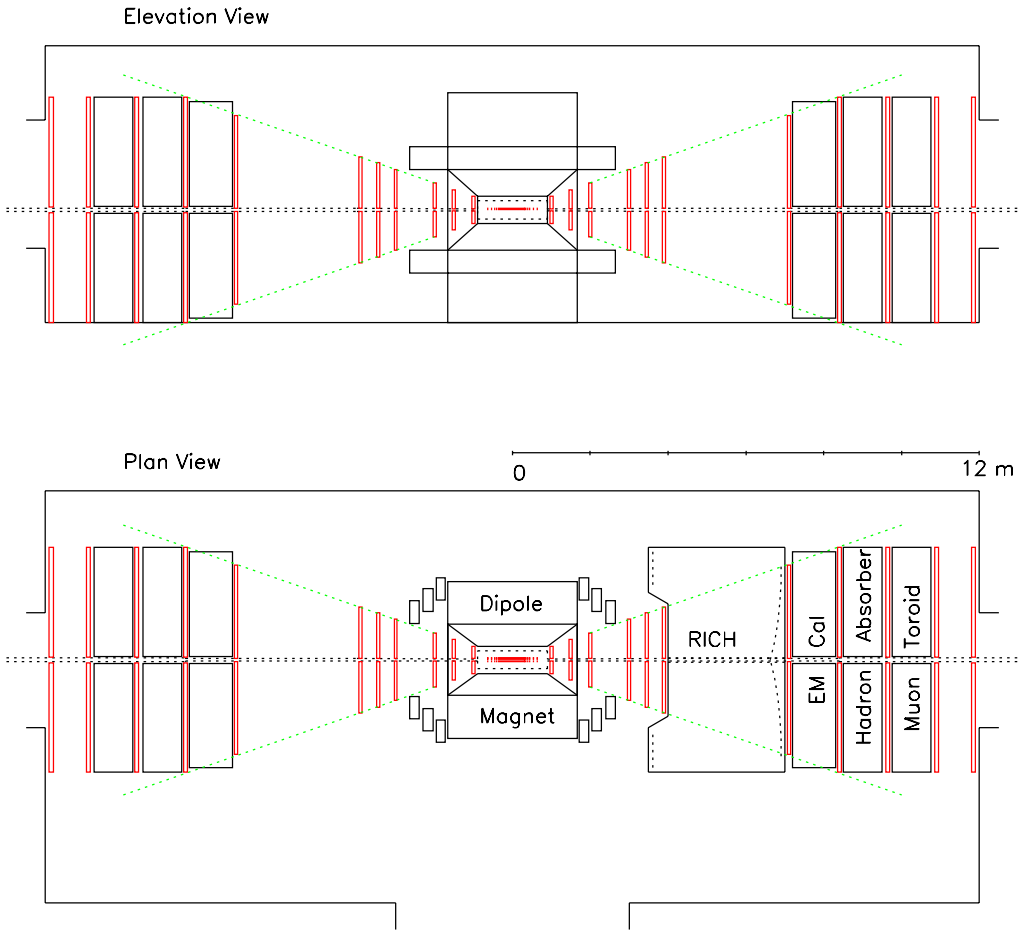

Figure 16: Layout of BTeV/C0 Spectrometer

Table 5: A Few Key Parameters Relevant to BTeV/C0 in Fermilab Collider Run II.

Property	Value
Luminosity(BTeV/C0 physics)	5×10^{31}
Luminosity(full BTeV)	2×10^{32}
Bunch Spacing	132 ns
Length of Luminous Region(initial)	σ_z=30 cm
Length of Luminous Region(final)	σ_z <30 cm
Transverse X dimensions	$\sigma_x = 40\mu$m
Transverse Y dimensions	$\sigma_y = 40\mu$m
Interactions/crossing(BTeV/C0)	mean = $\sim$0.5
$b\bar{b}$ cross section	100 μbarn
$\sigma_{b\bar{b}}/\sigma_{inel}$	$\sim 2\times10^{-3}$

2.1 The C0 Experimental Area

The experiment will be carried out in a new experimental hall to be built in the C0 interaction region. There is an assembly hall to the East of the enclosure where detector components can be assembled and moved into the enclosure through a 20' × 20' 'shield door'. The C0 enclosure and assembly area establish the physical boundary conditions for the experiment. The hall is designed to extend ±40' along the beam on either side of the interaction region. In plan view, the hall is asymmetric with respect to the beam, extending 12' from the beam on the side away from the assembly area to 18' from the beam on the side towards the assembly area. The Tevatron beam height is 100" and the ceiling height is 14' above the beam line. Figure 17 shows a layout of the hall with the proposed baseline detector.

Detector elements are brought into the area at a ground level loading dock. They can be lowered to the assembly area floor using a 30 ton crane which covers the loading dock and the assembly hall. There is no crane in the beam enclosure; all detector elements must be designed so they can be constructed or staged in the assembly area and moved through the shielding door into the enclosure. During operation the shielding door is sealed with concrete blocks for radiation protection purposes. The blocks are stored in the south end of the assembly area in an alcove when the door is open.

There are cable ducts from the experiment enclosure to a 1000 square foot electronics room at grade level on the north end of the assembly area. It is intended that this area will be extended at a later time to become a full counting room. Electrical, air handling, and other utilities have been sized to accommodate the BTeV proposal.

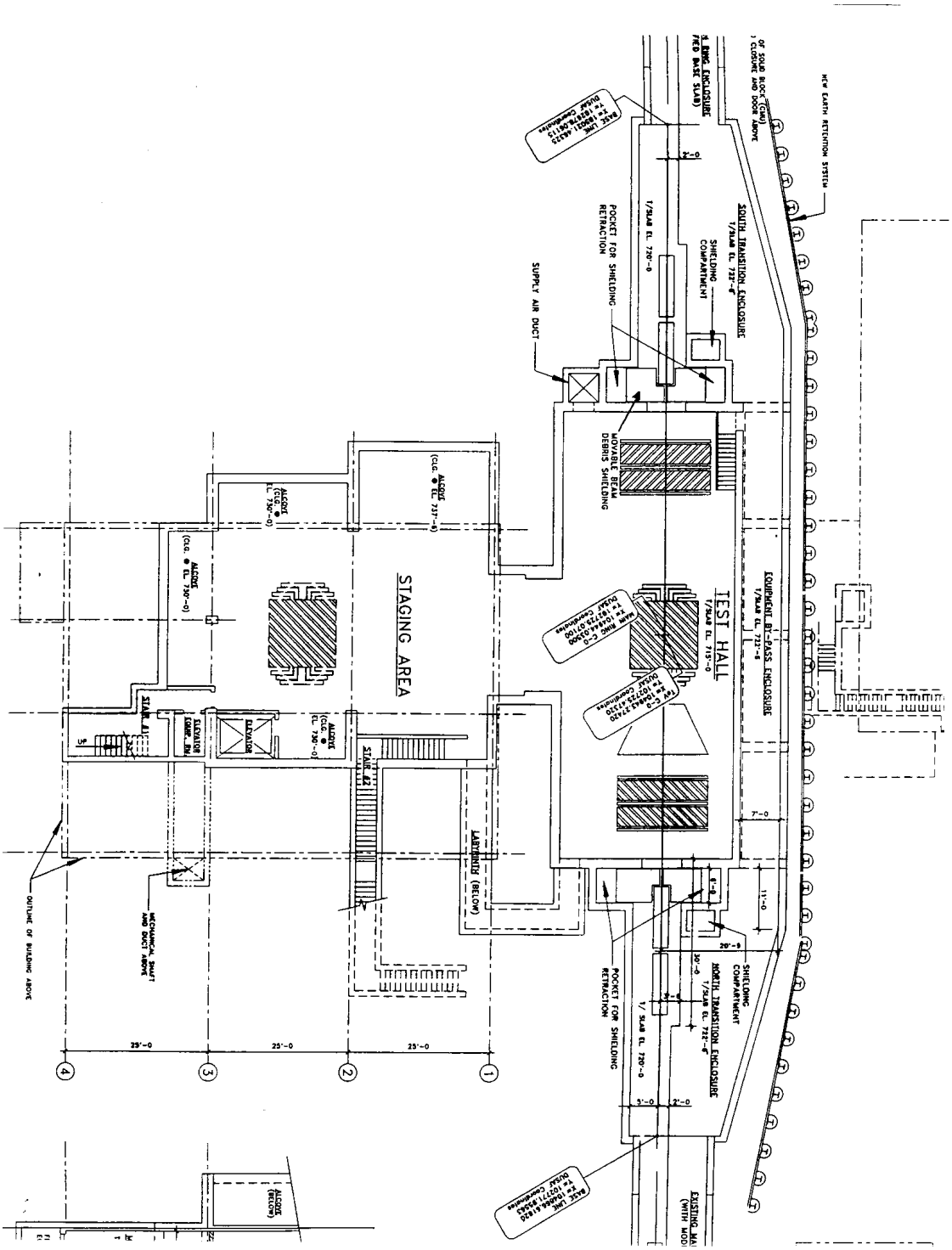

Figure 17: Layout of C-0 Test Area

2.2 The BTeV/C0 Spectrometer Magnet

We have identified a magnet that satisfies the specifications for the BTeV/C0 spectrometer. The SM3 magnet, currently part of the Fermilab MEast spectrometer, is shown on the proposed layout, Fig. 16, of the BTeV/C0 spectrometer. This magnet was assembled in 1981 from soft iron blocks recovered from the decommissioned Nevis Cyclotron. The coils for the magnet were built of 5 cm square aluminum conductor by the Sumitomo Corporation under the aegis of the US-Japan Agreement on High Energy Physics. The magnet has operated in MEast for 15 years, at a central field of about 0.8 Tesla, serving experiments E605, E772, E789, and E866. It is available at the end of the present fixed target run, September, 1997.

The SM3 magnet was assembled by welding together, in place, various blocks of steel. It has a total weight of 500 metric tons. The as-built drawings for this magnet have been studied and a preliminary scheme has been developed for disassembling and modifying the magnet so that it can be reassembled in the C0 assembly hall and rolled into the collision hall, as shown in Fig. 17.

The central field specified for the BTeV/C0 spectrometer is much higher than the current operating excitation of the SM3 magnet. Preliminary studies with a magnetostatic modeling program have led to a redesigned pole-piece insert for SM3. This insert, indicated in Fig. 18, will yield a central field of 1.6 Tesla with acceptable uniformity for insertion into the Tevatron lattice. In this design the magnet would draw 650 kW of power at 4200 amps, its present operating point (it is powered by two 500 kW Transrex power supplies). The properties of the magnet, with the pole faces shimmed to the BTeV requirements, are shown in Table 6.

Table 6: BTeV/C0 Vertex Dipole Properties

Property	Value	Comment
$\int B \times dl$	5.2 T-m	2.6 T-m on each side of center of IR
Central Field	1.6 Tesla	
Effective Length	3.1 m	
Steel Length	3.2 m	
Overall length	5.3 m	
Vertical Aperture	$\pm$0.3 m	shimmed region
Horizontal Aperture	$\pm$0.3 m	shimmed region
Spectrometer Vert. aperture	$\pm$0.3 rad	
Spectrometer Horz. aperture	$\pm$0.3 rad	

The magnet is centered on the interaction region in Z thus creating both an 'upstream' and 'downstream' spectrometer. In quark-antiquark production at 2 TeV, the bottom quark and antiquark are usually either both boosted upstream or both boosted downstream. Thus having two spectrometers doubles

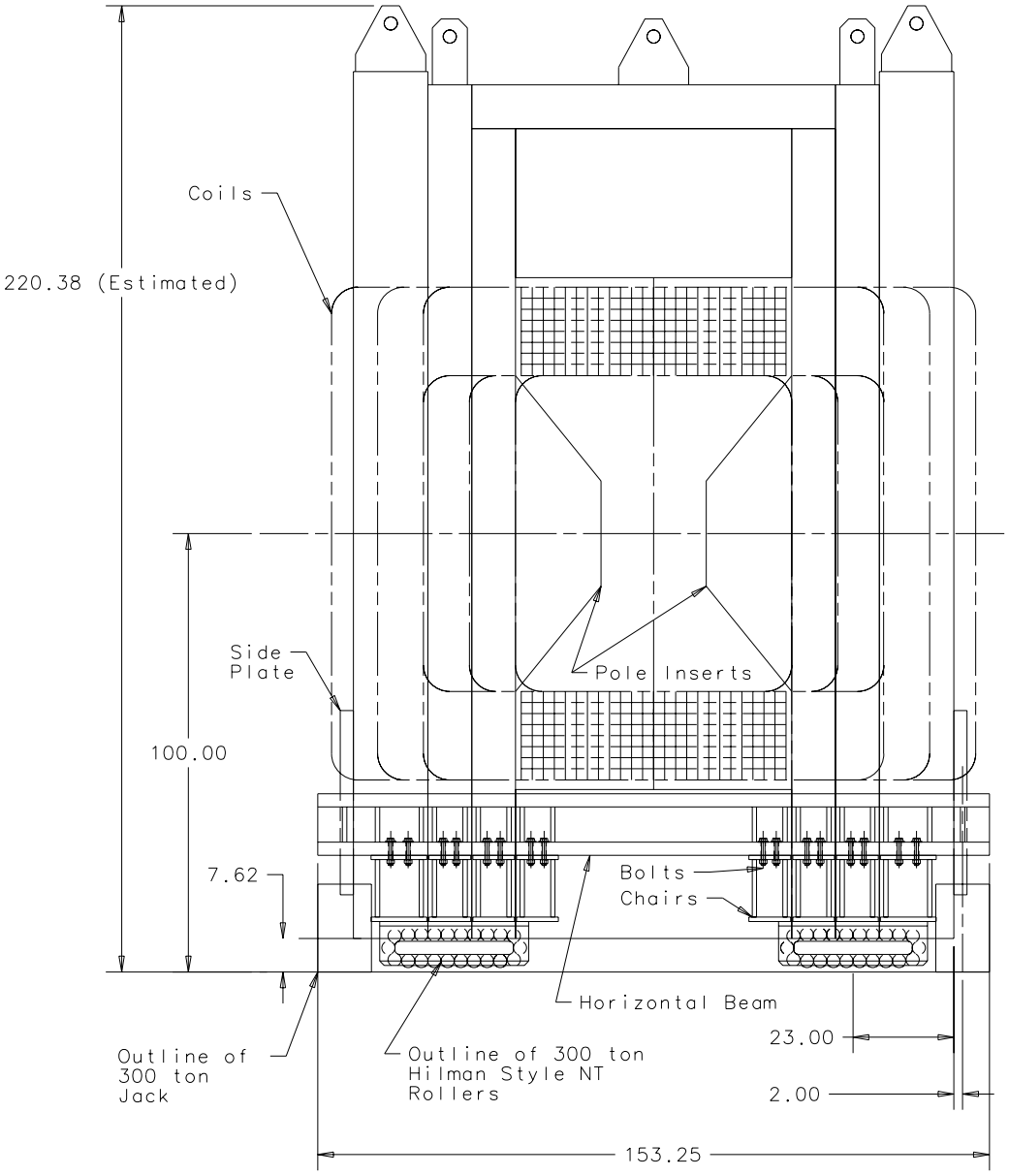

Figure 18: Cross section of the modified SM3 dipole with rollers and pole piece inserts. All dimensions are in inches.

the acceptance of the experiment for tagged decays. Having two spectrometers further improves the experiment because the extended coverage increases the number of tracks from the underlying event that can be used to determine the primary vertex. Fig. 19 shows the number of high energy primary tracks (low multiple scattering) that contribute to locating the primary vertex for single arm coverage and for two arm coverage. If we require three such tracks to determine the primary vertex, then 2.2 times more events survive with two arms than with one, and the primary vertex resolution is enhanced.

In this central dipole geometry, there is a strong magnetic field at the vertex detector. Because of the excellent spatial resolution of the vertex detector, it is possible to get a crude measurement of the track momentum using the vertex detector alone. This measurement can be used to reject tracks at the trigger level that are at such low momentum that multiple coulomb scattering errors make their assignment to a vertex uncertain.

The second spectrometer arm will also be useful during the R&D and early data-taking phases of the experiment. It is almost certain, given the lab's budget, that only one arm will be fully instrumented initially. The other side can be used to test new detector concepts or to test prototypes of production components under actual beam conditions until it becomes possible to instrument it fully.

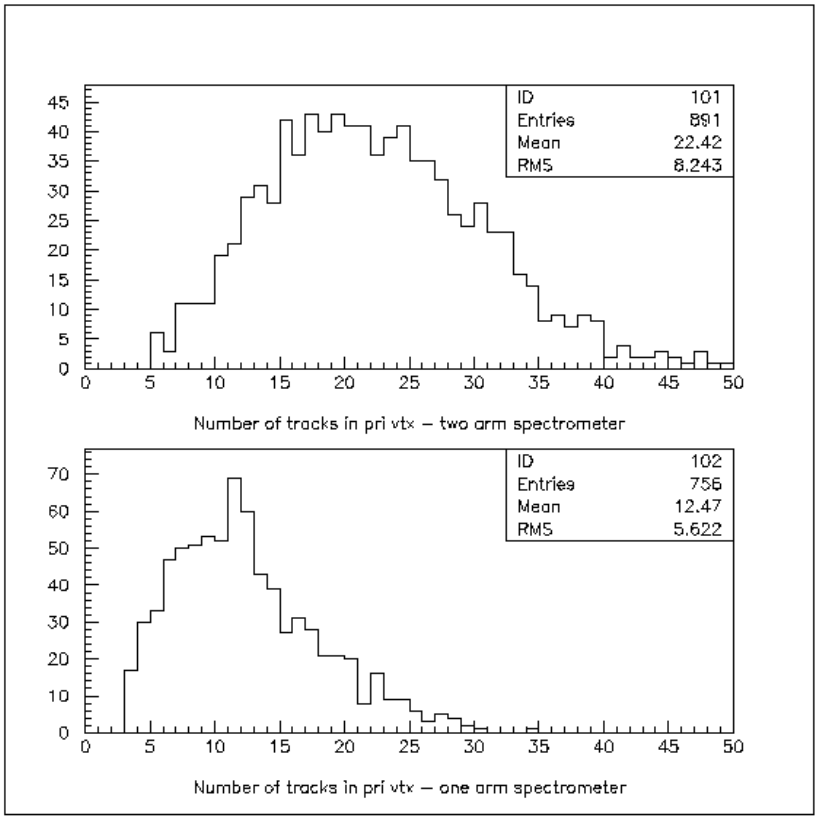

Figure 19: Fraction of events with N primary tracks above 1 GeV/c momentum for a) a dipole centered on the IR giving an effective two-arm acceptance and b) a single forward spectrometer arm.

2.3 Tracking System

The tracking system is designed to reconstruct tracks and measure their angles and momenta over the full aperture (± 300 mr $\times \pm$ 300 mr) and momentum acceptance (from 1 GeV/c to more than 100 GeV/c) of the experiment in both collider and fixed target modes. The main requirements that have to be satisfied by the system are:

- It has to provide adequate resolution on track positions, at least 10μm, and angles, at least 0.1 mr, to separate with high efficiency and robustness the secondary vertices of bottom and charm decays from the primary interaction vertex;
- It has to provide sufficient momentum resolution, about 1% at 100 GeV/c, to permit the reconstruction of the invariant mass of multibody bottom and charm decays with good precision;
- It has to be able to deliver its information to a Level I trigger processor which implements a trigger based on detached vertices or tracks with large impact parameters;
- It must successfully handle the rates and tolerate the radiation doses expected in the experiment.

To satisfy these requirements, the experiment will employ two tracking systems which work together to provide efficient track reconstruction, excellent vertex resolution, and excellent momentum and mass resolution. These are

- The vertex detector which provides the precise vertex measurement and also has momentum measurement capability. The signals from the vertex detector provide the main input to the Level I vertex trigger.
- The downstream tracker, which provides, along with the vertex detector, precision momentum measurement. It also permits us to reconstruct tracks from K_s^o's and Λ's, which often decay downstream of the vertex detector.

In the following paragraphs, we discuss the design of each of these systems.

2.3.1 Vertex Detector

The vertex pixel detector provides the high resolution tracking near the interaction which is required to associate tracks to their proper vertices – primary and secondaries. In designing a vertex tracking system, one must consider the long interaction region of the Tevatron which has a σ_z of 30 cm. This forces one to have a rather long vertex detector. In addition, the detector must be placed very close to the interaction region in order to achieve good resolution and acceptance; so radiation damage is an issue. In a wire geometry, a much shorter detector is sufficient. In this experiment, the vertex detector will be

used in the Level I trigger to select events with secondary vertices. This places special requirements on the detector and its readout.

The baseline BTeV inner tracking system uses planar arrays of silicon pixel detectors placed at intervals along the IR and upstream and downstream of it (to catch tracks coming from the end of the IR). Silicon pixel detectors are chosen because of:

- their superior signal to noise (expected to be better than 100 to 1 for 300μm thick detectors) as compared to other solutions such as silicon strips;
- their excellent spatial resolution. This includes the ability to improve the spatial resolution by measuring the charge sharing between adjacent pixels;
- their low occupancy due to the large number of channels;
- their intrinsically better pattern recognition capabilites compared to strip detectors;
- their speed of response; and
- their reasonable radiation hardness.

It is especially important for the trigger, which operates within strict time constraints, that the number of spurious noise hits be as low as possible. Also, the system must not produce pattern recognition ambiguities or ghost tracks which would take extra time to sort out at the trigger level. The two dimensional nature of the pixels is an enormous help in this regard.

The baseline vertex detector, shown in Fig. 20, has rectangular 30μm by 300μm pixel detectors. It has triplets of planes distributed along the IR separated by about 3.2 cm. The individual planes are composed of four 5cm $\times$ 5cm detectors. Acceptance studies show that this is an adequate size for these detectors. They are mounted above and below the beam so that a small vertical gap is left for the beams to pass through.

Each triplet consists of one wafer that measures the bend view, one that measures the non-bend view, and a third that measures the bend view again. The reason for this particular arrangement of pixel orientations is related to the trigger and is discussed below in the trigger section. One can actually derive a crude momentum measurement using information from three or four triplets. If the pulse height is read out and made available to the trigger, charge sharing can be used to improve the momentum resolution. The momentum information can be used to reject very soft tracks that would adversely affect the trigger algorithm because of Multiple Coulomb Scattering.

With this configuration, the point resolution is expected to be between 5μm and 9μm, depending on how successful the pulse height interpolation is. The angular resolution (without taking multiple scattering into account) is of the order of 0.1 mr. As noted above, the pixel detector does quite a respectable job of

measuring momentum without any assistance from the downstream spectrometer. For example, for a track which passes through ten stations, the resolution is

$$\frac{\sigma_p}{p} = 2\% \times \frac{p}{10 \text{ GeV/c}} \tag{47}$$

where p is the momentum in GeV/c.

The implementation of this system will be very challenging. Because pixel information must be made available to the trigger, a custom electronic design is necessary. There are also significant mechanical (e.g. alignment and support) and thermal issues that must be addressed. The detector must be shielded electronically from the circulating beam which is a significant rf source. It will be enclosed in a secondary vacuum, isolated from the main accelerator vacuum, by a thin aluminum vacuum container. The silicon should be as close to the beam as possible. At 5×10^{31}, a gap of $\pm$6mm will result in the innermost edge of the detector receiving a fluence of close to 0.5×10^{14} per year so that the inner two centimeters of the detector may have to be replaced once every four years. The detector needs to be retractable to a distance of 2 cm from the beam while the collider is being filled and until acceleration is complete.

Table 7 summarizes the properties of the pixel detector.

While pixel detectors have been successfully operated in HEP experiments, no pixel detectors of the proposed size which operate at the high rates we will experience in BTeV and which can provide signals to the first level trigger have yet been built. A substantial R&D effort will be required to meet the BTeV specifications. Although the BTeV pixel detector is unique, pixel detectors are necessary for several other experiments and much work is going on all over the world which we can take advantage of.

We recognize that the design presented here is very challenging. We are studying ways of reducing the technical requirements while incurring only minimal loss of physics reach.

2.3.2 Downstream tracker

The purpose of the downstream tracker is

- To provide better momentum measurements for tracks. This includes tracks which pass through several silicon stations but which have high momentum so that the silicon tracker itself does not provide good resolution; tracks, typically with low momentum, which travel at steep angles and exit the silicon system before traversing many planes; and tracks, typically with high momentum, which travel at small angles and strike only a few silicon planes at the downstream end of the system.

- To provide the only momentum measurements for important classes of tracks which do not pass through the vertex detector. The most important such class consists of K_s's and Λ's which decay downstream of the silicon. K_s's are daughter particles in some of the most important bottom and charm decays.

Table 7: Properties of Baseline Pixel Vertex Detector

Property	Value
Pixel size	rectangular: 30μm × 300μm
Quadrant size	5cm × 5cm
Plane Dimensions– upper half	10cm × 5cm
Plane Dimensions– lower half	10cm × 5cm
Central (vertical) gap	adjustable
	nominal setting in collider mode is ±6mm
Total Planes	93
Total Stations	31 each consisting of
	three planes
Pixel orientations	the outer two with narrow
	pixel dimension vertical
	the middle one with narrow
	pixel dimension horizontal
Separation of Stations	3.2 cm
Plane to plane separation	4 mm
(within station)	
Total Plane Thickness	500 μm
(incl cooling, supports)	
Station Thickness	1700 μm equivalent
(incl. Al shielding skin)	
Total Pixels	10^8
Total Silicon Area	$\approx 1\text{m}^2$
Readout	possible analog readout
Trigger	signals are used in Level I trigger
Rate requirements	beam crossing rate is 132 ns.
Deadtime	$<3\%$ at $5\times10^{31}\text{cm}^{-2}\text{s}^{-1}$
Noise requirement	desired: $< 10^{-5}$ per channel
	required: $< 10^{-4}$ per channel
Power per pixel	<40 μWatt

- To confirm and locate the track at the entrance (and exit) to the particle identification system, the EM calorimeter, and the muon system. In particular, this system allows one to flag charged tracks that interacted or decayed within the spectrometer volume.

The baseline technology for this detector is planes of straw tubes. Another possibility is conventional drift chambers. The requirement on the spatial resolution is about 100-150μm per plane. The detector will be divided into quadrants for ease of removal from the beam for servicing.

The baseline system has seven stations of straw tubes distributed along both arms of the spectrometer as shown in Fig. 21. A single station has three sets of straws directed along the three views: X, Y, and U (U is at 45^o from X). Each set in a station is made up of four layers of parallel straws.

The chambers are placed at ±96 cm, ±146 cm, ±196 cm, which is just at the downstream end of the magnet, ±296 cm, ±341 cm, ±386 cm, which is at the entrance to the RICH, and at ±706 cm, which is just after the RICH and before the EM calorimeter. The chambers upstream and downstream of the RICH provide an accurate location for the center of the Cerenkov rings. The geometry has not yet been optimized because we have not yet studied how to best exploit the fringe field of the analysis magnet for neutral Vee finding but we believe this configuration performs quite well.

Details of the downstream trackers are given in Table 8.

Table 8: Properties of the Downstream Tracker

Property	Value
Straw size	4mm diameter
Central hole	5 cm diameter
Total Stations	7 each (forward/backward)
Z positions (cm)	96, 146, 196, 296, 341, 386, 706
Quadrant size(cm)	30, 45, 60, 90, 105, 118, 210
Total Views per station	3
Total Layers per view	4
Total Straws	$\approx 10^5$
Total Station Thickness	$< 1\%$ X_0 per station
Readout	TDCs (6 bits)
Rate requirements	beam crossing rate is 132 ns.

If we assume that we can achieve a resolution of 100μm in the bend view at each station, the momentum resolution of a track originating in the vertex detector and reaching the last station of straws can be measured with an accuracy of better than 1% at 100 GeV/c.

Figure 22a shows the momentum resolution obtained using only the pixel information from 10 GeV/c tracks coming from the center of the IR and reaching the last straw chamber vs the number of pixel planes traversed. Figure 22b shows the momentum resolution for the same tracks using both the pixel detectors and the straw chambers vs the number of pixel planes traversed. It is clear that the precision momentum measurement comes from the straw tube system and is independent of the number of pixel planes traversed.

Figure 23a shows the z distribution of decay vertices for K_s^o's and Fig. 23b shows the K_s^o mass peak obtained with this tracking system.

Since the downstream tracker is used to improve the momentum resolution for wide-angle, low momentum tracks which only pass through a few silicon planes, it is important that these tracks pass through very little material after they exit the silicon. Since we are not certain at this time how much material will be in this region (electronics and cooling), we do not know whether this will be a problem. If it turns out that the material is large enough to seriously degrade the momentum resolution, we can recover it by inserting a large silicon plane, which could be based on silicon microstrips rather than pixels, to measure

the bend view coordinate right at the downstream ends of the silicon vertex detector. These planes need to be ± 20 cm $\times$ ± 20 cm and need a strip width of 50-100μm. Their z-position would be ± 64 cm. These planes give us a precision point to use in conjunction with the downstream tracker's measurements and to make use of all the field from 64 cm to the ends of the dipole field. At present, these planes are not included in our simulation nor is there any material in the region outside of the vertex detector transversely.

2.3.3 Options

Diamond Pixel Option

Diamond pixel detectors could have significant advantages over silicon pixel detectors but are in an earlier stage of development. The recombination length of diamond is still at the level of 100μm. The resulting signal is about a factor of four lower than that of silicon. Research on improving the signal collection continues. Properties of diamond that make it superior to silicon if sufficient pulse height can be obtained are:

- lower radiation length leading to lower multiple scattering;
- better radiation hardness; and
- better thermal conductivity which leads to simpler cooling schemes which can result in less material in the detector.

Wide Angle Tracker Option

There are other ideas for enhancements to the tracking system which will extend the acceptance of the detector and/or will improve the trigger. For example, we have begun the study of the wide angle tracking system shown in figure 24. The primary purpose of this system would be to facilitate the vertex trigger by providing information which could be used to quickly locate the primary interaction point or points. Using generator-level information from both minimum bias and b events, we have determined that in a very large fraction of events, enough information is contained in the wide angle tracker to enable it to locate the primary interaction with sub-millimeter precision. We are very encouraged by this result and intend to follow up with a more complete design and a hit-level simulation.

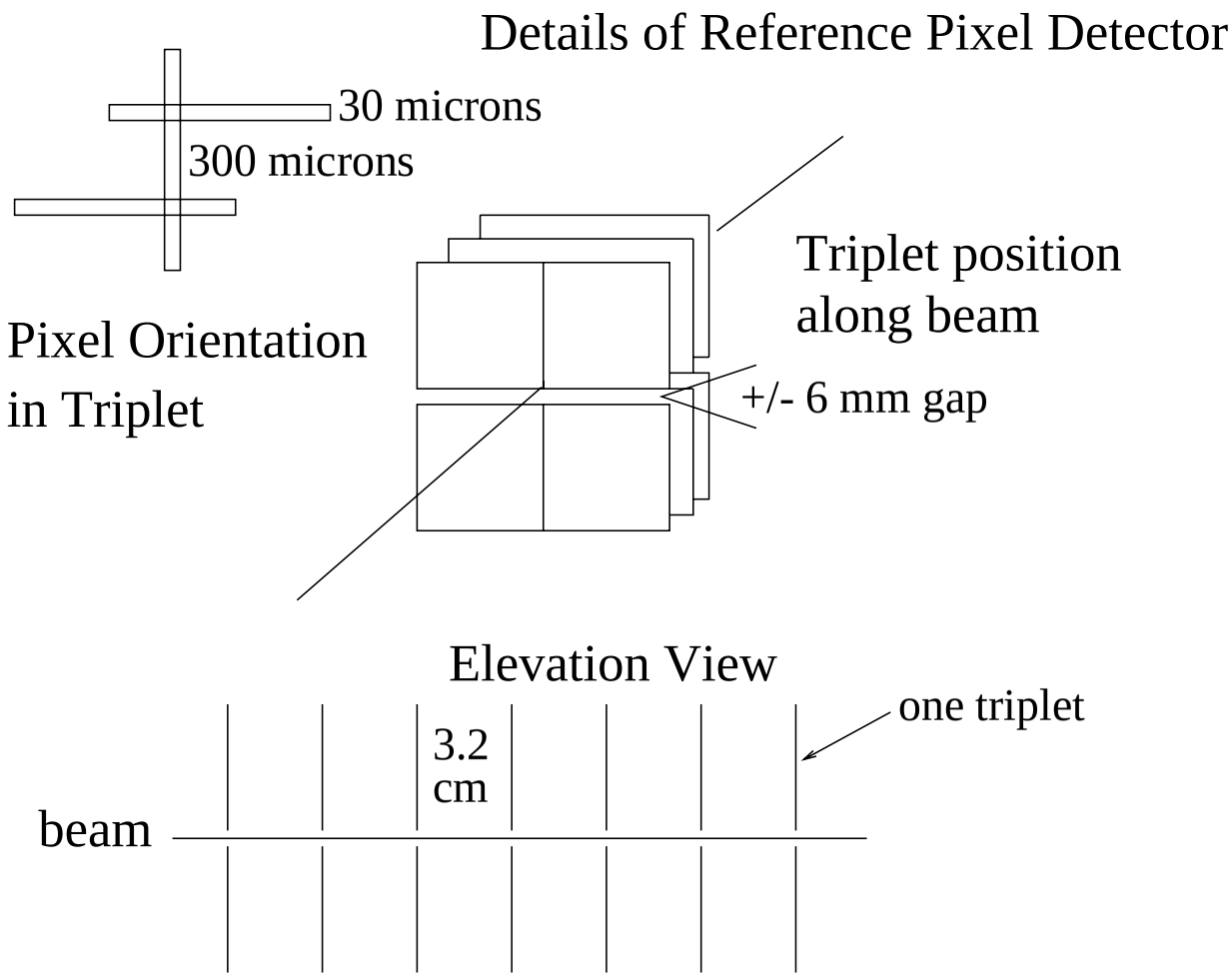

Figure 20: Baseline pixel vertex detector

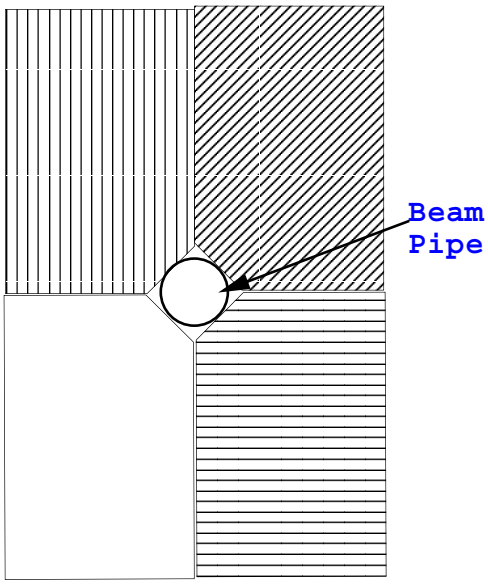

Figure 21: Details of 'downstream' tracker. Shown are the location of the four quadrants with respect to the beam pipe. Also shown are the three views, which are actually in complete planes each offset in z from the others.

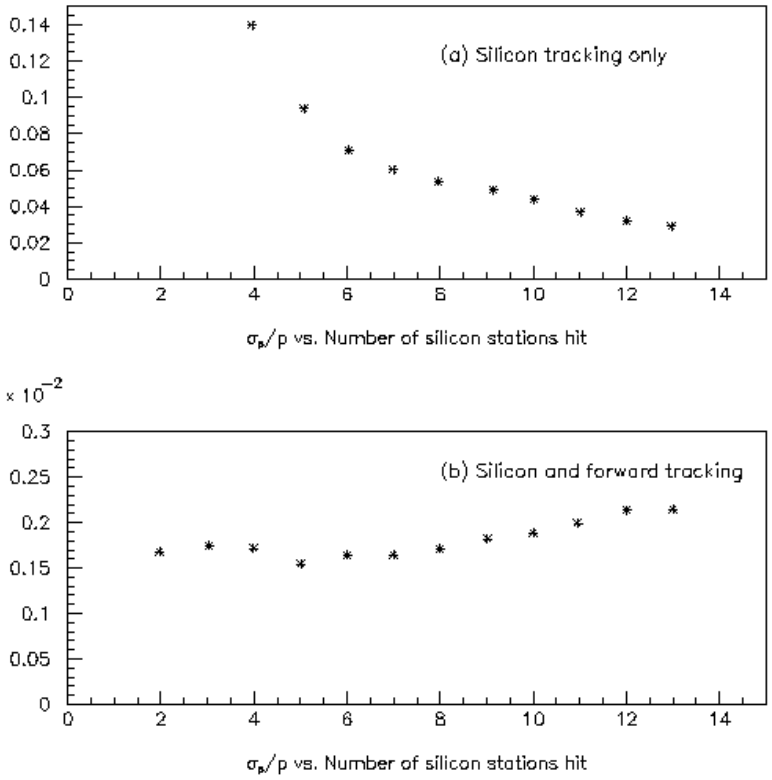

Figure 22: Momentum Resolution for a 10 GeV/c particle vs the number of pixel planes traversed using: a) only the pixel planes to measure the momentum (upper figure); and b) both the pixel planes and the downstream tracker to measure the momentum (lower figure).

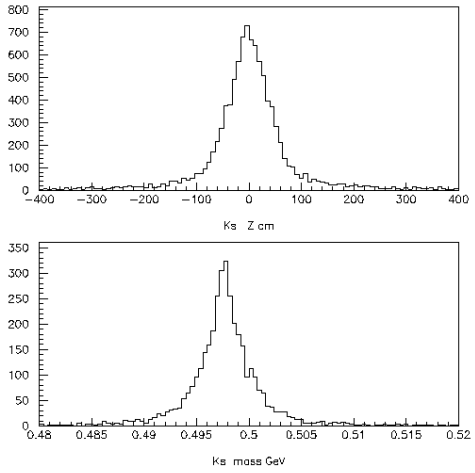

Figure 23: a) Z distribution of decay vertices of K_s^o's in the spectrometer; and b) K_s^o mass peak obtained with tracking system.

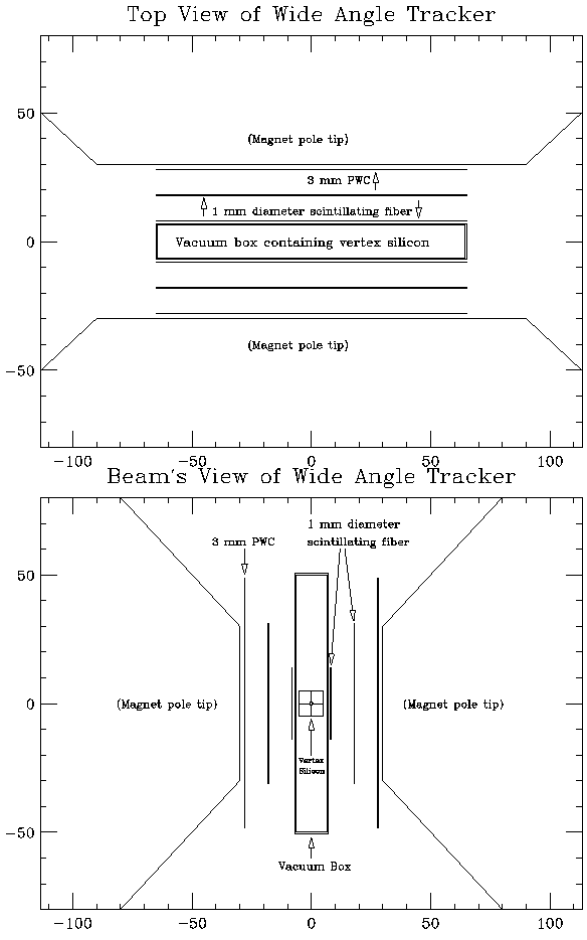

Figure 24: Schematic of the wide angle tracker. Dimensions are in centimeters.

2.4 Triggering System

The proposed broad charm and beauty physics program of BTeV/C0 calls for a trigger whose efficiency

- is large for heavy-quark decay events which can be found off-line and
- is relatively independent of decay mode.

Because the program has many goals and will undergo several phases of development, the trigger needs to be flexible. We plan to implement a multi-level trigger with several "branches" that can be independently prescaled and then combined into a global trigger. These triggers will include muon and dimuon triggers, electron and dielectron triggers, and general interaction triggers. However, the demands of a collider B experiment are difficult to meet with simple, conventional approaches to triggering. In particular, the second criterion above is not satisfied by simple triggers commonly used in hadron collider experiments, e.g. lepton triggers. BTeV's main B-physics trigger focuses on the key difference between heavy quark events and typical hadronic events – the presence of detached vertices – at Level I. It is very efficient for the B decays that can be successfully reconstructed by the spectrometer. It also avoids the need to focus at Level I on specific final states, which can limit the accessible physics. Its implementation requires a very sophisticated trigger architecture which also provides a more than adequate foundation for any of the other triggers we are considering.

In this section, we focus on the Level I detached vertex trigger, for which we are carrying out a program of research and development, based on extensive simulation and design studies. Details some of the other triggers – the muon trigger and the electron trigger – are given in the sections on the muon detector and the electromagnetic calorimeter.

2.4.1 Level I Detached Vertex Trigger

The trigger algorithm has the goal to reconstruct tracks and find vertices in every interaction up to an interaction rate of order 10 MHz (luminosity of $10^{32}\,\mathrm{cm}^{-2}\,\mathrm{s}^{-1}$ at $\sqrt{s} = 2\,\mathrm{TeV}$). This entails an enormous data rate coming from the detector ($\sim 100\,\mathrm{GB/s}$), thus a careful organization of the data-flow is crucial. This trigger must be able to operate both in collider and fixed-target modes. It must be capable of reducing the trigger rate by a factor between a hundred and a thousand.

The key ingredients for such a trigger are

1. a vertex detector with excellent spatial resolution, fast readout, and low occupancy;
2. a heavily pipelined and parallel processing architecture well suited to tracking and vertex finding;

3. inexpensive processing nodes, optimized for specific tasks within the overall architecture;

4. sufficient memory to buffer the event data while the calculations are carried out; and

5. a switching and control network to orchestrate the data movement through the system.

The pixel detector described above is the first ingredient. Use of pixels for the tracker will produce very high spatial resolution for the trigger (and the final analysis) and, because of their 2-dimensional nature and excellent signal-to-noise, will reduce the level of potential confusion during the crucial track-finding phase of the trigger. Since the pixel detector is located in a magnetic field, some momentum information can be derived from the bending in the pixel detector alone without needing to use the downstream tracking system. If, in addition, the pixels have pulse height readout, they can achieve a spatial resolution of less than 9 μm, which provides rather good momentum information to the Level I trigger.

To provide the second ingredient, we employ parallelism both at the subevent level and at the event level. The detector layout described above has "stations" consisting of three planes. Processors organize the hits in each triplet of planes into "station hits". Still at the subevent level, individual processors work on the station hits from a slice of the detector, as will be described below. At the event level, track candidates from the individual slices are brought together in a common processing node, one member of a large farm, for vertex finding.

The third ingredient is provided by using large numbers of inexpensive, commercially available CPU chips. New processors are constantly appearing on the market, often optimized for very specific tasks, and prices are dropping rapidly. Research is in progress to determine the characteristics of the processors needed at each stage.

The fourth ingredient is also commercially available. The time allowed to process the data is limited by the number of events which can be stored while the trigger decision is being made. An event is expected to be significantly less than 100,000 bytes. The memory required to buffer 256 crossings even for 100,000 byte events is only 25 MB and is adequate for a decision time of 33 μs. This system can be off the detector (i.e. not in a strong radiation environment) so commercial (PC) memories are adequate and the costs are small on the scale of the full trigger system. Memory costs do not limit the decision time which could be much longer if necessary.

The final ingredient is switching networks which appear at the input of each section of the Level I trigger and between the Level I trigger and next level of triggering. The design of this switching hardware is under study.

The detailed reference trigger scheme we now discuss was developed by the Penn Group - Selove, Sterner, and Isik [1]. While it may undergo some revisions, it has been an excellent starting point for studying this kind of trigger and the initial results for this particular algorithm are very encouraging.

The proposed algorithm has four steps:

1. In the first step, hits from each pixel plane are assigned to detector subunits. This can be done very rapidly for all planes in parallel using field-programmable gate arrays (FPGAs). It is desirable to subdivide the area of the detectors in a way which minimizes the number of tracks crossing from one subunit into the next and assures uniform and low occupancy ($<$ 1 hit/event) in all subunits. We therefore divide each plane into 32 azimuthal sectors ("ϕ-slices"). Simulation shows that at 2 TeV, on average each ϕ-slice contains 0.2 hits per inelastic interaction, approximately independent of the plane's z coordinate.

2. In the second step, "station hits" are formed in each triplet of closely-spaced planes using hits from each ϕ-slice. Since the pixels under consideration have a rectangular shape (e.g. 30 μm by 300 μm), the two outer planes in each station are oriented for best resolution in the bend view, and the inner plane for the non-bend view. There is a "hit processor" (which may be a microprocessor, an FPGA, or a combination of the two) for each ϕ-slice of each station. The hit processor finds triplets of overlapping pixels, and sends to the next stage a single "minivector" consisting of x, y, $\frac{dx}{dz}$ and $\frac{dy}{dz}$. Given the good position resolution of each measurement, a detector station determines a space point accurate to $5-9$ μm in x and y, and y and x slopes to $\frac{dy}{dz} \approx 1$ mr (bend-view) and $\frac{dx}{dz} \approx 10$ mr (non-bend). The use of these minivectors in the track-finding stage substantially reduces combinatorics.

3. In the third step, minivectors in each ϕ-slice from the full set of stations are passed via a sorting switch to a farm of "track processors." The sign of the bend-view slope is used to distinguish forward-going and backward-going minivectors and send them to separate farms. To handle the few percent of tracks crossing segment boundaries, hits near a boundary between two ϕ-slices can be sent to the processors for both slices.

   Each track processor links minivectors into tracks, proceeding along z from station to station. For each pair of minivectors in adjacent stations, the processor averages the y-slopes in the two stations and uses this average slope (which represents the slope of the chord of the magnetically deflected trajectory) to project from the first station into the second. It then checks whether the y-value of the minivector in the downstream station agrees with the projection within an acceptance window. If three or more hits satisfy this requirement, a fast fitting algorithm finds the momentum of the track candidate.

4. In the fourth step, the tracks are passed to a farm of "vertex processors" and used to form vertices. The vertex with $\sum p_z$ closest to zero is designated as the primary vertex. Tracks which have a large impact parameter with respect to this vertex are taken as evidence for heavy quark production in an event. To reduce the effect of multiple scattering on vertex

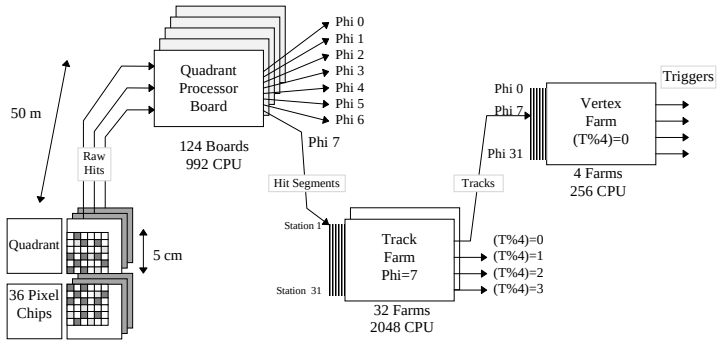

Figure 25: Schematic of Proposed Level I vertex trigger

resolution, tracks below an adjustable bend-view transverse-momentum (p_y) threshold are excluded from the vertex finding.

It is desirable to have pulse-height information included with each hit so that interpolation can be used to improve the point resolution beyond the $30\ \mu\mathrm{m}/\sqrt{12}$ otherwise available. Digital (1 bit) readout seems to be adequate for the p_y cut, but the improved momentum resolution with analog information would allow the processor to calculate the mass of the charged particles at a vertex, which may be a useful variable on which to cut if additional rejection is needed. It also can improve the position accuracy for tracks incident at large angles, which cross over rows or columns of pixels.

The Level I rejection factor for events containing only light quarks is required to be between 10^{-2} and 10^{-3} in order to reduce the data rate into Level II to sufficiently low levels. The overall acceptance for $B \to \pi^+\pi^-$ events is expected to be 10-20% for the proposed BTeV Level I vertex trigger. The expected trigger efficiency for $B \to \pi^+\pi^-$ events that will have both B daughter πs reconstructed should be much higher. Results of simulation studies with this trigger will be described below in Section 4.

This algorithm is preliminary and has not yet been optimized. The current simulation does not take into account Molière multiple-scattering tails, the effect of pair-conversions or hadronic interactions in the silicon, detector inefficiencies, or noise in the detector. We have not yet studied the trigger performance when there is more than one interaction per crossing.

D. Husby and W. Selove have developed a detailed proposal for this trigger system. In this design there are 992 hit processors, 2048 track processors, and 128 vertex processors. Since the architecture is scalable, there is flexibility for these numbers to be optimized to meet unanticipated conditions. The design uses a combination of FPGAs and commercial CPUs. Fig. 25 shows a schematic diagram of the full system. Details of their current design can be found in Ref. [2]. A hardware design has been worked out for a small-scale prototype; see the trigger research and development section in Section 5 for details.

2.4.2 Development of other Level I triggers and the global trigger framework

While we have emphasized the "vertex/impact parameter" trigger because it is our most crucial and most ambitious trigger, we will also have other triggers at Level I. These will include muon and electron triggers and perhaps some triggers derived from the same hardware that is used for the vertex trigger but optimized for different physics. At the output of the first level trigger there will be a 'global Level I trigger' subsystem that will allow us to combine the various individual trigger elements into final triggers (for example, an event with only weak evidence for a secondary vertex but with an indication of a high p_T single lepton might be accepted). It will also have the ability to apply a programmable prescale to the various triggers before the are 'or'ed together to form the final trigger. We will probably also include the ability to dynamically change the prescales during the course of the store.

2.4.3 Beyond the Level I Trigger

Modern experiments in High Energy physics implement hierarchical trigger systems and BTeV is no exception. Many details of the full data acquisition system have to be worked out as the design of the detector components and trigger algorithms become more mature. For this EOI it is simply our intention to demonstrate that a suitable system can be constructed for a reasonable cost. At the design luminosity of $5 \times 10^{31}\mathrm{cm}^{-2}\mathrm{s}^{-1}$ and with a total inelastic cross section of $\sigma_{inel} \approx 60$mb the interaction rate at BTeV will be around 3 MHz. Fig. 26 gives the outline of the expected data flow at the nominal design luminosity.

The Level I trigger we plan must be capable of reducing the trigger rate by a factor between a hundred and a thousand. At our current level of understanding, this seems to be achievable even if the only test made is for a detached vertex in vacuum. The event rate is then reduced to $\approx$100 kHz in the worst case during the highest luminosity running. It is still possible to move all this data, amounting to a maximum rate of 10 GB/s, to the Level II trigger.

Events that pass the first trigger level are forwarded to compute nodes to be further analyzed. First, detector component information is used to partially reconstruct the event, e.g. finding tracks in the vertex detector. Algorithms with refined secondary vertex requirements or invariant mass cuts will be implemented at this level. Events remaining after this step are then fully assembled in a switch-based eventbuilder and passed to a processor farm. Alternatively, an algorithm such as associating a mass with each detached vertex can be computed at Level I which would eliminate the need for an intermediate trigger step before the eventbuilder. Since most of the detached-vertex events will be K_s, a requirement that the mass at the vertex be above some threshold (say 1 GeV/c^2) could reduce the rate to less than 10 kHz with almost no bias against charm and beauty events of interest. Even so, it will probably be impractical to write several kHz of events to archival storage.

The final trigger level will combine information from different sub-detectors

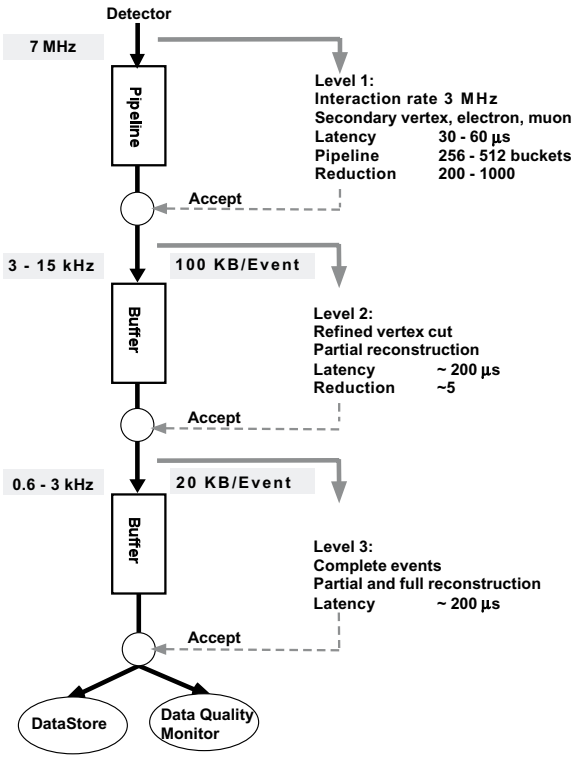

Figure 26: The BTeV data flow diagram. The numbers are for the nominal luminosity of $5 \times 10^{31}\mathrm{cm}^{-2}\mathrm{s}^{-1}$.

to further suppress background events. Particle identification will be available at this stage and could be used to obtain a very clean direct charm signal for specific final states. We intend to fully reconstruct the events at this level before the data are sent to a storage system and made available for off-line processing.

Because the event rate surviving this last level may still be close to a kHz, the software will probably have to reduce the amount of data per event to archival storage by writing out an event summary which eliminates much of the raw data. The event summary would be around 20 KB so that the output rate could still be as high as 20 MB/s. This results in a dataset size of 200 TB/yr, comparable to what is expected from CDF or D0 in Run II. However, initial phases of the experiment will run at much lower rates and will be comparable in dataset size to a current fixed target experiment.

2.4.4 Additional Work

Although initial simulation results are very encouraging, much additional simulation work and a vigorous R&D program are needed to implement such a triggering system. The simulation work will involve studying the performance of

this proposed algorithm under more realistic experimental conditions, which include detector inefficiencies, photon conversions, delta ray production, hadronic interactions in the silicon, low energy loopers, multiple interactions, electronic noise, machine backgrounds, and beam-induced backgrounds (e.g. scraping in the support structures and/or beam pipe). Plans for additional simulation and variations to the Level I and Level II trigger algorithms will be described in Section 5.

2.5 Particle Identification

Excellent charged hadron particle identification is a critical component of a heavy quark experiment. Even for a spectrometer with the excellent mass resolution of BTeV, there are kinematic regions where signals from one final state will overlap those of another final state. For example, $B_d^o \to \pi^+\pi^-$, $B_d^o \to K^+\pi^-$, and $B_s^o \to K^+K^-$ all overlap to some degree leading to ambiguous classification of the final state. These ambiguities can be eliminated almost entirely by an effective particle identifier. In addition, many physics investigations involving neutral B-mesons require 'tagging' of the flavor of the signal particle by examining the properties of the 'away-side' particle. Our studies show that kaon tagging is a very effective means of doing this.

2.5.1 Requirements

In the design of any particle identification system, the dominant consideration is the momentum range over which efficient separation of the various charged hadron types – π, K, and p – must be provided. In BTeV, the physics goal which sets the upper end of the momentum requirement is the desire to cleanly separate $B_d^o \to \pi^+\pi^-$ from $B_d^o \to K^+\pi^-$ and $B_s^o \to K^+K^-$. These two-body decays produce reasonably high momentum pions and kaons. Fig. 27 shows the momentum distribution of pions from the decay $B_d^o \to \pi^+\pi^-$ mentioned above for the case where the two particles are within the spectrometer's acceptance. The low momentum requirement is defined by having high efficiency for 'tagging' kaons from generic B decays. Since these kaons come mainly from daughter D-mesons in multibody final state B-decays, they typically have much lower momentum than the particles in two body decays. Fig. 28 shows the momentum distribution of 'tagging' kaons for the case where the signal particles are within the geometric acceptance of the spectrometer. About 1/5 of the tagging kaons never exit the end of the spectrometer dipole. Almost all of them are below 3 GeV. Almost all kaons exiting the dipole have momenta above 3 GeV. Based on these plots, we have set the momentum range requirement for the particle identification system to be

$$3\,\mathrm{GeV/c} \;<\; P_{particle\ id} \;<\sim 70\,\mathrm{GeV/c} \tag{48}$$

Finally, kaons and pions from directly produced charm decays have momenta which are not very different from the kaons from B-decays. Fig. 29 shows the momentum spectra of kaons from accepted $D^o \to K^-\pi^+$, $D^o \to K^-\pi^+\pi^-\pi^+$, and $D_s^+ \to K^+K^-\pi^+$ in both collider and fixed target mode. The range set by the B-physics requirements is a reasonable, if not optimal, choice also for charm physics.

2.5.2 Initial detector design

Because of the large momentum range and limited longitudinal space available for a particle identification system in the C0 enclosure, there is really only

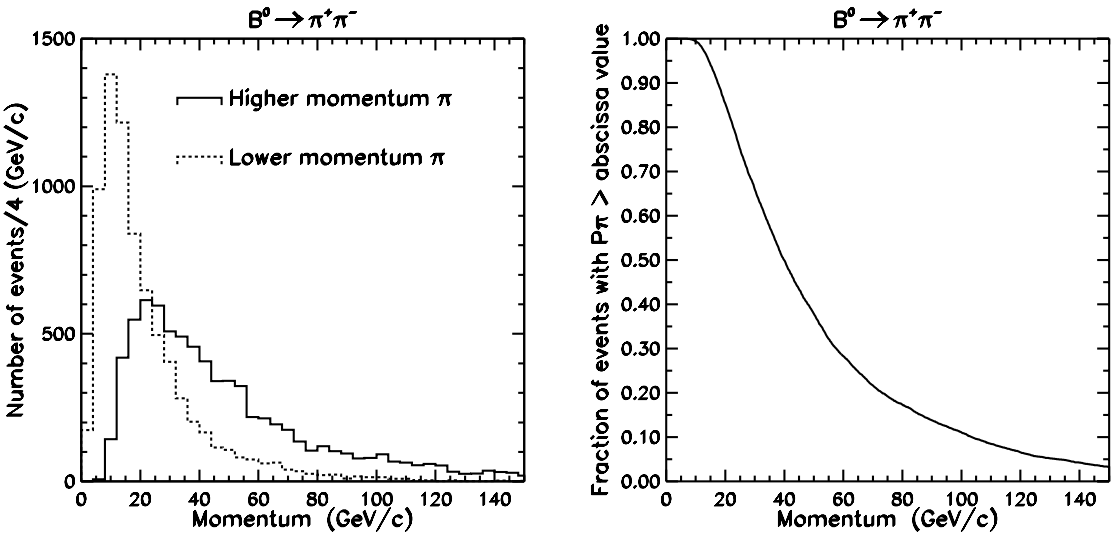

Figure 27: The momentum distribution of pions in $B_d \to \pi^+\pi^-$ decays. The left plot shows distributions for the lower (dashed line) and higher (solid line) momentum pion in this decay. The right plot presents the later distribution in integral form, which gives loss of efficiency as a function of the high momentum cut-off of the particle ID device.

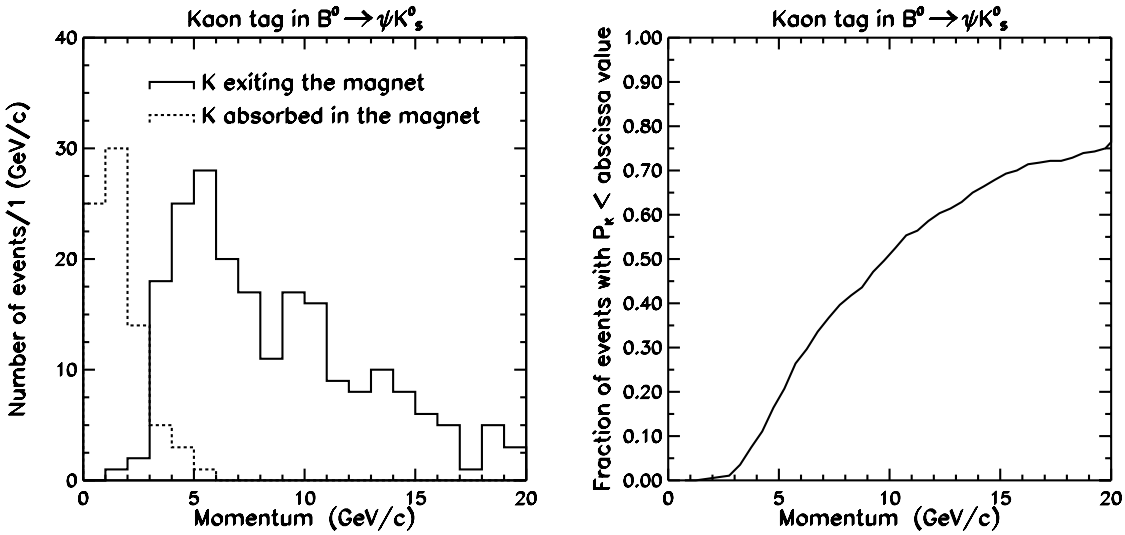

Figure 28: The momentum distribution of 'tagging' kaons for the case where the signal particles (ψK^0_S) are within the geometric acceptance of the spectrometer. The left plot shows distributions for kaons absorbed in (dashed line) and exiting from (solid line) the magnet. The right plot presents the later distribution in integral form, which gives loss of efficiency as a function of the low momentum cut-off of the particle ID device.

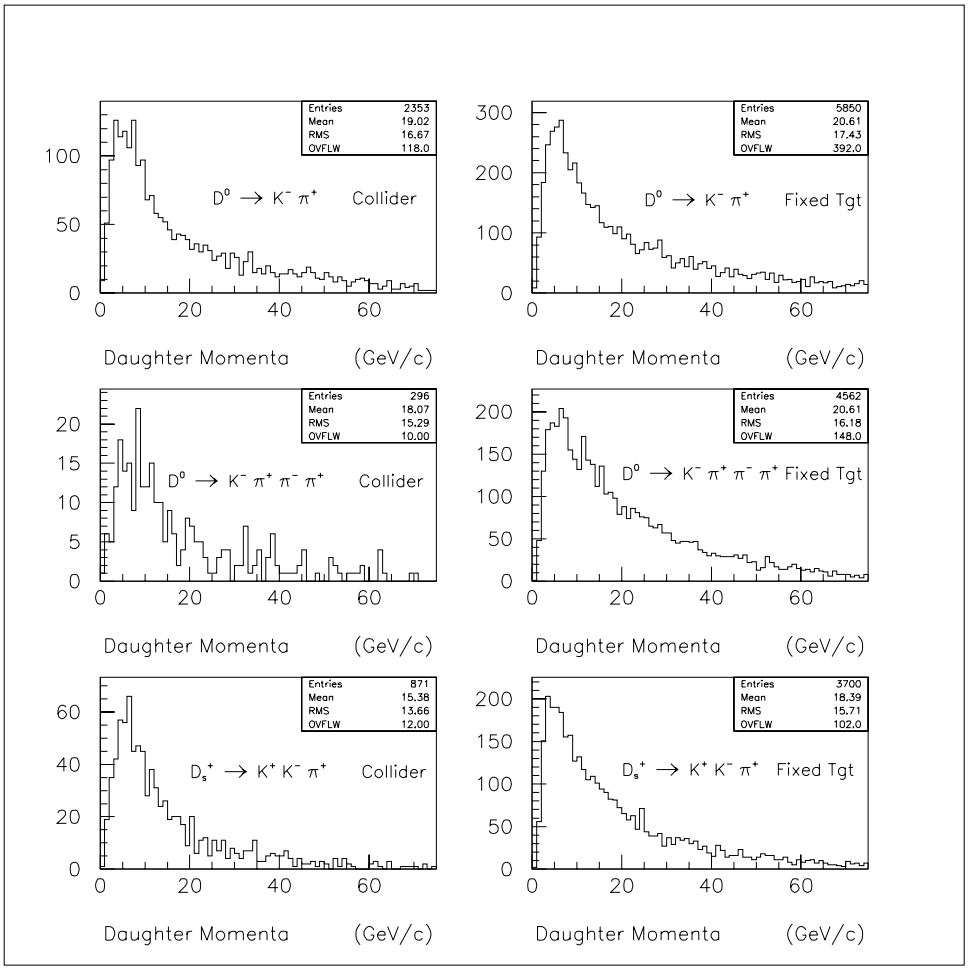

Figure 29: The momentum spectra of kaons from accepted $D^o \to K^-\pi^+$, $D^o \to K^-\pi^+\pi^-\pi^+$, and $D_s^+ \to K^+K^-\pi^+$ in both collider and fixed target modes.

Parameter	C_4F_{10}	C_5F_{12}
(n-1) x 10^6	1510	1750
gamma-threshold	18.2	16.9
$\Theta_c(\beta=1)$	54.9 mr	59.1 mr
π threshold	2.5 GeV/c	2.4 GeV/c
K threshold	9.0 GeV/c	8.4 GeV/c
p threshold	17.1 GeV/c	15.9 GeV/c

Table 9: Several parameters for the two candidate radiators.

one choice of detector technology – a gaseous ring-imaging Cherenkov counter. Fortunately, there are gas radiators which provide signal separation between pions and kaons in this momentum region. Table 9 gives some parameters for two candidate radiator gases: C_4F_{10} and C_5F_{12}. Note that below 9 GeV, these gases do not provide K/p separation and that, since kaons are below threshold, the system operates in a threshold mode (except that it has much better noise discrimination than a normal threshold counter because it still measures a Cherenkov ring for pions). Among other experiments C_5F_{12} was used in the barrel part of the DELPHI RICH. It needs to be operated at 40°C because of its high condensation point. The C_4F_{10} gas can be used at room temperature. It was used in the DELPHI endcap RICH and was adopted for the HERA-B and LHC-B RICH detectors. The simulations described below are based on C_4F_{10}.

There is approximately 3 meters in length between the end of the dipole including the tracking chambers and the EM calorimeter in which to site a RICH detector. To determine transverse dimensions of the RICH detector we have looked at intersections of daughter charged particles from B_d decays, reconstructed in the BTeV charged tracking system, with the entrance plane of the RICH vessel, and at intersections of the radiated Cherenkov photons with the mirrors located at the other end of the vessel. These distributions are shown in Fig. 30. The photodetectors should be located away from the flux of particles exiting the magnet, therefore the mirrors are tilted. In order to minimize geometric aberrations from an off-axis mirror configuration, the mirror would be split along the mid-line of the detector, reflecting photons to photodetectors located on each side of the vessel in the non-bend view. The lateral extent of the mirrors (both horizontal and vertical) should be around 6 meters. To estimate the size of the area to be covered by photodetectors we also show in Fig. 30 the spatial distribution of Cherenkov photons at one of the two photodetector planes.

Tentative sizes of the proposed RICH detector are shown in Table 10 and illustrated in Fig. 31. A possible configuration for the mirrors is to make them from an array of individual hexagons as shown in Fig. 32. Each mirror half would consist of 18 full hexagons (76.2 cm tip-to-tip)and 6 half hexagons.

Fig. 33 shows the expected ring radii at the photodetector and the sepa-

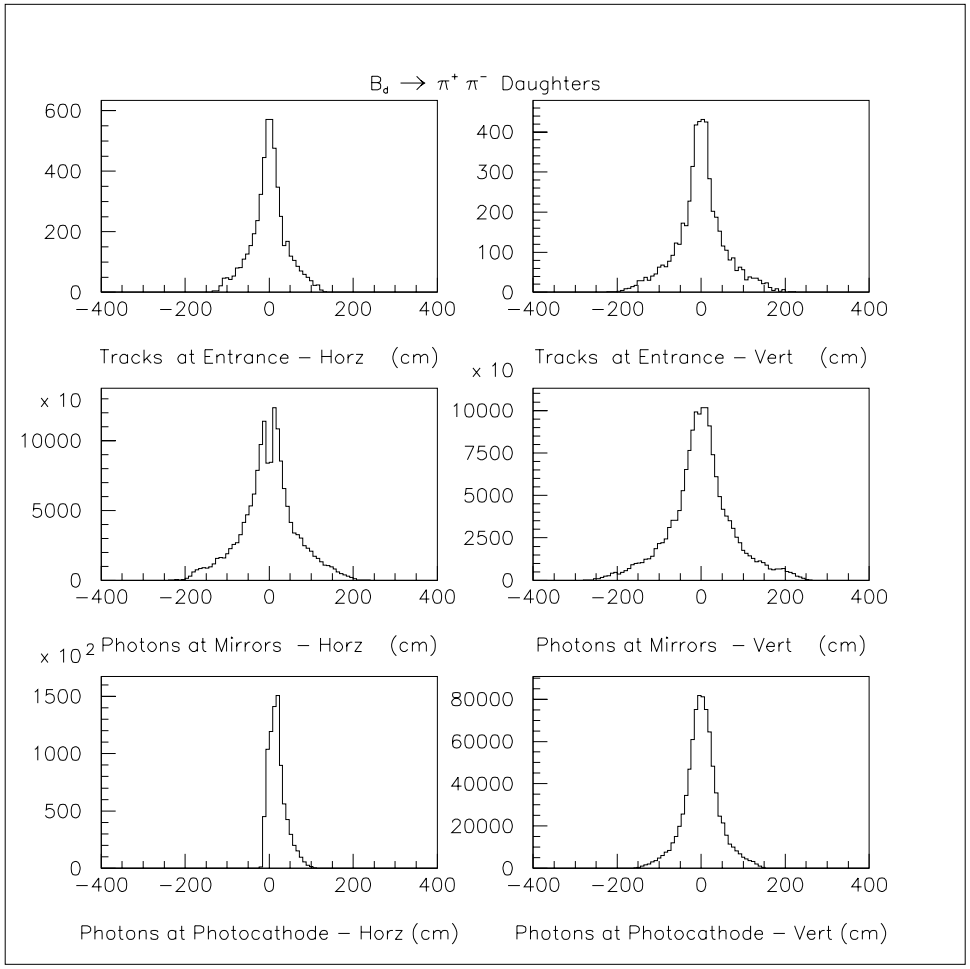

Figure 30: The spatial distribution of daughter charged particles from B_d decays at the upstream end of the particle identifier (top row), the spatial distributions of their radiated photons at the downstream end of the RICH (middle row), and at one of the photodetector planes (bottom row). The plots on the left (right) show horizontal (vertical) coordinates. These distributions are used to set transverse dimensions of the RICH radiator and of the photodetection planes.

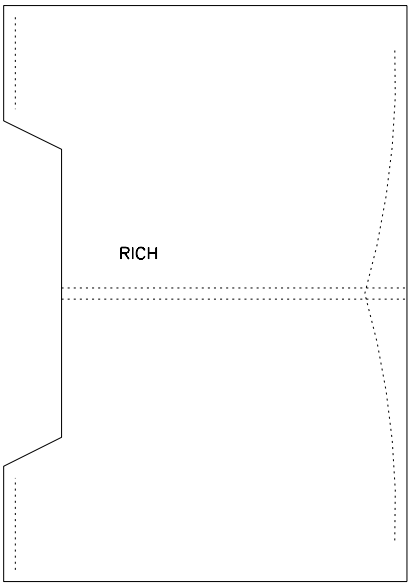

Figure 31: Schematic of the RICH detector.

Characteristic	Size
Radiator Length	3 m
Radiator Cross Section	4.2 m x 4.2 m
Entrance Window	1.3 m x 2.0 m
Mirror Radius	6 m
Photodetector Size(x2)	1.0 m x 2.2 m

Table 10: Spatial dimensions of the proposed RICH detector.

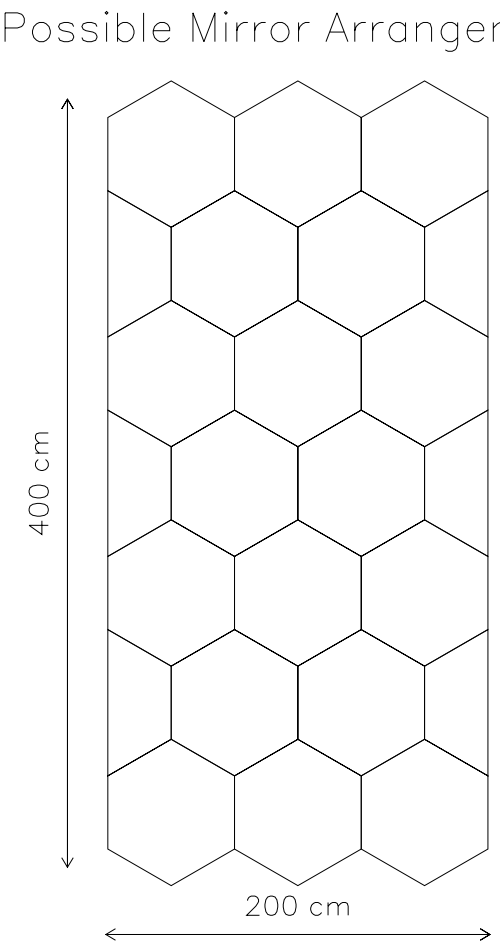

Figure 32: Possible arrangement for each half of the mirror using hexagonal mirrors of size 76.2 cm tip-to-tip.

ration between different ring radii for various particle types as a function of momentum for the C_4F_{10} radiator and a 600 cm radius mirror. We would like to achieve meaningful π/K separation out to about 70 GeV/c, where the ring radius difference is 1.3 mm or 0.43 milliradians (mr). For 3 sigma separation we would need to achieve a resolution of 0.4mm or 0.14 mr. The LHC-B design [3] based on a 1m long C_4F_{10} radiator with HPD readout claims a resolution of 0.13 mr per track which would satisfy our goal. The LHC-B detector has smaller transverse size resulting in a smaller mirror tilt. Loss of resolution due to the larger mirror tilt in our detector can be compensated to some extent by a larger number of photoelectrons produced in a longer radiator. Detailed RICH design studies are under way. An alternative choice to HPD's for the photodetector could be multi-anode PMTs such as the 16 channel tubes from Hamamatsu used in the HERA-B detector. We would need approximately 2500 such PMTs (40000 channels). All readout schemes we are considering operate in visible light, possibly extending to the ultraviolet.

2.5.3 Aerogel Radiator

In order to increase positive identification of low momentum particles, one interesting possibility is to insert a thin ($\sim$ 5 cm) piece of aerogel at the entrance to the gas RICH as proposed by LHC-B. [3] For example, aerogel with refractive index of $n = 1.03$ would lower the π, K, p momentum thresholds to 0.6, 2.0, 3.8 GeV/c respectively. Shorter wavelength Cherenkov photons undergo Raleigh scattering inside the aerogel itself. They are absorbed in the radiator or exit at random angles. A thin mylar or glass window between the aerogel and the gas radiator would pass photons only in the visible range, eliminating the scattered component. The same photodetection system could then detect Cherenkov rings produced in both the gaseous and the aerogel radiators. The radius of rings produced in the aerogel would be about 4.5 times larger than those produced in C_4F_{10}. The aerogel radiator would provide positive π/K separation up to 10-20 GeV/c. It would also close the lower momentum gap in K/p separation. Since the low momentum coverage would be provided by aerogel, one could think about boosting the high momentum reach of the gas radiator by switching to a lighter gas such as C_2F_6 ($n = 1.0008$) or CF_4 ($n = 1.0005$). This would also loosen the requirements for Cherenkov angle resolution needed to reach a good K/π separation at a momentum of 70 GeV/c. Detailed simulations are needed to evaluate trade-offs due to more complicated pattern recognition.

The alternative options to be considered for improving particle identification at lower momenta include a ToF system or a DIRC.

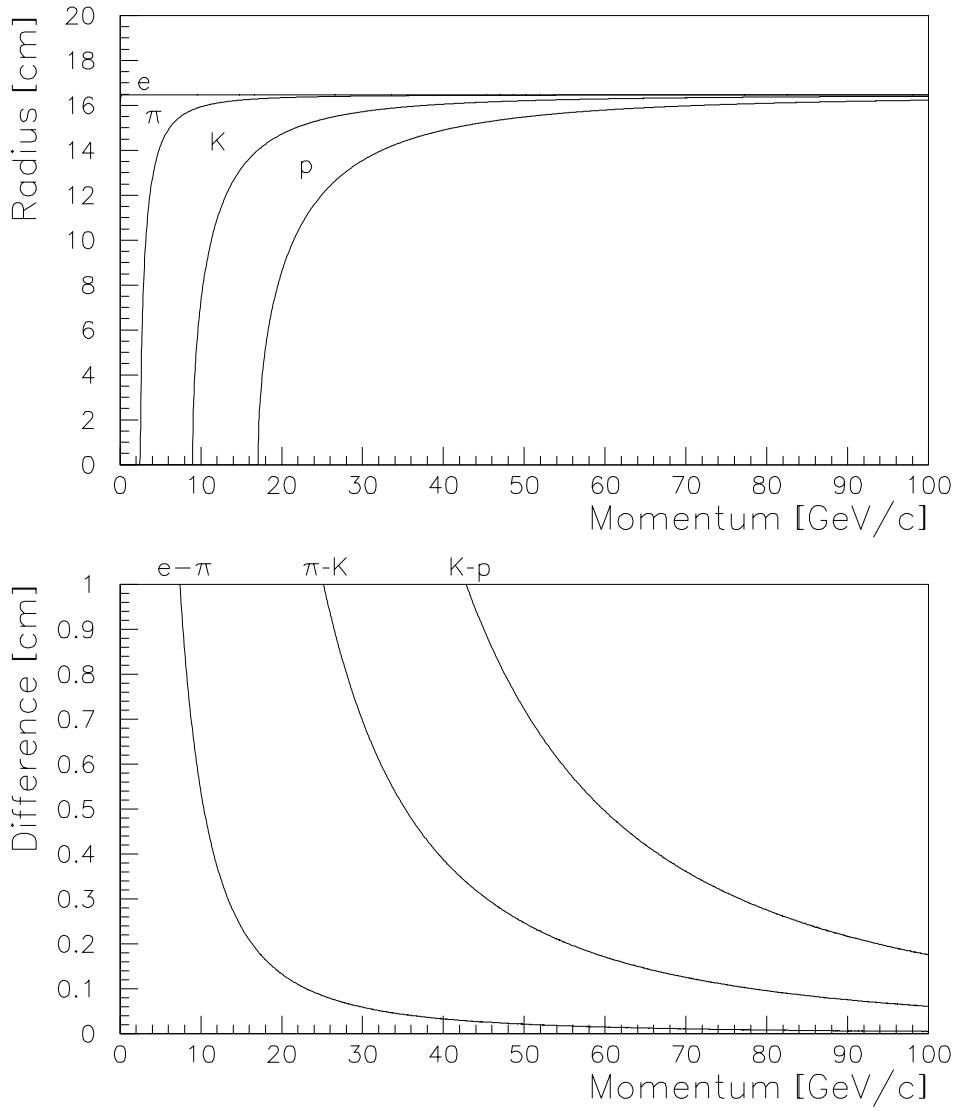

Figure 33: Ring radius and difference in ring radius for several different particle types at the photodetector for the C_4F_{10} radiator and a 600 cm radius mirror.

2.6 Electromagnetic Calorimetry

The ability to identify electromagnetic final states is an integral part of the BTeV physics program. First, electrons can be used to tag the flavor of the associated B for CP studies. Second, high mass electron-positron pairs can be used to tag exclusive final states (eg J/ψ). Further, an ambitious program would reconstruct exclusive final states containing neutral mesons (π^0's, η's, ρ's, etc.) Lastly there is the hope of measuring final states containing single photons.

Furthermore, the electromagnetic calorimeter can aid in the triggering provided that it can efficiently identify electrons while rejecting the large background due to photon conversions and misidentified hadrons.

To determine the appropriate size, segmentation, and technology for the calorimeter requires an understanding of the radiation environment of the calorimeter as well as the signals and the backgrounds. The area available to the calorimeter is located 7 meters from the nominal interaction point and extends for 1 meter. The transverse dimension which matches the acceptance of the spectrometer is a 4 x 4 meter box centered on the Tevatron beam line (see Fig. 16).

2.6.1 Signals

We have begun Monte Carlo studies of the following benchmark processes to understand the signals we hope to measure.

1. $B \to D^{(*)} e\nu$
   e.g. electron tagging,
2. $B \to J/\psi K_s$, $J/\psi \to e^+e^-$, $K_s \to \pi^+\pi^-$
   e.g. identification of exclusive final states (triggering),
3. $B^\pm \to \pi^\pm \pi^0$
   e.g. CKM measurement if one is able to make a good mass measurement on neutral final states,
4. $B \to K^*\gamma$
   e.g. Radiative decays if one is able to limit the large background due to neutral pion decays.

As a preliminary study the above physics processes were generated using PYTHIA and tracked though the BTEV/C0 geometry using the MCFAST Monte Carlo. All charged particles in the final state were required to be reconstructed in the spectrometer. The positions and energies of the electrons and photons at the location of the calorimeter were then examined. In the case of modes with more than one electromagnetic particle, the minimum energy and the maximum radius were used. The radii for acceptances of 80% and 95% are summarized in Table 11. The minimum energy for acceptances (independent of the transverse size) are also listed in Table 11. Note that these studies are preliminary and the statistics are low. Also care must be taken to understand the correlation between energy and radial position (see Fig. 34).

Process	radius		Minimum energy	
	95%	80%	95%	80%
$B \to D^{(*)} e\nu$	200 cm	170 cm	3 GeV	6 GeV
$B \to J/\psi K_s$	210 cm	170 cm	5 GeV	8 GeV
$B^{\pm} \to \pi^{\pm}\pi^0$	210 cm	170 cm	$\leq$ 1 GeV	3 GeV
$B \to K^*\gamma$	200 cm	160 cm	2 GeV	4 GeV

Table 11: Required geometry and sensitivity for 80% and 95% efficiency

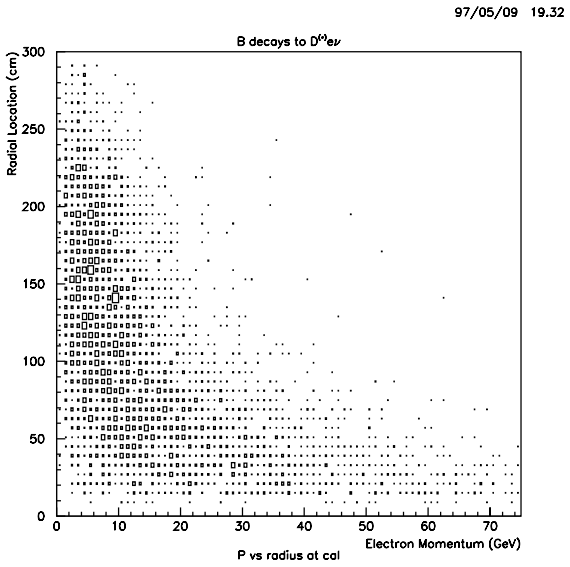

Figure 34: Example of Energy and Position correlation for semi-leptonic B decays

2.6.2 Backgrounds

The dominant background which affects the identification of electrons is expected to be photon conversions due both to interactions in the beam pipe and in the silicon near the primary vertex. Other backgrounds will be misidentified pions which charge exchange in the first few depths of the calorimeter, and other processes which can mimic the behavior of an electron.

The dominant background to single photon identification is neutral pions where the less energetic of the two photons is below the sensitivity of the calorimeter. If the segmentation of the calorimeter is not fine enough, then there can also be background due to the two photons not being resolved.

The ability to reject backgrounds will depend on the choice of the calorimeter technology, the segmentation, and to some extent the performance of the other

detector elements. These processes will have to be evaluated both with Monte Carlo tools (such as GEANT and MCFAST) and test beam studies. However calorimeters and calorimeter technology are well understood.

- Electron identification
  Electrons will be identified by matching their energy and momentum and looking at their transverse (and perhaps) longitudinal profiles. There are no worries that any of the technologies listed above would fail provided that the segmentation of the calorimeter is adequate (cell size equal to a Molière radius).

- Electron-Positron mass resolution
  Limited segmentation (larger than 5 x 5 cm^2) would degrade the mass resolution of the calorimeter.

- π^0 identification
  The mass resolution of the final state will be proportional to the energy resolution of the Electromagnetic calorimeter. From Table 11, 80% of the photons have an energy greater than 4 GeV. To obtain a π^0 mass resolution of 5-6 MeV implies a resolution of better than $20\%/\sqrt{E}$.

- Single photon identification
  Single photon identification depends on the sensitivity of the calorimeter. The background rate is given by the number of π^0s produced convoluted with the efficiency of π^0 rejection based on the sensitivity. The efficiency of the rejection can be estimated by assuming that

$$\text{efficiency of rejection} = 1 - \frac{2E_{\text{min}}}{E_{\pi^0}}$$

  where E_{min} is the minimum energy to which the calorimeter is sensitive (see Fig. 35). Since the background is at least 3 orders of magnitude larger than the signal, sensitivities of better than 5 MeV are required if one wishes to pursue this physics.

2.6.3 Technology Choices

The following technologies are under consideration (from the point of view of performance, cost, and availability).

- A sampling calorimeter with Lead and either Scintillator or liquid Argon
- A total ionizing calorimeter based on either CsI or liquid Krypton

Lead glass has been neglected because it is not likely to survive the yearly radiation dose as measured by CDF:

$$\text{Dose} = \frac{0.4\text{MRad}}{(\text{r}/2.5\text{cm})^{1.7}}$$

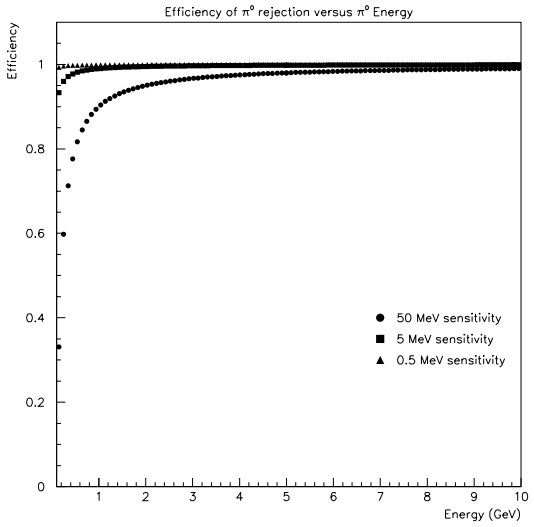

Figure 35: π^0 rejection efficiency for different sensitivity

where r is the radial distance from the beam (see Fig. 36).

Table 12 lists the typical characteristics of various materials used to construct electromagnetic calorimeters. In all cases the cell size would have to be on the order of 2 x 2 cm^2. These characteristics lead to the following performance characteristics:

- Lead Scintillator
  For most currently operating EM lead-scintillator callorimeters, the resolution is typically $12 - 15\%/\sqrt{E}$, which is defined by a sampling ratio (with thinner absorber and thicker active media one would have better resolution), and a constant term of 1-2%. The constant term is induced from a number of internal non-uniformities, such as variation of thickness of scintillating layers (which in its turn contributes to gain variation) and radiation damage, and can be controlled to some extent with calibration. However, the disadvantage is that it could suffer radiation damage after 100 kRad.

- Lead-Liquid Argon
  The resolution ranges between $7 - 10\%/\sqrt{E}$ with a constant term of 1-2% which is induced from a number of internal non-uniformities. The advantage is that, in principle, there is no risk of radiation damage.

- Liquid Krypton
  The difference between the use of Krypton and Argon is that Krypton

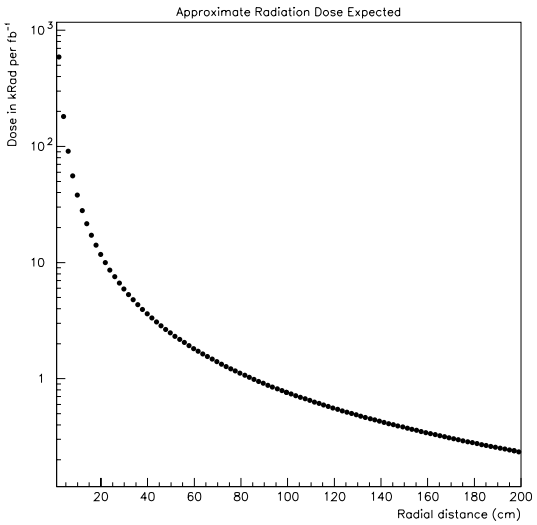

Figure 36: Expected radiation dose at the Tevatron for 1 year of running

Material	Radiation Length (X_0)	Depth ($20X_0$)	Interaction Length (Λ_0)
Argon	14.0 cm	280 cm	83.7 cm
Krypton	3.9 cm	78 cm	65.4 cm
CsI	1.85 cm	37 cm	36.5 cm
Pb	0.56 cm	40 cm	17.1 cm

Table 12: Properties of commonly used calorimeter materials

requires no lead. This improves the resolution to $3\%/\sqrt{E}$ and in principle reduces the constant term to better than 0.5%.

- Cesium Iodide
  Cesium Iodide crystals give a superior resolution but require a large effort to attain the resolution. Also there is the possibility of radiation damage to crystals near the beam pipe (The KTeV collaboration has shown that there are no detrimental effects for doses as high as 20 kRads).

If the only goal is good electron identification then a sampling calorimeter of either Lead-liquid Argon or Lead-Scintillator would suffice. However, the possibility of a large radiation dose near the beam at C0 suggests a preference for a liquid based technology. The E706 calorimeter is available, but it is not clear if the structure is adaptable to our needs.

If the goal is to be able to identify final states containing π^0s and possibly single photons, then the choice is between CsI and liquid Krypton. Again the

issue of radiation damage near the beam leads one to prefer a liquid based technology.

2.7 Muon Detection

The BTeV/C0 muon system has two primary functions:

- J/ψ and Prompt Muon Trigger: Besides providing interesting physics, this trigger performs an important service role by selecting (bottom) events on which the more aggressive and technically challenging triggers (such as the vertex trigger) can be debugged and evaluated.

- Muon Identification: Many of the experiment's physics goals (rare decay searches, CP violation studies which require tagging, studies of beauty mixing, searches for charm mixing, etc.) rely on efficient muon identification with excellent background rejection.

A big challenge in designing a system that serves the above purposes is understanding and rejecting the backgrounds from the accelerator, interaction point, and hadronic showers in the EM calorimeter. The size constraints imposed by the experimental hall add significantly to the difficulty.

At the current time, the requirements of the J/ψ trigger are driving the design. This function requires that the system have a momentum and/or di-track mass trigger capability. Both a magnetic (toroidal) option and a non-magnetic option have been investigated [4]. In the magnetic option, the tracking elements of the muon system itself combined with the muon toroid permit momentum/mass triggering capability using only the muon detector. In addition, this option provides the ability to compare the stand-alone measurement with the measurement from the upstream spectrometer to achieve improved background rejection. However, the magnetic option requires finer tracking resolution which increases the cost. This increased cost needs to be quantified and the trade-offs must be well understood so that a final choice can be made. The magnetic (toroidal) system is the current BTeV/C0 baseline system.

2.7.1 Physics Requirements

Fig. 37 shows the momentum and spatial distributions of muons from $B^o \rightarrow \psi K_s$ where $\psi \rightarrow \mu^+\mu^-$. Fig. 38 shows the same distributions for $B^o, B^+, B_s^o \rightarrow \mu + X$, a typical distribution for away side tags.

In order to be successful as a trigger, the system must get a rejection at Level I of at least 10^{-3} in the full BTeV configuration and at least 10^{-2} in the lower luminosity initial BTeV/C0 situation. The rate after the final level of trigger must be around 100 Hz. The sets the rejection at 1×10^{-4} of all events for BTeV/C0 and 1×10^{-5} for BTeV. The goal for muon misidentification is 10^{-3}.

2.7.2 Design Considerations

Our preliminary calculations show that it is not possible to get a good momentum measurement using a non-magnetic muon system and the dispersion provided by the central dipole. The extrapolation distance is too large given

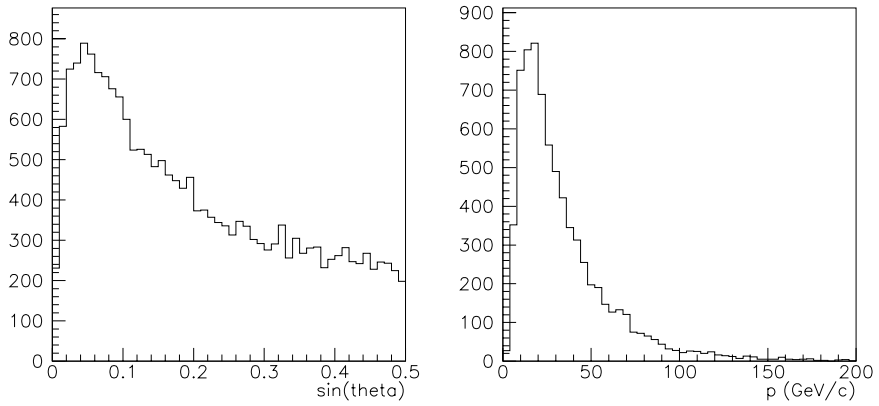

Figure 37: Distribution of (a) production angle and (b) momentum (for accepted muons) for muons from $B^o \to \psi K_s$ where $\psi \to \mu^+ \mu^-$.

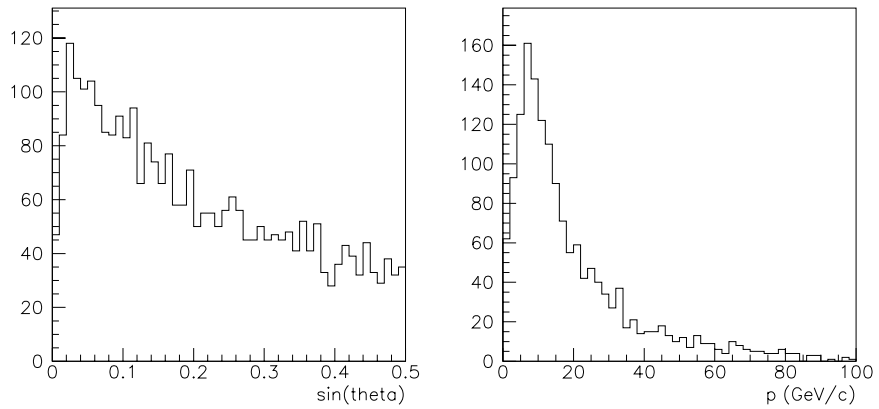

Figure 38: Distribution of (a) production angle and (b) momentum (for accepted muons) for muons from $B^o, B^+, B_s^o \to \mu + X$.

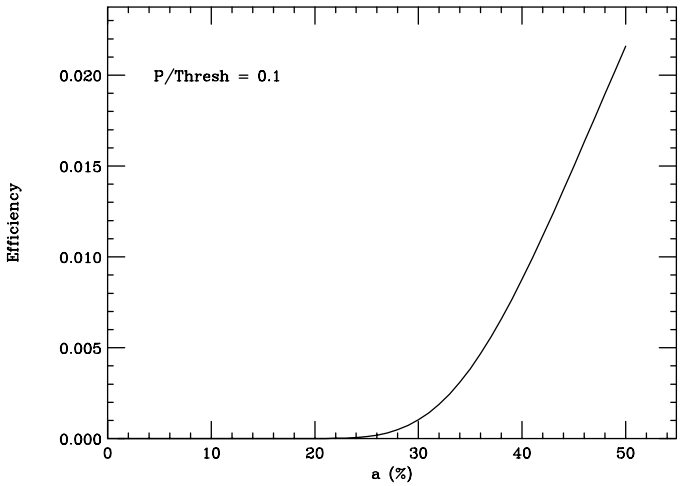

Figure 39: The efficiency calculated for a 1 GeV muon to pass a 10 GeV threshold as a function of a, the mcs term in the resolution formula. Note the extreme sensitivity in this efficiency near $a = 25\%$.

the level of multiple scattering up to the muon planes, making it unfeasible to point the muon track segment back to the interaction region. A magnetic toroid is the only option which will allow us to trigger effectively on muon momentum using information from the muon system alone.

The fractional momentum resolution of a simple toroidal system can be parameterized by the expression:

$$\frac{\sigma_p}{p} = \sqrt{a^2 + (b\ p)^2} \tag{49}$$

At low momentum, where the multiple scattering dominates resolution, a 1.5 Tesla, 1 meter thick toroid with magnetic fields circulating in the $\hat{\phi}$ direction provides an intrinsic fractional momentum resolution of $a = 25\%$. This means that a trigger essentially rejects very soft muons at roughly the 4σ level. Fig.39 shows that the potential rejection provided by a trigger for low momentum muons significantly degrades once the low momentum fractional resolution exceeds 25% (meaning a minimum of 1 m of magnetized iron is required).

At higher momentum, where multiple scattering is less important, one becomes sensitive to the b term of Eqn. 49. The b term depends on the specific layout geometry and spatial resolution of the detector system. The high momentum resolution influences how sharp a momentum threshold one can make in a stand-alone muon trigger. Fig. 40 illustrates this point by showing the trigger efficiency as a function of momentum for several b values.

As a further illustration, Fig.41 shows the resolution obtainable at the trigger level for $J/\psi \rightarrow \mu^+\mu^-$ events for two values of b.

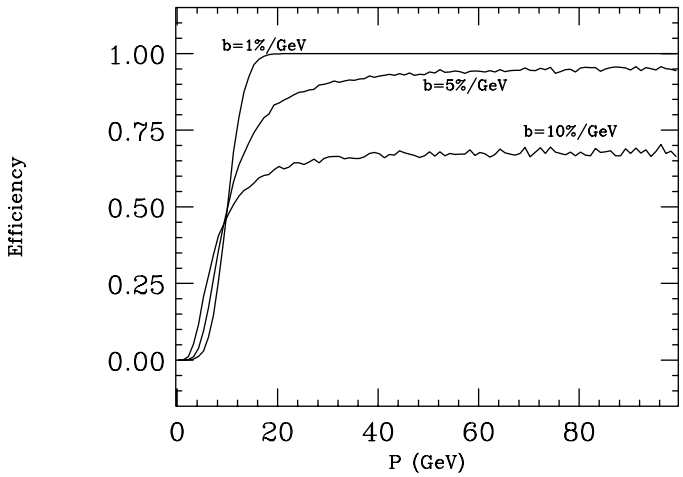

Figure 40: Simulated trigger efficiency as a function of muon momentum for a trigger designed to fire with a 50% efficiency at 10 GeV. The mcs dominated term is set to $a = 25\%$ while the measurement dominated term varies from $1\%/GeV < b < 10\%/GeV$. The $2 \oplus 2$ option read out by four $\sigma = 2.5\ mm$ muon detectors gives $b = 1\ \%/GeV$.

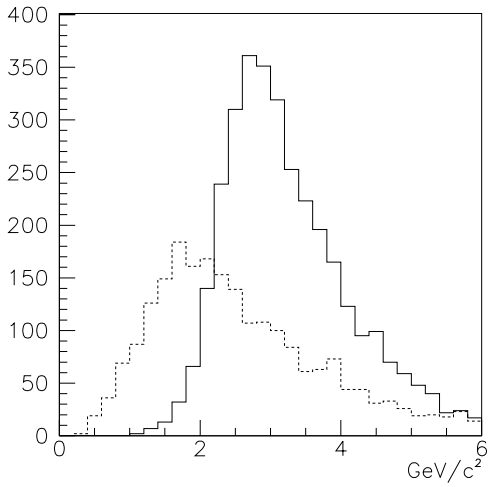

Figure 41: Reconstructed $J/\psi \rightarrow \mu^+\mu^-$ mass resolution for $b = 1\%/GeV$ (solid) and $b = 5\%/GeV$ (dashed), where b is defined in Eqn. 49. Equal numbers of J/ψ candidates were generated for each case.

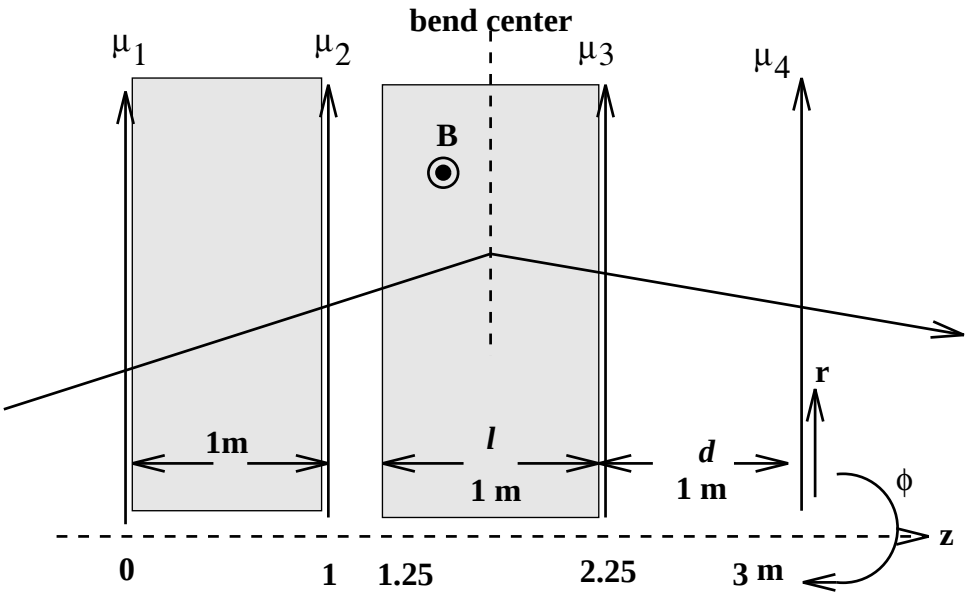

Figure 42: Layout of one arm of the muon detector.

Several possible measurement and shielding layouts are being studied. We believe that it is very likely that timing considerations alone dictate that the muon detector have an intrinsic rms spatial resolution comparable to our needs at the trigger level. Timing information is useful for rejecting background hits such as those associated with accelerator backgrounds (these hits come 70–80 ns before tracks from the interaction point). Assuming a fast gas drift velocity of 10 cm/μs, a drift tube system with a maximum drift time of 50 ns has a maximum drift length of 5 mm. Good momentum resolution ($b \approx 1\%/GeV$) can be achieved with $\sigma = 2.5$ mm spatial resolution, if both the trajectory of the muon entering and exiting the toroid are measured by upstream and downstream θ doublets with one meter lever arms as illustrated in Fig.42. We will call this arrangement a $2 \oplus 2$ measurement.

In the $2 \oplus 2$ layout of Fig.42, only the downstream steel is magnetized – the upstream steel is for shielding only. This arrangement where entering and exiting angles are measured by field free doublets is being studied since this simple bend angle measurement might be easier to implement in a fast trigger. We are also studying the possibility of magnetizing both steel elements. This would offer better resolution – both a and b will decrease by about 30% – and might provide additional filtering of soft hadronic debris which would tend to "curl" up in the presence of the magnetic field.

The most upstream of the four stations might be inadequately shielded against hadronic showers originating in the electromagnetic calorimeter. One could measure momentum using the downstream doublet and a single upstream point which we will call a $1 \oplus 2$ measurement. For the same spatial resolution,

the b parameter obtainable using the $1 \oplus 2$ measurement is 2.8 times worse than that for the $2 \oplus 2$ measurement. Our studies show that the resolution loss due to a missing or confused upstream plane can be largely recovered by tracing the upstream trajectory through the dipole field to the interaction region.

2.7.3 Detector Design and Layout

The detector technology selected must have the following attributes:

1. Robust: It will be very difficult to access the detectors once they are installed.

2. Low Cost: There is a large area to cover (4.8m $\times$ 4.8m) and there will be as many as four stations of chambers in each arm. The cost of readout electronics must be kept low, especially in the proposed magnetic system where the channel count will be relatively high.

3. High Rate Capability: Rates of a few kHz/cm^2 are possible in parts of the system (based on calculations of accelerator backgrounds).

4. Time Resolution: Timing information on hits with a resolution of 30–40 ns will allow rejection of hits due to accelerator backgrounds.

5. Spatial Resolution: For a magnetic system, tracking resolutions on the order of 2–3 mm are required.

6. Longitudinal Compactness: Given the size constraints, the detectors should be of minimal thickness.

7. Minimal Neutron Susceptibility: We will avoid use of hydrogenic detector elements.

The above criteria appear to rule out some candidate technologies. The expected occupancy means that resistive plate chambers (RPC's) will be inadequate without pre-amplifiers, which increases the per channel readout cost of that technology. The drift tubes proposed for use in the SDC muon system are too thick.

Two technologies are currently being given serious consideration: cathode strip detectors such as those being proposed for use at LHC and extruded tubes of the type that have been used in several Fermilab experiments.

Work on cathode strip detectors is being done by an LHC group in Lab 7, so there is significant local expertise. This technology seems to meet all of the above specifications (although we were told that they have not yet done beam tests to verify item (3)).

These chambers consist of gas gaps (roughly 1 cm thick, although a range of thicknesses is possible) with anode wires spaced at roughly 3 mm. The cathodes are divided into strips and are read out. Charge sharing is used to increase measurement resolution. It is claimed that the resolution of these chambers, for 16 mm wide strips, is less than 1 mm. The resolution depends on the thickness

of the gas gap and the location of the charge centroid (the resolution is worse near the center of a strip). The anode wires can also be read out. In the LHC design, 16 wires are ganged and readout by one TDC (the timing is used to associate hits with individual beam crossings, which are much more frequent than the 132 ns expected at BTeV/C0). Several layers of gaps are stacked together to provide local track vectors and redundancy. The gas they use is 20% CF_4, 50% CO_2, and 30% Argon. Since this gas contains no hydrogen, it should be less susceptible to neutron backgrounds. The mechanical details of the Lab 7 chambers are given in a CMS Note [5]. The 12' by 5' size is the largest size chamber the group can build, since they require that a chamber be built from whole pieces of copper clad G-10. (Presses are not available to make larger sheets.) One potential difficulty with this technology is the charge sharing required to obtain 1 mm resolution. It is not clear that this sharing calculation can be completed in time for use in the trigger.

Extruded tubes have been used as muon detectors in several experiments at Fermilab. Each extrusion consists of several square tubes arranged in two overlapping layers. A fast gas would be used to obtain the requisite timing resolution. Due to the overlap of the two layers of tubes, the spatial resolution in latch mode approaches $w/(2\sqrt{12})$, where w is the width of a tube.

Our current straw man design, as illustrated in Fig. 42 and Fig. 43, consists of four stations 8' in radius. Each station is divided into sectors: 8 for the extruded tube design and 10 for the cathode strip design (where the width of a sector is limited to 5'). To give full coverage with no dead regions, adjacent sectors would be overlapped. The requirements for the muon system and the parameters of the current baseline design are summarized in Table 13. In Fig. 43 and Table 13 we have assumed the extruded tube design. This reflects our current (weak) prejudice.

If the extruded tube technology is chosen, in principle a sector design is not necessary, as the tubes could be long enough to cover the full width or height of each station. Dividing each plane into sectors, however, has significant advantages:

1. It simplifies trigger logic.

2. It reduces "ghost hits" (pattern recognition confusion) at both the trigger and off-line stage.

3. It makes it possible to split a station so that it can be moved out of the beamline, providing access for repairs.

For the cathode strip technology, each sector would be 8' along the long side and 5' wide across the top. In this design the strips would run in the $\hat{\phi}$ direction and measure $\hat{r}$, which is the coordinate which requires the fine resolution. The wires would run in the $\hat{r}$ direction. To maintain the stability of the wires over distances of 8' requires some sort of support at roughly 1 m spacing. Ten sectors would be required for one station. To be conservative, this design uses three gaps (we don't require vector segments, but some redundancy seems prudent).

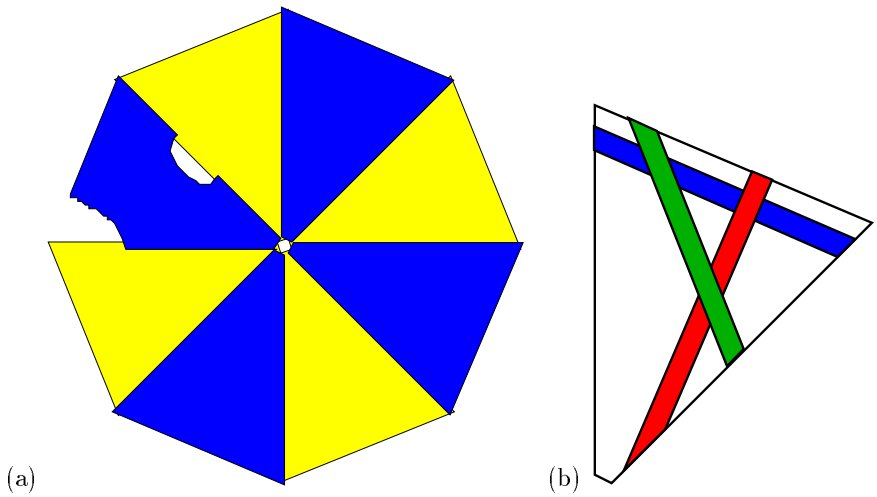

Figure 43: Sketch of one station: (a) full plane with cutaways in one octant to show overlaps, (b) one octant with readout orientations shown for the three views.

To calculate the channel count of this system, we assume the strip width is 16 mm, which gives about 450 channels per sector (150 per layer of each sector $\times$ 3 layers) or 18000 channels for the full system. To read out the anode wires requires 90 more channels per sector (3mm wire spacing, but wires are ganged in groups of 16) for a total of 3600 anode channels in the system. Each sector would be 6cm thick. A full measuring station consisting of overlapping sectors would be a total of 12 cm thick.

A sector in the extruded tube technology option (see figure 43) would consist of three views: $\hat{r}$, $\hat{\phi}$ and a $\hat{u}$ view which is at 45 degrees. Three views provide redundancy. The inclusion of a $\hat{u}$ view helps with pattern recognition (reduces confusion) and provides "triplets" which can be used in efficiency and alignment studies. Each view is made from overlapping double width extrusions with a cell size of 1cm (which gives a naive resolution of 1.4 mm). The channel count of each sector would be 1150 (all three views), for a total channel count of 36,800. The total thickness of a measuring station would again be 12 cm.

The sectors in each station will be supported above and below by rails. The support system will be designed to allow each station to be split apart vertically so it can be rolled out of the beam. The system will also be split horizontally, since there will not be enough room to roll the full station completely out of the beam.

We estimate that the cost of the iron for this system will be roughly \$500,000, and the coil packs will be \$100,000. The detector costs will be comparable for either technology. A materials and fabrication estimate for the cathode strip system, based on similar estimates by the Lab 7 group for their LHC design, is \$360,000. The Lab 7 group estimates that their electronics cost will be \$25-35

Table 13: Requirements for the Muon Detector and parameters of the baseline design.

Requirements:	
Transverse size	$\pm$ 200 mrads
Total Length	3 m
Rate capabilities	few kHz/cm^2
Baseline Design:	
Steel Length	2 m
Toroidal Field	1.5 T
No. of Longitudinal segments (steel)	2
Plane size:	20 m^2
Tube cell size	1 cm $\times$ 1cm
Wire spacing:	0.5 cm
Spatial resolution	2.5 mm
No. of channels/sector (3 views)	1150
Sectors per station	8
Total channels	36,800
Momentum resolution	$\sigma_p/p = 25\% \oplus 1\% \times p$
Total thickness/station	12 cm

per channel. This number is high, but includes the cost of the ADC required to do charge sharing. It may be possible to reduce this cost by redesigning the electronics. At a cost of \$30 channel, the cost for front-end electronics will be \$540,000. A simple latch readout scheme should be possible for the extruded tube technology, and the cost of those electronics is estimated to be \$5-10 a channel, for a total cost of \$185,000 - \$370,000. The total cost of one arm of the system, excluding triggering electronics and HV, is between \$1.14 M and \$1.50 M.

2.7.4 Front-end Electronics

The front-end electronics will be located on the frames of the sectors, as close as possible to the detector to reduce noise, signal degradation, and cabling costs. The simplest electronics design consists of an amplifier, discriminator and latch. Amplifiers and discriminators will be hybrid circuits, with a modularity of eight. After the discriminators the signals are latched, ready for the next stage of the circuit.

Since the muon system has as many as 36,800 channels, it is necessary to reduce the cost of connectors and of the long cables carrying the signals to the control room. One option is to use parallel to serial shift registers after the latches. Using an eight input shift register, the total number of lines going to the control room is reduced to 4,600. This requires an additional time of less than 100 ns to serialize the data.

A bank of serial to parallel shift registers in the control room receives the

data (without additional time because the data are pipelined). At this point it is possible to fan the data out into a FIFO for later readout and a Programmable Gate Array (PGA) for triggering. The PGA's are programmed to trigger on muon hits that form projective roads in a row of sectors. This is done for two of the views. The ouptut for each of these two views in a sector is required to be in coincidence, and this output from each sector is ORed to generate the signal for the FIFOs to be read.

When the trigger signal is sent to the FIFO, the information is coded into 9 bit addresses for readout, together with a word containing the number of addresses that will be sent.

2.8 Comparison with LHC-B

Here we address the issue of how BTeV can compete with LHC-B when and if that experiment is approved and indeed is built.

LHC-B is being designed to run at a luminosity of 2×10^{32}, which is the same as BTeV's goal. There are several inherent advantages and disadvantages that LHC-B has compared with BTeV. The issues that favor LHC-B are:

- The b production cross-section is expected to be about five times larger at the LHC than at the Tevatron.
- The mean number of interactions per bunch is expected to about 4 times lower at the LHC than at the Tevatron (at 132 ns bunch spacing).

The issues that favor BTeV are:

- BTeV is a two-arm spectrometer, which increase the signal by a factor of two compared with LHC-B.
- The short bunch spacing at the LHC, 25 ns, makes first level detached vertex triggering more difficult than at the Tevatron.
- The seven times larger beam energy at the LHC makes the range of track momenta that need to be momentum analyzed and identified much larger and therefore more difficult. The larger energy also causes a large increase in track multiplicity per event, which makes pattern recognition and detached vertex triggering more difficult.
- BTeV is designed to have the vertex detector in the magnetic field thus allowing the rejection of low momentum tracks at the trigger level. Low momentum tracks have large multiple scattering which can cause false verticizing leading to poor background rejection in the trigger.
- Use of a detached vertex trigger in Level I allows for an extensive charm physics program absent in LHC-B. It also allows for a more uniform collection of b triggers.

We believe that our triggering strategy and our geometry, coupled with the other considerations listed above, give BTeV an edge over LHC-B.

References

[1] D. Husby, P. Chew, W. Selove, and K. Sterner, Nucl. Instr. and Meth. A **383** (1996) 193.

[2] For updated vertex trigger documentation, see http://www-ese.fnal.gov/eseproj/trigger/default.htm.

[3] R. Forty, CERN-PPE/96-176, Sept. 1996 published in Proc. of the 4^{th} Int. Workshop on $B-$physics at Hadron Machines, Rome, Italy, June 1996, F. Ferroni, P. Schlein (Eds.), North-Holland, 1996.

[4] J. Wiss, *Preliminary Thoughts About the BTEV Muon System*, BTEV Internal Memo (March 1997).

[5] D. Eartly, *et al.*, *Six Layer P1 Cathode Strip Chamber Prototype*, CMS NOTE/1997 – 013 (December 1996).

3 Evolution of the C0 Program

We are very encouraged by Fermilab's decision to construct a new experimental area at C0 which is capable of supporting a large bottom and charm decay experiment. We propose to develop in stages the experiment described in detail in Section 2. Some of these stages involve R&D into key technologies required for the experiment. Others involve a program of physics measurements. We believe that our approaches are best tested by trying to do real physics measurements with the detector at various stages. Only when one tries to produce a publishable result does one truly confront all the problems of efficiency, backgrounds, and systematic errors in the measurement.

The rate at which the full experiment can be mounted depends on many things. One is when the lowβ quadrupoles will be available since this determines the earliest time when we can have collisions. Another is when the R&D for each component is completed. A third is, of course, when manpower for design work and money to build detectors and buy the electronics and computing become available. And finally, all the equipment must be installed, integrated, and made to work.

We understand that the running schedule around which we must plan our activities is the following: that each year there will be about 9 months of collider running; that there will be a three month shutdown for maintenance during which installation can take place; and that at some point after a few years of running, the 3 month shutdowns will be arranged back-to-back so that there can be a reasonable period for envisioned machine upgrades and for upgrades to one or more of the other collider detectors.

Our first goal is to get the 'large components' installed in C0 during the main injector shutdown. At the minimum, this means the SM3 analysis magnet. If we can locate the steel for one or both of the muon detectors, we would like to get that installed too. Once these components are in, all other installation activities are similar to installing components in a fixed target experiment. Individual modules of the detector can be moved into the enclosure and installed in short shutdowns of even a few days.

Between now and the end of 1999, when Run II begins, we expect to complete much of the R&D and design work. Pixel R&D, discussed in Section 5, has already begun and we would like to complete it before the year 2001. We recognize this is ambitious. Trigger R&D has also begun and will be completed by the middle of 1999. This should certainly be achievable. All detector R&D and the design of the downstream tracker, muon chambers, particle identification system, and electromagnetic calorimetry can be completed by the beginning of 1999. We would hope that prototype modules of the downstream tracker and the muon chambers could be completed by the end of 1999.

Our goal for the beginning of the run will be the following: To put some counters into C0 to measure backgrounds near the IR and in the region of the muon detector and RICH and to measure the luminosity. To set up the prototype modules of the muon detector and the downstream tracker and operate them in the C0 enclosure. To install a wire target and study the interaction

rate and backgrounds, and establish the effect on the other collision regions.

By the end of the year 2000, we would like to have all the modules of the downstream tracker, muon detector, and the EM calorimeter on one side of the IR installed and to have one RICH completed and installed. We would also at this time like to have a small (of order 15 planes) microstrip detector installed in a mockup of the evenutal housing we will use for the pixel detector. We will use this arrangement to study the initial full size pixel detector chips and to do a physics run on a wire target, emphasizing charm. The equipment available at this time should permit us to begin to do some charm physics in fixed target mode. We would also use this system to test our vertex trigger algorithms and hardware. Finally, the silicon support would be designed to accomodate a few pixel detector planes so that prototypes that should be coming available later could be tested in place.

We would hope to have our first $p\bar{p}$ collisions in 2001. We would measure the backgrounds in the collider mode. At that point, we would also have the first few stations of the pixel detector. We would interleave wire mode and collider running and test as much of the vertex tracker and vertex trigger as we could. By 2002, we would hope to have much of the pixel detector and the second side of the downstream tracker and muon detector. We would want a significant 'test run' of three or four months in collider mode and possibly some additional running in fixed target mode.

In 2003, we would hope to have the BTeV detector described in Section 2, including the full vertex detector, the second RICH, and all the EM calorimetry. We would want to run in collider mode for as much as possible of the full collider running period and believe that we would be taking real data for at least half of this period.

We look forward to full runs in collider mode at $5\times10^{31}\mathrm{cm}^{-2}\mathrm{s}^{-1}$ in 2004 and 2005.

With this plan, we can steadily build our understanding of the detector over a period of a few years and can be ready to do real physics with a tested analysis program in place when the full detector is complete. It also allows the lab to spread its resources, people and money, over several years. It allows BTeV enough time to carry out the R&D required to make it capable of extending the work of the next round of experiments just as they begin to approach their asymptotes (doubling time of the order of a couple of years). A serious forward collider B experiment will be in progress before the LHC turns on so BTeV will have a good head start over LHC-B. Morever, as the collider increases its luminosity in steps as currently imagined, BTeV will be able to take advantage of these increases without a major upgrade.

4 Physics Reach of the BTeV Detector

The continued study of heavy quark physics will yield new insights into weak interactions. The BTeV experiment will take advantage of its precision vertex detector, the vertex and other triggers, the particle identification system and the lepton identification to establish a full program of studies in heavy quark physics.

The physics reach for the BTeV detector will be described in this section. The simulation studies that are outlined here are the beginning of a program to explore the potential of the baseline spectrometer and to refine and optimize its design. We have investigated several physics channels in some detail and report them here to indicate the power of a heavy quark experiment with a Level I vertex trigger and excellent particle identification. We then contrast this with other detectors and proposed experiments.

The simulations presented are for the baseline BTeV detector described in Section 2. Our results are based on an average luminosity of $5 \times 10^{31}\mathrm{cm}^{-2}\mathrm{s}^{-1}$ for 10^7 sec. This should be a good indication of what we will be able to achieve in a year of "low" luminosity running. For the simulation studies we are taking a $b\overline{b}$ cross-section of 100 μb and a two-arm spectrometer. We believe that the results shown here are very conservative. Over the life of the experiment we plan to integrate over a much larger time than 10^7s and we believe that an optimized detector will be able to run with a factor of 4 higher peak luminosity.

The estimates of sensitivity for each final state are based on combining our geometric acceptance, our trigger acceptance, and the efficiency of realistic analysis cuts which are necessary to reduce backgrounds for that particular state. Detector effects which contribute to the track, momentum and vertex resolutions are modeled parametrically including the effects of multiple scattering.

The trigger efficiencies are determined by an algorithm which includes pattern recognition and a fast determination of the primary vertex and "secondary" tracks which miss the vertex. Though we quote current results from this algorithm, it is not yet optimized and we expect to improve it with more work. The simulation studies have been quite useful, in that they have helped us address many detector design issues. Here we use them to show the large potential physics reach of BTeV.

The issues for which we quote simulation results in this EOI are a small subset of the physics issues that we intend to investigate. A broader perspective of the physics potential can be found in Section 1. Here we show results on B_s mixing using the final state ψK^*, the CP asymmetry in $B^o \to \pi^+\pi^-$, a rare decay channel $B^- \to K^-\mu^+\mu^-$ and for comparison with other experiments the CP reach in $B^o \to \psi K_s$. We also show some studies of the efficiency for flavor tagging the other b. We also quote some initial results on the study of charm decays, where the enormous potential of hadron colliders in the forward direction has been overlooked.

To measure B_s mixing, the detector needs to have excellent b lifetime resolution. This lifetime resolution is also very useful for all b and c decays in separating the decay vertices from the interaction vertex and thus reducing

combinatoric backgrounds. The $\pi^+\pi^-$ final state is an example not only of a very important decay mode, but also of a low multiplicity hadronic final state. Detecting this mode is one of the main goals of the vertex trigger algorithm. We also include trigger results on the ψK^* final state just using the detached vertex trigger (even though the muon trigger will also be used for this state) since it is an example of four-body b decay.

For some of these modes and for the kaon tagging study we present comparisons with what a central geometry detector at the collider could accomplish.

Many more simulations are necessary. For example, we are just beginning to study states in which a B-meson decays into a charm meson, resulting in a a tertiary vertex. States such as $B_u \to D^o K$ and $B_s \to D_s K$, which involve charm vertices, can be used to measure $\sin\gamma$. Similarly, we discuss $B_s \to D_s 3\pi$ in connection with the measurement of x_s. Also, we have not yet studied what could be done on final states with photons or π^o's, such as $K^*\gamma$ or $\pi^+\pi^o$. We are just starting the investigation of directly produced charm final states.

4.1 Simulations

Pythia 5.7 and Jetset 7.4 [1] were used to generate physics processes for the BTeV simulation studies described below. Heavy quark decays were then modeled through the CLEO decay Monte Carlo QQ 9.2 [2].

For these studies the size of the interaction region was taken as $\sigma_x = \sigma_y = 50\mu$m and $\sigma_z = 30$ cm corresponding to our current understanding of the running conditions in the C0 interaction region. The average number of interactions per crossing is expected to be less that 0.5 at a luminosity of $5 \times 10^{31}\text{cm}^{-2}\text{s}^{-1}$ which means that there will sometimes be more than one interaction per crossing. The effects of multiple interactions per crossing have not yet been accounted for in these studies. We believe, however, that the length of the interaction region and the station repetition in the vertex detector design will allow us to separate tracks from two different primary interactions in each event as long as the interactions are more than a few centimeters apart.

The first goal of the simulation studies was to determine the best geometry configuration for a heavy quark experiment at the Tevatron. The geometries initially studied included:

- Collider; Central Geometry with a Solenoid Magnet ($|\eta| < 1.5$)
- Collider; Forward Geometry with a Dipole Magnet ($1.5 < |\eta| < 4.5$)
- Collider; Combined Geometry with a Solenoid Magnet and Dipole ($|\eta| < 4.5$)
- Fixed Target; with a Dipole Magnet

Space constraints in the Tevatron collision halls essentially eliminated the option consisting of both a solenoid and a dipole magnet. We have investigated the other options and present the results for the collider operation where the cross sections are higher.

To complete the physics studies a new software tool MCFast[3] was used extensively. This package handles simple detector geometries containing solenoid and dipole magnetic fields in a unified analysis framework which is ideal for comparing different detector geometries.

4.1.1 MCFast Simulation package

Most physics simulations for BTeV were carried out using MCFast v2_6, a new fast Monte Carlo package developed by the Fermilab Computing Division for detector design studies. MCFast provides a general framework for the comparison of differing detector geometries and is interfaced to a variety of generators that simulate the production and decay of B hadrons in a collider environment or fixed target environment.

The primary goal of MCFast is speed and flexibility which is achieved through parameterization. The package was designed to serve as an analysis tool that could be used to compare the physics reach of a variety of detector

options. The program emphasizes fast tracing of particle trajectories through simple geometrical shapes. Tracking is based on a Kalman filter technique[4][5] and smeared particle trajectories are supplied to the user for further analysis. Hit generation has been included in the MCFast package for use in trigger simulations. Parameterized showering has been implemented so that it is possible to simulate electromagnetic and hadronic showers and energy deposition inside calorimeters and absorbers. An interface between the MCFast geometry and GEANT has been written to enable more detailed simulations.

MCFast simulations currently include detector effects with gaussian errors. The effects of multiple scattering are taken into account in tracking and in hit generation. The simulation package provides tools that allow the user to include the effects of the large interaction region and of multiple interactions in the simulations. Decays in flight, pair conversions and bremsstrahlung can also be included in the simulations.

The code is written primarily in Fortran and C and is interfaced to the standard HEP event generators Pythia, Herwig[6] and Isajet[7] through the StdHep interface. The decay of charm and bottom hadrons is done by QQ, a Monte Carlo package developed for CLEO. A 3-D Graphics package based on SGI-Explorer has been developed to display the detector geometry, tracks and hits. An Open Inventor based display package is under development. A new version of MCFast containing a more general tracing algorithm written in C^{++} and a true Kalman filter track fitter is currently under development and is expected to be released soon. These improvements are required in order for us to develop pattern recognition algorithms, to study the trigger algorithms and will allow us to add detector elements such as a beampipe into the BTeV detector description.

4.2 B_s Mixing with $B_s \to \psi \bar{K}^{*0}$

The decay chain $B_s \to \psi \bar{K}^{*0}$, $\psi \to \mu^+\mu^-$, $\bar{K}^{*0} \to K^-\pi^+$ has been proposed [8] as an excellent mode with which to measure the B_s mixing parameter, x_s. Although this mode is Cabibbo suppressed, many other factors are in its favor: the final state consists of a single detached vertex; it has a relatively low multiplicity; the state is triggerable with several independent strategies, including impact parameter triggers, secondary vertex triggers and muon or di-muon triggers. These factors ensure an excellent time resolution and a good total efficiency.

In this section the x_s reach of BTeV using the mode $B_s \to \psi \bar{K}^{*0}$ will be discussed. This study was carried out in several steps, the first step being an MCFast based simulation of the BTeV detector, which was run on samples of both signal and background events. The output of this step was treated as real data and passed through a physics analysis program to determine the various efficiencies, resolutions and background levels. A mini-Monte Carlo then used the detector response determined in the previous step to generate many samples of proper time distributions for different values of x_s. These distributions were then fitted to determine the x_s reach of the detector.

In the simulation step, $p\bar{p} \to b\bar{b}X$ events were generated using Pythia version 5.7 and Jetset version 7.4 . All charmed and bottom hadrons were decayed using QQ. In order to simplify the analysis, all B_s mesons were forced to decay into the signal channel and all $\bar{B}_s$ mesons were permitted to decay generically, but with mixing disabled and with the charge conjugate of the signal channel excluded. The effects of mixing and mistagging will be included later in this section.

The first step in the simulated analysis was to form ψ candidates from pairs of oppositely charged tracks. Each track was required to have at least four hits in the pixel detectors, to have a momentum of at least 5 GeV/c, and to pass through the fiducial volume of the muon detector system. Tracks which passed the above criteria were assumed to be perfectly identified as either muons or non-muons. If the invariant mass of the di-muon combination satisfied a loose cut around the mass of the ψ, then the combination was accepted as a ψ candidate and the mass of the combination was constrained to that of the ψ.

Next, $\bar{K}^{*0}$ candidates were formed from oppositely charged pairs of tracks, with the negative track assigned the K^- mass and the positive track the π^+ mass. Each track was required to have at least four hits in the pixel detectors and the kaon candidate was required to have a momentum in the range $3.0 \leq p_K \leq 70.0$ GeV/c and to pass through the fiducial volume of the RICH detector. The pion candidate was required to have a minimum momentum of 0.5 GeV. It was assumed that the RICH detector would correctly identify 97.5% of all true K^- candidates which passed the above cuts and that it would allow 2.5% of non-kaons to be accepted as kaons. This parameterization of the RICH performance was chosen for consistency with other simulations reported in this EOI and it is a conservative estimate of the performance of an actual RICH detector. No particle ID requirements were placed on the π^+ candidate. If a combination satisfied the K^* mass within broad cuts, the combination was saved as a $\bar{K}^*$

candidate.

All combinations of ψ candidates plus $\bar{K}^*$ candidates were then formed, excluding combinations which shared tracks. It was required that the the mass of the four track combination fall within a large window around the B mass and that the momentum of the combination be greater than 15 GeV/c. Combinations passing these requirements were fitted to a single vertex and were retained if the probability of χ^2 for the vertex fit was greater than 0.005. When a combination passed the above cuts, a primary vertex for the event was found and fitted. If multiple combinations in a single event satisfied the above selection criteria, the primary vertex pattern recognition and fit were redone for each combination.

At this stage, the following quantities, and their errors, were computed for each combination: the decay length L, the proper decay time τ and the 3D distance of closest approach between the trajectory of the combination and the primary vertex, d_{3D}. The distribution of the above quantities for signal combinations generated with $x_s = 20$ is shown in the left hand parts of Fig. 44. The right hand parts of that figure show the distributions of the errors on these quantities. Combinations were considered for further analysis provided $L/\sigma_L > 10$ and $d_{3D} < 3\sigma_{d_{3D}}$. Also, candidates with poor time resolution were rejected by demanding $\sigma_\tau \leq 0.09$ ps.

The above analysis was run on a file of Pythia $p\bar{p} \rightarrow b\bar{b}X$ Monte Carlo events which contained one signal decay in each event. The invariant mass of all combinations passing the above cuts is shown in Fig. 45a). The B_s signal is prominent. Figures 45b) and c) separate the entries of part a) into two subsets: b) those entries tagged by MCFast as coming from true signal combinations and c) the remaining entries. Although most of the entries in part c) contain two or three tracks from true signal combinations, the distribution in part c) does not peak in the signal region. Part d) of the figure shows the distribution of the measured proper decay time minus the generated proper decay time ($\tau_M - \tau_G$) for true signal combinations. A fit to this distribution determined that the RMS time resolution is 0.045 ps.

From the distribution in Fig. 45b), the mass resolution for the signal is determined to be $\sigma = 5.2 \pm 0.2$ MeV/c^2 and the efficiency is determined to be 0.038 ± 0.002. Here the efficiency includes the geometric acceptance of the detector and the efficiency of the analysis cuts; it does not, however, include the trigger efficiency or the efficiency for the tag which is required for mixing studies. This efficiency can be combined with other factors summarized in Table 14 to predict that 1730 events per year will pass the above cuts.

The present incarnation of the secondary vertex trigger simulation predicts that 0.50 ± 0.03 of the events passing the analysis cuts will also pass the trigger. The trigger simulation, however, has not been carefully tuned and it is expected that the fraction accepted by the trigger will rise as more is understood about triggering B events in this environment. For reference, 13% of all generated events pass the trigger. Also, 36% of all events in which all four B_s daughters are reconstructed pass the trigger.

One of the important features of this mode is that it allows redundant trig-

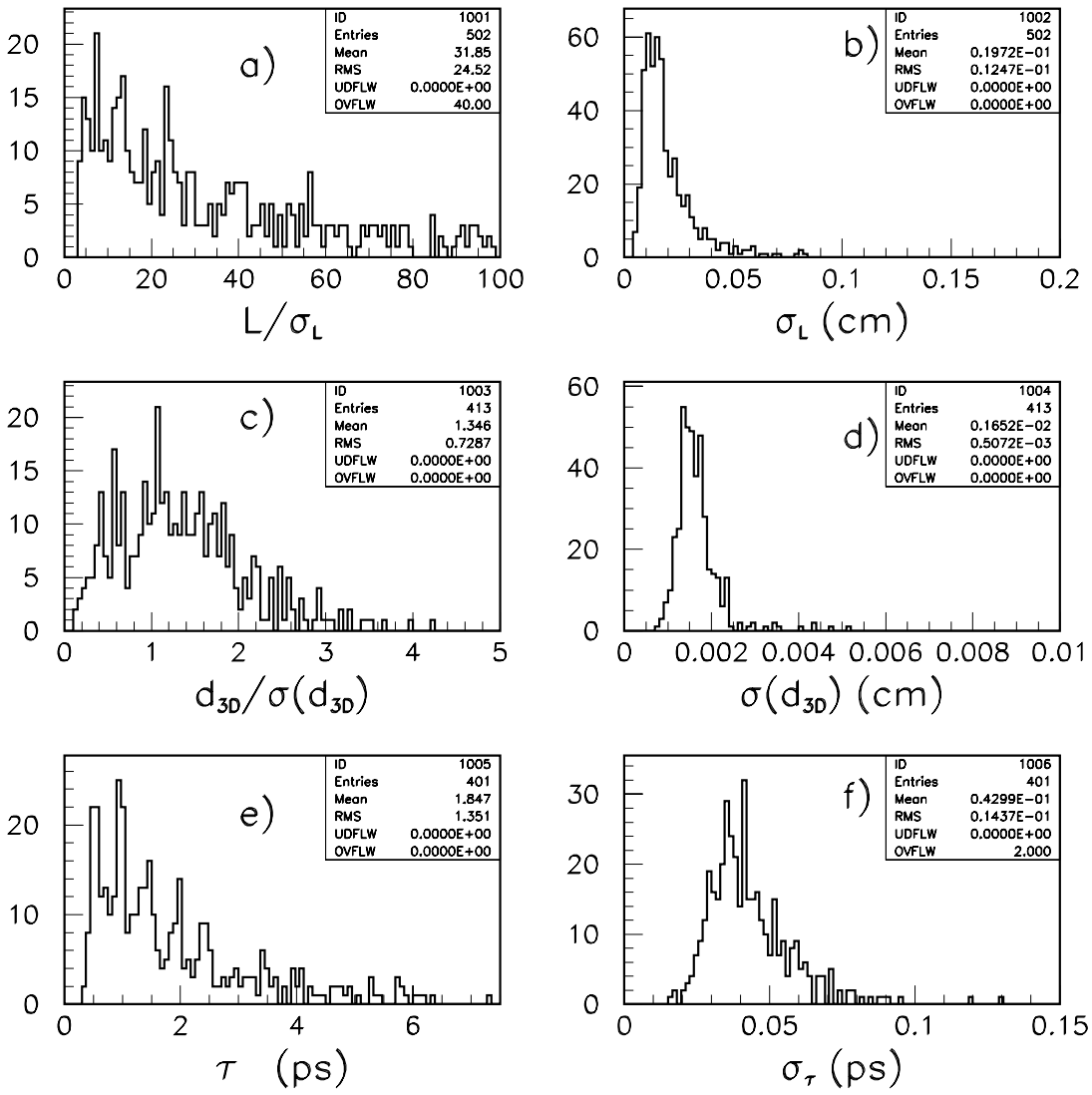

Figure 44: Distributions of important analysis cut quantities for $B_s \to \psi \bar{K}^{*0}$. These distributions are for a sample of events which were generated with $x_s = 20$ and with a lifetime distribution which corresponds to a mistag fraction of 0.25.

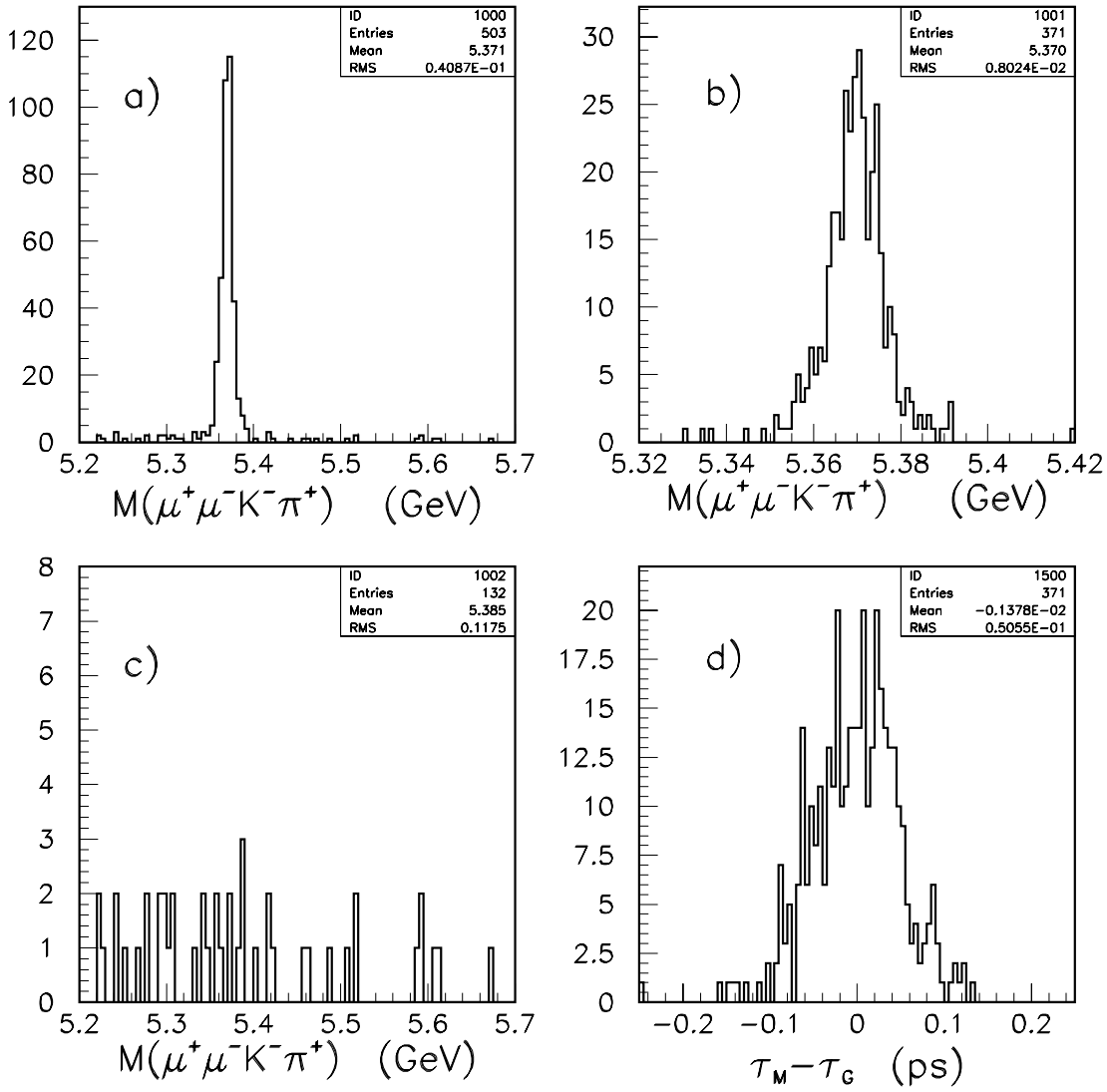

Figure 45: Resolutions and Backgrounds in $B_s \to \psi \bar{K}^{*0}$ signal events. Part a) shows the invariant mass distribution for all combinations in a signal event which pass the analysis cuts. Parts b) and c) show disjoint subsets of the entries in a): b) for true signal combinations and c) for the remaining combinations. Part b) also illustrates the mass resolution while part d) shows the resolution on the proper decay time.

Quantity	Value	Yield (Events/year)
Luminosity:	$5 \times 10^{31} cm^{-2} s^{-1}$	
One Year:	$10^7 s$	
$\sigma_{b\bar{b}}$:	$100 \mu b$	
$\mathcal{B}(B_s \to \psi \bar{K}^{*0})$:	8.5×10^{-5}	
$\mathcal{B}(\psi \to \mu^+ \mu^-)$:	0.061	
$\mathcal{B}(\bar{K}^{*0} \to K^- \pi^+)$:	0.667	
$\mathcal{B}(\bar{b} \to B_s)$	0.13	45500
ϵ(Geometric)	0.19	
ϵ(Analysis cuts)	0.20	1730
ϵ(Trigger)	0.85	1470
ϵ(Tag)	0.15	220
Include $\psi \to e^+ e^-$		330
Mistag fraction	0.15	

Table 14: Projected Yield for $B_s \to \psi \bar{K}^{*0}$ in one year of BTeV running. The numbers in the third column give the expected yield when all of the factors down to and including that line have been considered. The estimate for $\mathcal{B}(B_s \to \psi \bar{K}^{*0})$ was obtained from [8] and that for $\mathcal{B}(\bar{b} \to B_s)$ was obtained from [9]. The trigger efficiency is quoted as a fraction of those events which pass the analysis cuts. The tagging efficiency and mistag fraction are quoted from the sum of clean tagging modes only.

gering possibilities. The analysis cuts described above ensure that both muons are well within the acceptance of the spectrometer and one can envisage that a di-muon trigger would be highly efficient. Therefore, it is estimated that about 85% of the events which pass the analysis cuts will trigger, as quoted in Table 14.

In order to measure x_s, it is necessary to tag the flavor with which the B_s meson was created. The studies described in section 4.7 determined that opposite side $K^{\pm}$ tagging will have an efficiency of 0.12 with a mistag fraction of 0.15 and that opposite side muon tagging will have an efficiency of around 0.03, also with a mistag fraction of 0.15. These tags correspond to $\epsilon D^2 = 0.075$. As discussed in section 4.7, it is expected that the total tagging power will reach $\epsilon D^2 = 0.10$. The additional power will come from tags with much higher efficiency but also with much higher mistag fractions. For purposes of the simulations discussed below, only the clean tags will be considered.

Finally, the expected yield can be increased by a factor of at least 50% by using the mode $\psi \rightarrow e^+e^-$. This mode will have an efficiency for secondary vertex triggers which is comparable to that for $\psi \rightarrow \mu^+\mu^-$ and, an as yet unspecified, electron trigger is part of the BTeV reference design.

The backgrounds to the signal processes come from several sources. Most likely the most important background process will be $B \rightarrow \psi X$, $\psi \rightarrow \mu^+\mu^-$ which occurs with a product branching fraction of about 8×10^{-4}. When 10000 events of this decay chain were passed through the analysis code and the trigger simulation, only 2 entries survived anywhere in the mass plot. When 200000 each of generic b decays and generic charm decays were passed through the analysis code and the trigger simulation, no entries survived anywhere in the mass plot. In all of these cases, higher statistics Monte Carlo runs are needed before any conclusions can be drawn. Another likely source of background is events which contain two semileptonic decays of either b or c hadrons. Studies on all of the above backgrounds are continuuing. It is also important to remember that, should some of these backgrounds be large, there remains significant headroom in the analysis cuts.

Some sources of background which one might at first think to be important turn out not to be a problem. First, the more copious $B_s \rightarrow \psi\phi$ final state is not a significant source of background because of the excellent particle ID provided by the RICH system. Second, the mass resolution is sufficient to separate the much more copious decay $B_d \rightarrow \psi\bar{K}^{*0}$.

The final step in the study was to use a mini-Monte Carlo to study the x_s reach of the apparatus. Figures 46a) and b) show the proper time distributions which result from one run of the mini-Monte Carlo for 330 events (approximately one year of BTeV running), with $x_s = 20$, a mistag probability of 15% and a smearing in proper time of 45 fs. It was also required that the smeared decay time be greater than 400 fs, which simulates the cut of $L/\sigma_L > 10$. Except of the treatment of mistags, there are no background contributions in these simulations. Part a) shows the proper time distribution for unmixed decays while part b) shows the distribution for mixed decays. Part c) of the figure shows, as a function of x_s, the value of the unbinned negative log likelihood function computed from these events. A step of 0.5 in the negative log likelihood func-

tion determines the 1 σ error bounds and a line is drawn across the figure at the level of the 5 σ error bound. A clear minimum near the generated value of x_s is observed and the likelihood function determines the fitted value to be $x_s = 20.08 \pm 0.09$.

The error returned by the fit was checked in two ways. First, an ensemble of mini-Monte Carlo experiments was performed and the errors were found to correctly describe the dispersion of the measured values about the generated ones. Second, the errors returned by the fit were found to be approximately equal to the Craemer-Rao minimum variance bound [10]. This analysis closely follows that of reference [11].

The mini-Monte Carlo also showed how the limiting x_s sensitivity of the experiment is approached. As the number of events in a trial is reduced, the negative log likelihood function becomes more and more ragged and the secondary minima approach the significance of the global minimum. Eventually there are secondary minima which reach depths within 12.5 units of negative log likelihood (5σ) of the global minimum. When this happens in a sufficiently large fraction of the trials, one must conclude that only a lower limit on x_s can be established. In the region of the parameter space which was explored, the absolute error on x_s was no more than 0.2 or 0.3 when this limit was reached.

The above exercise shows that one cannot reliably determine the x_s reach of the experiment by simply looking at the minimum variance bound on x_s or by scaling results by $\sqrt{\epsilon}D$. Therefore a more complex treatment is needed in order to estimate how much the x_s reach can be extended by incorporating the tags which have large mistag fractions. The method will be to create separate pairs of mixed and unmixed proper time distributions for each tag type and to perform a simultaneous fit to the complete set of histograms. This work is underway.

To give one more example, the mini-Monte Carlo indicates that it will be difficult, but not impossible, to measure x_s of 40 in one year of running. On the other hand, it is very likely that it can be measured in two years of running. An example of a typical mini-Monte Carlo run for $x_s = 40$ and two years of running is shown in Fig. 47.

The results of the mini-Monte Carlo runs for different values of x_s and different running periods are summarized in Fig. 48. Any value of x_s under about 30 is easily accessible in one year of BTeV running under the nominal startup conditions. An x_s of about 40 comes within the reach of BTeV after about two years of running. The detector has the time resolution necessary to probe higher values of x_s provided the forseen increase in luminosity is achieved.

The workplan for this analysis is to determine the background levels and the lifetime characteristics of the backgrounds. The fitter will also be extended to allow the use of several tags with different mistag fractions. Using this new information and new technology, the x_s reach will then be reevaluated.

We focus on B_s decays to $J/\psi K^*$ for measuring mixing because it is clean, easy to trigger and has excellent time resolution. The relative branching fraction of $B_s \to D_s^+ \pi^-$ and $B_s \to D_s^+ \pi^+ \pi^- \pi^-$ with $D_s \to K^+ K^+ \pi^-$ are higher by about two orders of magnitude and ought to provide a larger sample of B_s

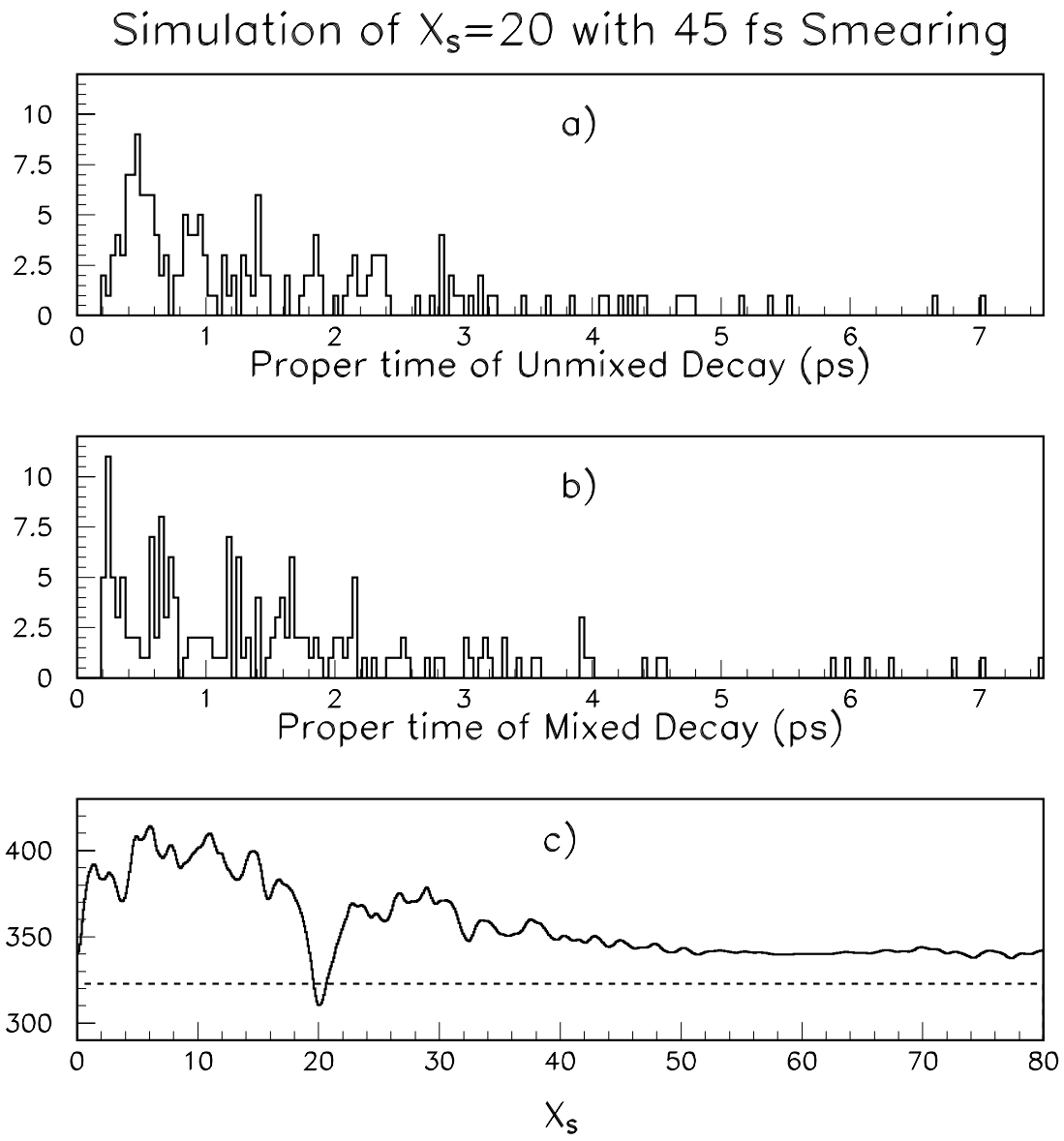

Figure 46: Mini-Monte Carlo Proper Lifetime plots of a) unmixed and b) mixed decays for one BTeV year of $B_s \to \psi \bar{K}^{*0}$ with $x_s = 20$, a mistag fraction of 0.15 and a time smearing of 45 fs. Part c) shows the corresponding negative log likelihood as a function of x_s. The dashed line marks the level above the minimum which corresponds to 5 σ significance.

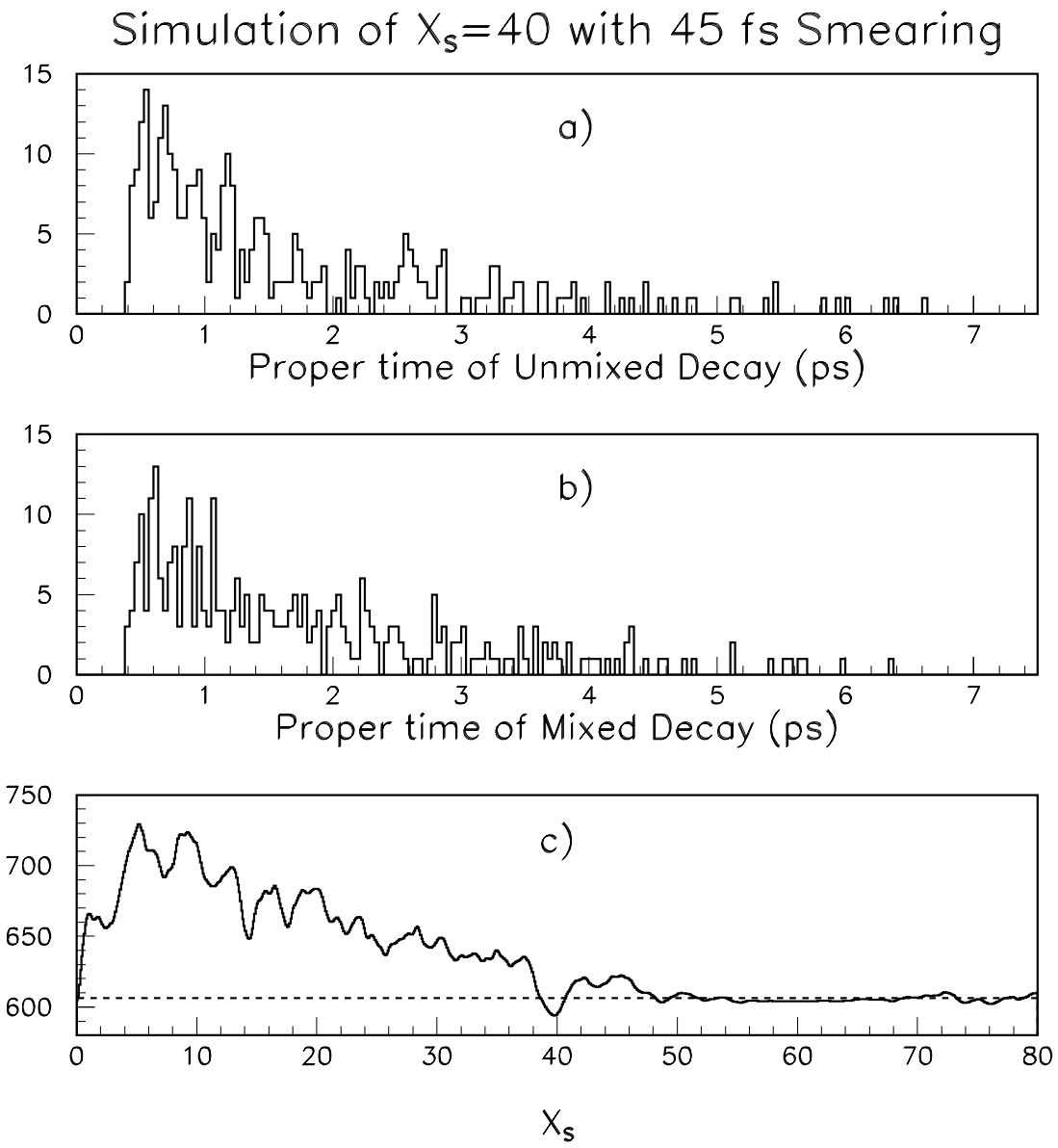

Figure 47: Mini-Monte Carlo Proper Lifetime plots of a) unmixed and b) mixed decays for two BTeV years of $B_s \to \psi \bar{K}^{*0}$ with $x_s = 40$, a mistag fraction of 0.15 and a time smearing of 45 fs. Part c) shows the corresponding negative log likelihood as a function of x_s. The dashed line marks the level above the minimum which corresponds to 5 σ significance.

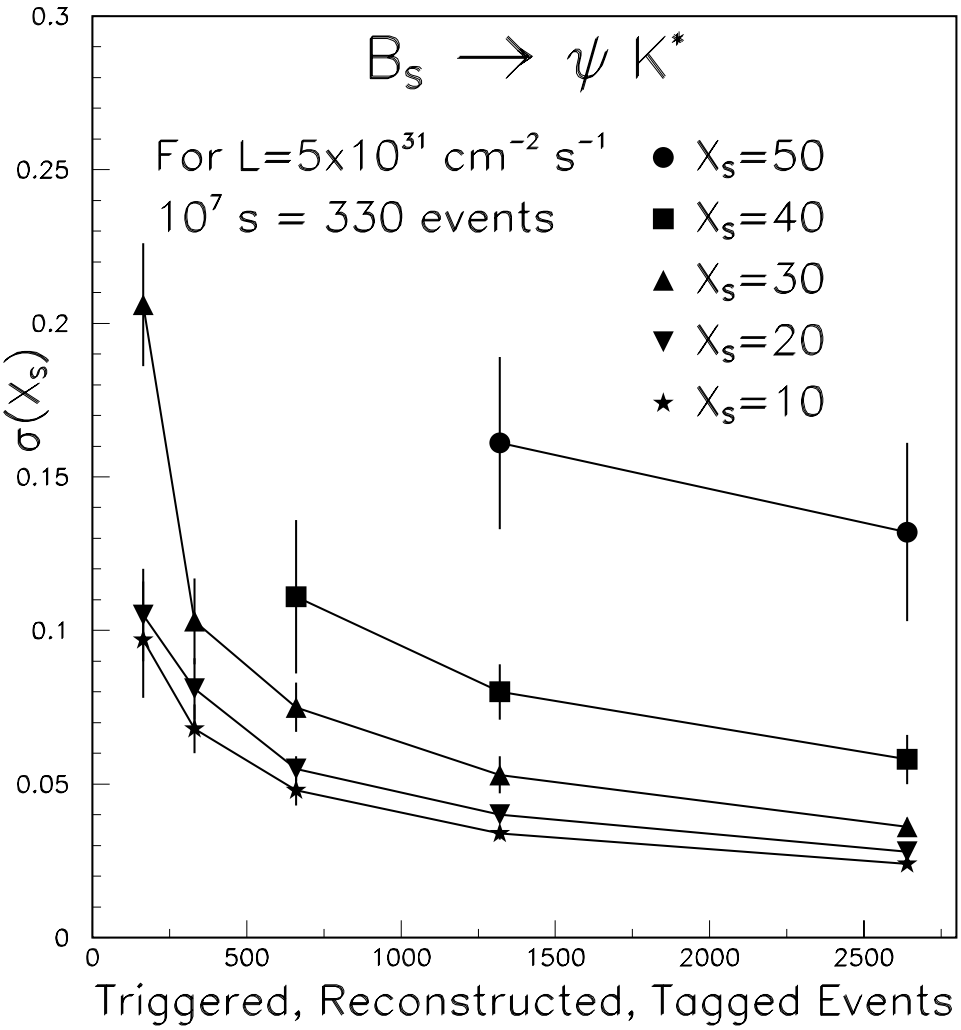

Figure 48: x_s reach as a function of event yield for $B_s \rightarrow \psi \bar{K}^{*0}$. The horizontal axis covers up to 8 years of running under the nominal startup conditions, which is 2 years of running with the anticipated final luminosity. Each data point was obtained by running the mini-Monte Carlo 20 times and obtaining the measured error on x_s for each run. The simple mean of these values is plotted as the central value of each data point. The rms width of the errors from the 20 runs is plotted as the vertical error bar. The lines connecting each point are to guide the eye. The data points for $x_s = 40$ and higher do not extend to low values on the horizontal axis because the detector cannot resolve such an x_s with that level of statistics.

decays for our mixing studies. This represents a real challenge to our trigger, our particle id, and especially our ability to cleanly associate the D_s and the pions to a common vertex and accurately measure the decay proper tiem without introducing a lot of background. Our preliminary work on the 3π indicates that the trigger will be about 50% efficient for decays that would be reconstructable in the spectrometer. The trigger efficiency as a function of the proper decay time is shown in Fig. 49. It is interesting to note that the lowest trigger efficiency is found among events at low proper time, i.e. those events that are least useful for determining x_s.

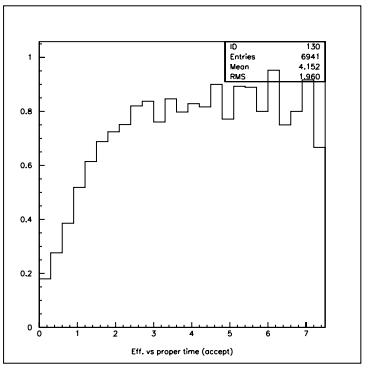

Figure 49: The trigger efficiency for $B_s \to D_s \pi\pi\pi$ is shown as a function of the proper time.

Our preliminary work indicates that the yield of B_s in the $D_s 3\pi$ mode will be larger than for $J/\psi K^*$, however, the time resolution is expected to be not quite as good, 65 fs [12]. The degraded time resolution makes it difficult to achieve an x_s reach of 40 with this mode. However, with a yield in one year of running of several thousand reconstructed events in this mode we can reach x_s of 30.

4.3 CP violation in $B_d \to \pi^+\pi^-$ Decays

The decay $B_d \to \pi^+\pi^-$ is the traditional choice for measuring $\sin(2\alpha)$.

The signature for this decay is very simple: two oppositely charged tracks with a displaced vertex and the invariant mass of a B^0. Most of the background rejection against random combinations must come from the secondary vertex. While particle identification is vital to reject backgrounds from decays like $B^0 \to K^+\pi^-$ and $B_s \to K^+K^-$, it has a small effect on random combinations since most particles are pions.

It has been shown by the BCD group [13] that the dominant background to $B^0 \to \pi^+\pi^-$ comes from random combinations of tracks in events containing B's. Tracks from real B's are already displaced from the primary vertex and have a higher probability of faking a secondary vertex. We have chosen to optimize our selection to minimize the background from real B decays. Further studies will be needed to confirm that this is also sufficient to reject charm and light quark backgounds.

For this analysis we fit the primary vertex from tracks that are known to come from the primary. This underestimates the error on the primary but not significantly and the error on the decay distance is still dominated by the secondary decay. We loop over all opposite sign tracks with nine or more hits in the silicon vertex detector and try to fit a secondary vertex. Those with $\chi^2 < 8.0$ are kept for further analysis. After these fits we need to make four selections to reduce the random backgrounds:

- the cosine of the opening angle of the $\pi^+\pi^-$ pair must be greater than –0.75. Random tracks that are in opposite hemispheres of the detector produce masses near the B, while real B's never have opening angles this large.

- require that the distance between the primary and secondary decay divided by its error, L/σ, be greater than 10. This cut strongly rejects random combinations where tracks come from the primary vertex.

- require that each pion miss the primary vertex by more than 5 times its error on the impact parameter with respect to the primary vertex. This is correlated with the previous cut, but it can reject situations where a primary vertex track crosses another track making a false secondary vertex.

- require that the B^0 point back to the primary vertex within 2 σ of its point back error. This requirement rejects false vertices that consist of two tracks from different secondary decays.

Pattern recognition in the silicon sets the requirement that each of the two π track candidates have hits in 9 planes (3 stations) of the vertex detector. The geometric acceptance for $B^0 \to \pi^+\pi^-$ where both tracks are required to hit 3 stations is about 30%. The reconstruction of the primary and secondary vertices

and the background rejection cuts have an efficiency of 11.2% which means that over one third of the events in the acceptance remain after the cuts are applied.

There are several decay modes of B mesons that can mimic a $B_d \to \pi^+\pi^-$ decay. The decay $B_s \to K^+K^-$, which is due to a hadronic penguin decay mechanism, is the most important with other contributions from $B_d \to K^+\pi^-$ and $B_s \to K^-\pi^+$. Recent results from CLEO show a confirmed signal for the $B_d \to K^+\pi^-$ decay and an upper limit on the decay of interest, $B_d \to \pi^+\pi^-$ [14]. While many people have previously made assumptions that the $\pi\pi$ mode was larger than or equal to the $K\pi$ mode, it now appears that the $K\pi$ mode is larger. Based on the CLEO yields of each we will make a conservative assumption that $B(B_d \to K^+\pi^-)$ is twice a large as $B(B_d \to \pi^+\pi^-)$.

$B_s \to \pi^+K^-$ is a $b \to u$ transition of the B_s similar to the decay $B_d \to \pi^+\pi^-$, and $B_s \to K^+K^-$ is a hadronic penguin. The modes of B_s decays are normalized by having the total B_s production be 34% of B_d production [9]. In addition, we expect that the penguin and $b \to u$ decays of the B_s will have the same pattern of branching ratios as the B_d.

Using the above results as input, we simulate the two pion mass plot without particle identification in Fig. 50. The plots make it clear that kinematic separation is inadequate to discriminate between these decays. The width and separations for the signals in the mass plot are almost identical to CDF's prediction in their TDR [15], although they used a more favorable ratio of $K\pi$ to $\pi\pi$ which the new CLEO data puts in doubt.

MCFast does not simulate the RICH response, but it can model the geometric acceptance and momentum threshold. If we assume 100% particle identification, we only lose 16% of the events that pass our vertex cuts due to the RICH acceptance and threshold. This leaves 9.3% of all the generated events. Misidentification in the RICH at the 1-2% level will produce a background that is quite small compared to the background due to random combinations and it can be ignored.

If our trigger requirement is two tracks with more than 4σ significant miss distance from the primary vertex, then we would expect a strong correlation between triggered events and reconstructed events. The simulation shows that 72% of our reconstructable events pass this trigger. Such a trigger requirement rejects the light quark background at a rate of 250 to 1. This leaves us with 17000 events per year of running before tagging has been done. This compares well with 10000 triggered and reconstructed events in 2 fb^{-1} that CDF reports in their upgrade TDR [15].

Our signal to background estimate is based on 800,000 generic B events. From this sample only 4 events have a B mass that lies between 5.1 and 5.4 GeV, and if we scale to a B signal region which is 96 MeV wide (σ = 16MeV) we expect 1 event under the peak. If we assume a branching ratio $B(B_d \to \pi^+\pi^-) = 0.75 \times 10^{-5}$, then our $S/B = 0.4$ but with large errors due to limited statistics of the current simulations. Study of larger samples of backgrounds may allow us to understand how to improve our signal to background ratio.

The tagging efficiency, which is discussed in Section 4.7, is estimated to be 10%. We can combine these results to find an uncertainity on $\sin(2\alpha)$ fol-

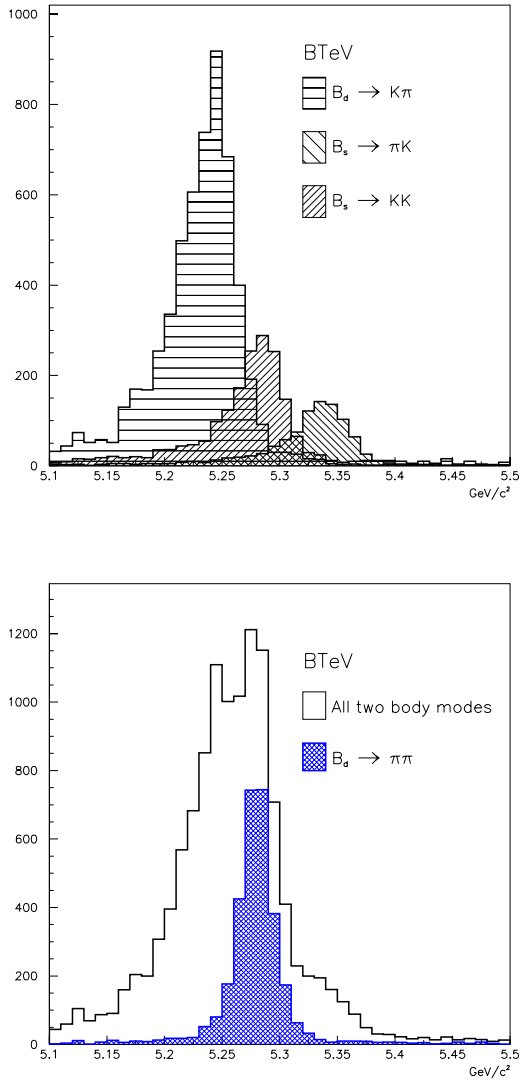

Figure 50: Two body mass plots without particle identification a) including contributions from $B_d \rightarrow K^+\pi^-$, $B_s \rightarrow \pi^+K^-$, $B_s \rightarrow K^+K^-$, b) $B_d \rightarrow \pi^+\pi^-$ and a sum of all two body decay modes. All particles are assumed to be pions.

Table 15: Project yield of $B^0 \to \pi^+\pi^-$ and the uncertainity on $\delta \sin(2\alpha)$

Luminosity	$5 \times 10^{31}\mathrm{cm}^{-2}\mathrm{s}^{-1}$
Running time	10^7 sec
Integrated Luminosity	500 pb^{-1}
$\sigma_{b\bar{b}}$	100 μb
Number of $B\overline{B}$ events	5×10^{10}
Number of B_d^0's	3.5×10^{10}
BR($B_d^0 \to \pi^+\pi^-$)	0.75×10^{-5}
Reconstruction efficiency	0.09
Trigger efficiency	0.72
Number of reconstructed $B_d^0 \to \pi^+\pi^-$	1.7×10^4
Tagging efficiency ϵD^2	0.10
S/B	0.40
$\delta \sin(2\alpha)$	0.10

lowing the same procedure as the previous section. Our results are shown in Table 15 [16].

4.4 CP Violation in $B_d^0 \to J/\psi K_s$

The decay $B_d^0 \to J/\psi K_s$ is the golden channel for measuring the CP violating angle β as shown in Section 1. Though we expect that CP violation in this mode will have been observed before BTeV starts, we include it here for comparison purposes. A study has been made of the geometric acceptance and reconstruction efficiency of the proposed BTeV detector for the decay $B_d^0 \to J/\psi K_s \to \mu^+\mu^-\pi^+\pi^-$. The geometric acceptance and resolution is shown in Table 16 and compared with a Tevatron central detector modeled on CDF.

The dominant backgrounds to the decay channel $B^0 \to J/\psi K_s$ are expected to arise from J/ψ's from B-decays combining with real K_s's from fragmentation or J/ψ's coming directly from hadronization combining with any K_s. Decays of B mesons with both a J/ψ and K_s in the final state, such as $B_d^0 \to J/\psi K^{*0}$, have an upper limit in the $J/\psi K_s$ spectrum at 5.15 GeV.

CDF found that prompt J/ψ's are a large fraction of total J/ψ production [17] and that this fraction increases at p_T decreases. In the forward geometry of the BTeV/C0 detector the p_T of the accepted J/ψ's peaks at about 2 GeV/c (See Fig 51). Extrapolating from the CDF results we expect that J/ψ's from B decays only comprise about 5% of the total J/ψ production. Background from fake or prompt J/ψ's can be reduced by a cut on the distance between the primary vertex and decay vertex. Monte Carlo events of the type $B \to J/\psi X$ were generated to study the background arising from J/ψ's from B-decays.

Table 16: Comparison of Acceptance ϵ and Resolution of BTeV and a Central Detector for $B_d^0 \to J/\psi K_s^0$

	J/ψ		K_s		B	
	ϵ	width	ϵ	width	ϵ	width
BTEV/C0	18.1%	9.5 MeV	32.9%	2.5 MeV	9.1%	12.7 MeV
CDF II	11.2%	9.5 MeV	34.0%	2.7 MeV	6.7%	13.6 MeV

The following requirements were put on all events:

- Each event must pass a primary vertex fit.
- J/ψ candidates were selected by combining pairs of oppositely charged tracks identified as muons. The muons were required to have a momentum greater than 5.0 GeV/c, and have a least one hit in the muon detector. These tracks were then required to pass a vertex fit. The normalized distance between the primary vertex and J/ψ vertex (L/σ_L) was required to be greater than 3.0. This cut is 83% efficient for the signal and rejects 99.8% of the background from prompt J/ψ's (see Fig 52).

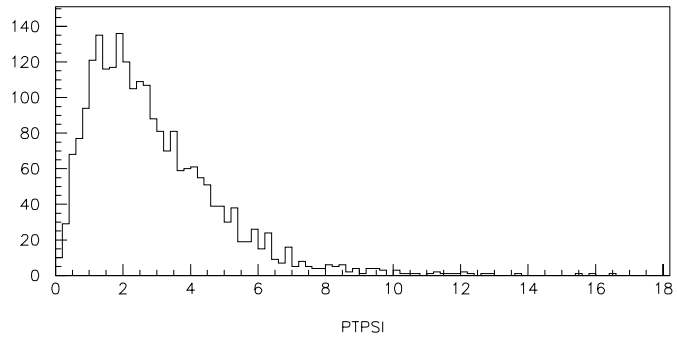

Figure 51: p_T distribution of J/ψ's

- K_s candidates were selected by combining pairs of oppositely charged tracks with a minimum momentum of 0.5 GeV and fitting them to a vertex. Each track was required to miss the primary vertex by at least 3σ and the reconstructed K_s was required to point back to the J/ψ vertex to within 5σ. (Figs 53 and 54).

- The J/ψ and K_s^0 candidates within a 3σ mass window of the nominal values were combined to form B_d^0 candidates. To reduce the background from a K_s^0 from the primary vertex combining with a J/ψ from a B decay we require the K_s impact parameter to the secondary vertex divided by the impact parameter to the primary vertex to be less than 2.0. We also require that the reconstructed B^0 point back to the primary vertex.

The reconstructed signal and scaled background are shown in Fig 55. The reconstruction efficiency of the signal is 4.9%.

The number of signal events expected in 10^7 sec of running time is shown in Table 17. We estimate that the efficiency of a dimuon trigger with a threshold of 10 GeV/c is 70% for events which pass the analysis cuts. The efficiency of the secondary vertex trigger is approximately 30% for these events and the total trigger efficiency is estimated to be 80 %. The error on $\sin 2\beta$ is given by

$$\delta \sin(2\beta) = \frac{1 + x_d^2}{x_d} \frac{1}{\sqrt{\epsilon D^2 N}} \sqrt{\frac{S+B}{S}}$$

where $x_d/(1+x_d^2) = 0.47$ accounts for the dilution due to the time evolution of the B_d^0. We estimate the effective tagging efficiency ϵD^2 to be 10% (See Section 4.7) and assume $S/B = 10$ which results in a value of $\delta \sin(2\beta)$ of 0.042. We are also studying the possibility of using the e^+e^- decay mode of the J/ψ.

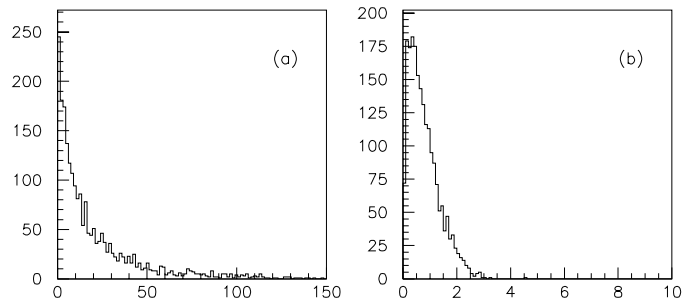

Figure 52: L/σ (a)J/ψ from B decays, (b) J/ψ from primary vertex

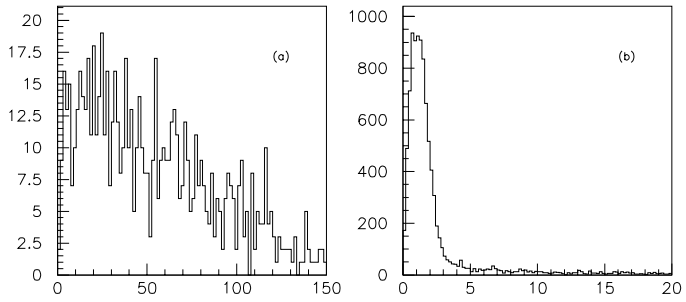

Figure 53: Normalized Impact parameter with respect to the primary vertex of (a) π from real K_s^0 , (b) π from fake K_s^0

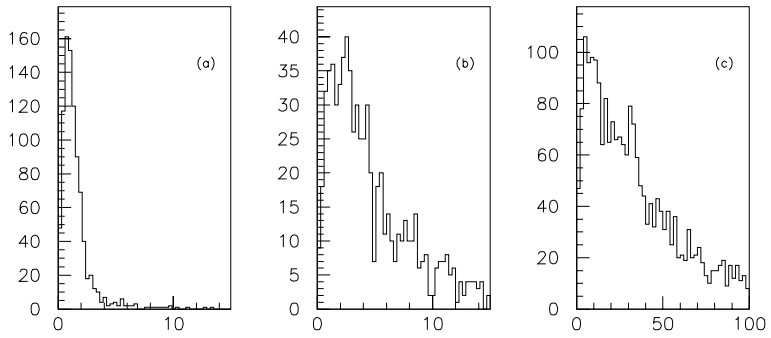

Figure 54: Normalized Impact parameter with respect to J/ψ vertex (a) real K_s from $B \to J/\psi K_s^0$ decay, (b) other real K_s^0's, (c) Fake K_s^0's

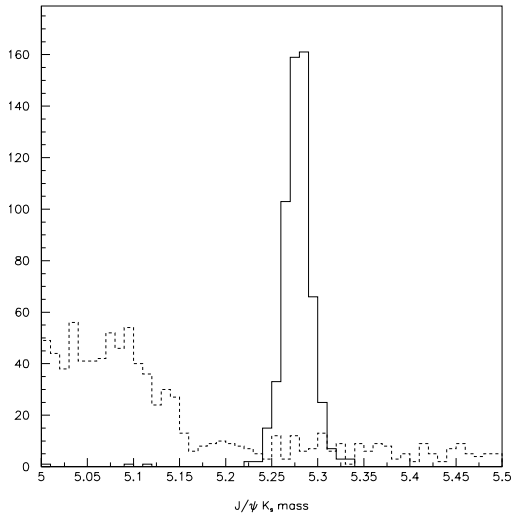

Figure 55: $J/\psi K_s$ mass: the solid line is the signal and the dashed line is background from B decays to $J/\psi X$

Table 17:

Luminosity	$5 \times 10^{31}\text{cm}^{-2}\text{s}^{-1}$
Running time	10^7 sec
Integrated Luminosity	500 pb^{-1}
$\sigma_{b\bar{b}}$	100μb
Number of $B\overline{B}$ events	5×10^{10}
Number of B_d^0's	3.5×10^{10}
BR($B_d^0 \to J/\psi K_s^0$)	5×10^{-4}
BR($J/\psi \to \mu^+\mu^-$)$\times$BR($K_s^0 \to \pi^+\pi^-$)	0.04
Reconstruction efficiency	0.05
Trigger efficiency	0.80
Number of reconstructed $B_d^0 \to J/\psi K_s^0$	2.8×10^4
Tagging efficiency ϵD^2	10%
$\delta\sin(2\beta)$	0.042

In Run I CDF reconstructed 240 $J/\psi K_s^0$ events from 110 pb^{-1} with a signal to background ratio of 1.2 [15]. The increased coverage of the new silicon vertex detector should result in a much improved signal to background.

Their goal for Run II is to reconstruct three to four times as many $J/\psi K_s$ events per pb^{-1} by lowering the p_T threshold of the dimuon trigger to 1.5 GeV/c, improving the coverage for lepton identification and by using $J/\psi \to e^+e^-$ as well as $J/\psi \to \mu^+\mu^-$ decays. They expect to reconstruct $\approx 10,000$ events for 2 fb^{-1} from the dimuon trigger in the central region ($|\eta| < 1$).

CDF conservatively estimate a tagging efficiency ϵD^2 of 3.8% resulting in $\delta\sin(2\beta) = 0.13$. Improvements in tagging by including a Time of Flight system for kaon tagging and the use of dielectron triggers could result in an error on $\sin(2\beta)$ of $\delta\sin(2\beta) = 0.076$ from CDF data after 2 fb^{-1} of integrated luminosity.

4.5 Flavor-changing B meson decays

4.5.1 The Physics Significance of Rare B Meson Decays

Within the Standard Model, flavor-changing neutral current decays of b quarks may occur through loop – or penguin– diagrams or box-diagrams. Such decays, which involve small CKM matrix elements and are therefore rare, may be used to extract CKM matrix elements once various long range and perturbative QCD effects are taken into account. If, however, some of these decays occur at a much higher level than predicted by the Standard Model, this would be evidence that there were new particles whose amplitudes could contribute to the loops or boxes. This would provide a path to new physics which is at a higher mass scale than can be probed directly at existing or planned accelerators. Table 18 [18] gives a list of some interesting rare decays and their estimated branching fractions.

Table 18: Estimated Branching Fractions for Flavor-Changing Neutral Current Decays with Muons and Electrons .

Decay Mode	Est. BR(SM)	Measurements and 90% CL upper limits
$(B_d, B_u) \to X_s \mu^+ \mu^-$	$(5.7 \pm 1.2) \times 10^{-6}$	$< 3.6 \times 10^{-5}$
$(B_d, B_u) \to X_d \mu^+ \mu^-$	$(3.3 \pm 1.9) \times 10^{-7}$	–
$(B_d, B_u) \to K \mu^+ \mu^-$	$(4.0 \pm 1.5) \times 10^{-7}$	$< 0.9 \times 10^{-5}$
$(B_d, B_u) \to K^* \mu^+ \mu^-$	$(1.5 \pm 0.6) \times 10^{-6}$	$< 2.5 \times 10^{-5}$
$B_s \to \mu^+ \mu^-$	$(3.5 \pm 1.0) \times 10^{-9}$	$< 8.4 \times 10^{-6}$
$B_d \to \mu^+ \mu^-$	$(1.5 \pm 0.9) \times 10^{-10}$	$< 1.6 \times 10^{-6}$
$(B_d, B_u) \to X_s e^+ e^-$	$(8.4 \pm 2.2) \times 10^{-6}$	–
$(B_d, B_u) \to X_d e^+ e^-$	$(4.9 \pm 2.9) \times 10^{-7}$	–
$(B_d, B_u) \to K e^+ e^-$	$(5.9 \pm 2.3) \times 10^{-7}$	$< 1.2 \times 10^{-5}$
$(B_d, B_u) \to K^* e^+ e^-$	$(2.3 \pm 0.9) \times 10^{-6}$	$< 1.6 \times 10^{-5}$
$B_s \to e^+ e^-$	$(8.0 \pm 3.5) \times 10^{-14}$	–
$B_d \to e^+ e^-$	$(3.4 \pm 2.3) \times 10^{-15}$	–

4.5.2 Rare Decays in BTeV

Because the Tevatron produces about 10^{11} b-hadrons per year, we should be able to observe some of these decays and to set stringent limits on others. However, b-physics at the Tevatron also has more sources of background than at e^+e^- B-factories and the sensitivity may be limited by the inability to reject these backgrounds.

Below, we show the results of a study of the decay $B^- \to K^- \mu^+ \mu^-$. This decay, according to Table 18, occurs with a branching fraction of around $4.0 \pm 1.5 \times 10^{-7}$. The study is based on simulation runs of 5000 signal events each containing the signal B^- decay and a generic $\bar{b}$-decay and 10^5 background events each of which has both B-mesons decaying semileptonically.

In Fig. 56 we show an invariant mass distribution for $B^- \to K^- \mu^+ \mu^-$ which also includes background events whose origin is described below. The requirements imposed on events contributing to this plot were determined by the need to achieve very high rejection of the background while maintaining reasonable efficiency. They are:

- A primary vertex consisting of at least 2 tracks with a good χ^2 fit;
- A secondary vertex consisting of three tracks:
  1. one of which is a charged kaon and is required to pass through the RICH and have a momentum greater than 4 GeV/c;
  2. another is a positively charged muon which is required to hit the muon detector and have a momentum greater than 5 GeV/c;
  3. and another is a negatively charged muon which is required to hit the muon detector and have a momentum greater than 5 GeV/c.

  The secondary vertex must have a χ^2 less than 8. The normalized separation, L between the primary vertex and the candidate secondary vertex, L/σ_L, must be greater than 7 and the candidate must satisfy a 'pointback' cut with respect to the primary vertex of less than 2.5 standard deviations.

It is also critical to study the background to this state. The various sources of background are:

- Minimum bias events where three particles conspire to fake a secondary vertex and two of the particles either decay downstream of the magnet or make hadronic showers which leave a signal in the muon detector (hadron punchthrough).
- Charm events with one or more real muons and kaons.
- b-events where portions of the two b-hadrons in the event appear to verticize downstream of the production point. In approximately 1% of all $b\bar{b}$ events both B-hadrons decay semileptonically producing two real muons. In addition, there is a charged kaon in at least one of the b's over 90% of the time.
- More generally, any variety of admixture of B, charm, minimum-bias events, primary interactions and secondary decays, combined with hadronic punchthrough.

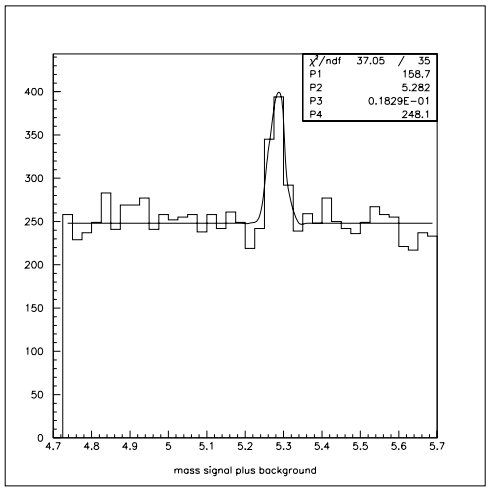

Figure 56: Invariant mass spectrum of $K\mu^+\mu^-$ including an estimate of the background from events where both b's decay semileptonically (also obtained with MCFast).

- Fake events from single b decays such as $B^- \to K^-\pi^+\pi^+$ where both pions fake muon signatures by decay or punchthrough. Another possibility is the decay $B^- \to D^o\pi^-$ where the D vertex is not seen as separated from the B vertex and where both pions simulate muons. However, a mass cut on the D will remove this background.

The basic weapons to combat backgrounds are:

- Excellent mass resolution on the final state.
- Excellent discrimination between the primary and secondary vertex which eliminates backgrounds from the minimum-bias events and from the underlying event within a true b-event.
- Excellent 'pointback' resolution between the reconstructed b candidate and the primary vertex which will do much of the work to reject events that have been artificially pieced together from particles from the two separate b's in the event.
- The ability to reject events where other tracks point to the candidate vertex, where some of the tracks in the candidate vertex also point to the primary, or where some of the tracks in the candidate vertex intersect with other tracks not in the primary vertex (i.e. tracks from the associated b).

In addition, the signal-to-background depends on the quality of both the muon detector and the particle identification.

We did not include the decay $B^- \to \psi K^-$ as a background. That decay is large compared to the rare decay being considered here and will interfere with the rare decay and distort the dimuon mass distribution in the vicinity of 3 GeV/c^2. This, however, is a physics contribution and will certainly be observed and studied based on a mass cut on the dimuon. In fact, this state can be used to calibrate the efficiency of the analysis and can be used as a normalization for a measurement of the relative branching fraction.

We have not simulated all sources of background. Our own estimates indicate that the most serious background is from events with pairs of B's which each undergo semileptonic decays. We have analyzed 10^5 simulated events of this type and have a background in the mass plot (4.7 to 5.7 GeV/c^2) of 1 event in 40 bins (which we can make disappear with only a slight adjustment in cuts). We obviously need to run more background events and are beginning to do so. However, if we scale this result to the correct mass interval and by the correct relative normalization factor, we estimate a background of about 750 events (with a very large error) under a peak of about 300 – or signal to background of 1 to 3 and a statistical significance of 10 standard deviations. We show what this would look like by including this estimated background in Fig. 56. We discuss below how to reduce this background further.

The overall efficiency for this state, with cuts designed to achieve good background rejection, is about 2.5%. Table 19 gives a calculation of the yield obtained in a one year run at a luminosity of $5\times10^{31}\mathrm{cm}^{-2}\mathrm{s}^{-1}$. We include in this calculation a triggering efficiency of 80% for those events which satisfy all the analysis cuts. This is consistent with what we expect to get from the dimuon trigger (70%) 'or-ed' with the vertex trigger which recovers almost half of what the muon trigger failed to accept.

Table 19: Estimate of Yield for $B^\pm \to K^\pm \mu^+ \mu^-$

Quantity	Value
Luminosity	$5 \times 10^{31}\mathrm{cm}^{-2}\mathrm{s}^{-1}$
Running Time/year	10^7s
$b\bar{b}$ cross section	100μb
Total $b\bar{b}$ pairs produced	5×10^{10}
Total $B^\pm$	3.5×10^{10}
Branching fraction	4×10^{-7}
Efficiency (cuts above)	2.5%
Total signal events	350
Events satisfying trigger	300
Estimated background	750
Signal to background	0.4
Statistical significance of observation	$>$ 10 Standard deviations
Uncertainty on branching fraction	10%

There is much work left to be done, especially on understanding and rejecting

the backgrounds. However, we have not exhausted all the weapons we have available to defeat these backgrounds. We have not optimized pointback cuts, χ^2 cuts on the secondary vertex, or the L/σ_L cut. Cuts that we have not yet employed include those which reject the event if there are other tracks that intersect the candidate secondary vertex and which reject the event if the daughter tracks of the candidate point either to the primary vertex or intersect with another track that is not in the primary (presumably from the other b in the event). We have also not investigated kinematic cuts to see if any characteristic of the individual particle p_T's or the dimuon mass distribution, or the angular distributions of the particles in the decay rest frame can help discriminate signal from background. Nevertheless, the initial results are very encouraging.

4.5.3 Comparison with CDF

According to the CDF II Technical Design Report [15], CDF expects a signal of 100-300 $B^+ \to \mu^+\mu^- K^+$ events in collider RUN II. The signal-to-background is expected to be better than the 1 to 10 achieved in RUN I. However, CDF, because of its lack of particle identification, is exposed to background from all the pions in the event conspiring with the muons to create background. In BTeV, because of the RICH, only the kaons can contribute to the background and there are fewer of them. BTeV will have intrinsically lower background than detectors without powerful particle identification. In light of the discussion above, it is reasonable to say BTeV's sensitivity for detecting rare B decays is comparable to or better than CDF's.

4.6 Trigger Simulations

The trigger simulations have been performed using MCFast v2_6 interfaced to the Level 1 trigger simulation software. The trigger software was designed to test the Level 1 vertex algorithm described in the trigger section of Section 2. The simulations take into account the geometry of the vertex detector and the size of the interaction region. The particles are traced through the detector and hits are generated and fed to the trigger simulation. During the tracing step, the particles suffer multiple scattering and energy loss as they step through the material of the vertex detector. There are no delta-rays or secondary interactions in the current simulation.

Station hit reconstruction has been studied for the baseline geometry using a simplified model for hit generation which ignores delta-rays and other detector and digitization effects. In the simulations presented here the vertex detector was divided into 16 slices in ϕ. This approach will facilitate parallelism in the trigger algorithm. The trigger software does pattern recognition on the station hits in each ϕ slice to find tracks. A primary vertex is built from the good tracks that are found. The tracks must have a minimum momentum in the bend plane p_y of 0.5 GeV/c and hits in at least three stations of the vertex detector. The algorithm handles the large ($\sigma_x = \sigma_y = 50\mu$m) beam width and reconstucts the primary vertex in 90% of $B \to \pi\pi$ events.

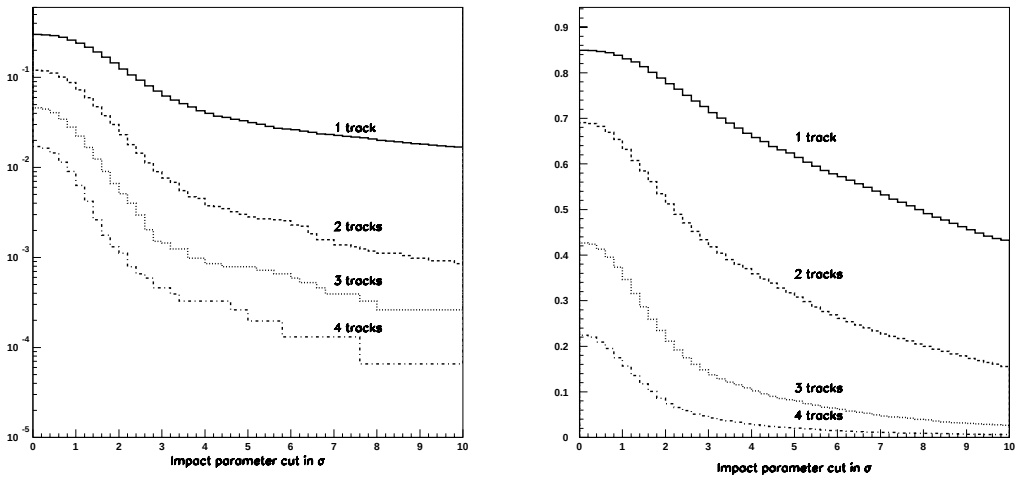

Figure 57: left) Trigger efficiency for light quark events; and right) Trigger efficiency for $B^o \to \pi^+\pi^-$. For the $B^o \to \pi^+\pi^-$ sample, the daughter $\pi^+\pi^-$ tracks are required to be reconstructed in the spectrometer. The ordinate gives the choice of cut value on the number of standard deviations (σ) on the impact parameter of the track relative to the primary vertex.

In the current implementation, the Level I trigger is formed by requiring a minimum number of tracks, N, to have a large impact parameter with respect to the primary vertex. One choses the size of the normalized impact parameter cut, b_{min}, by which these N tracks must miss the primary. In Fig. 57, the Y-axis is the efficiency for the given type of state and the X-axis is b_{min}. Each plot contains four curves, for N=1, 2, 3, and 4. The goal of the trigger is to find a set of selections in N and b_{min} which is very efficient for b-decays and has very poor efficiency for non-b interactions, especially those resulting in final states with light quarks, u, d, and s, which make up most of the total cross section. The plot clearly shows that there are sets of cuts which achieve this goal. For example, the requirement of N=2 and $b_{min} > 4$ results in an efficiency of about 36% for $B^o \to \pi^+\pi^-$ decays that are in our acceptance and rejects 99.6% of all light quark events. With this reduction at Level I, there is sufficient bandwidth to allow the surviving events to be moved to subsequent levels of the trigger so that further reductions can take place based on more complete analysis of the event. With this same requirement, the correlation of triggered events with the events that remain in the data sample after all analysis cuts is very high, or about 72%.

We have also investigated the vertex trigger on modes with a J/ψ. For the mode $B_s \to J/\psi K^*$ the trigger is 35% efficient for events with all four tracks in the acceptance and about 50% efficient for events that survive the reconstruction cuts. The trigger selection requirement for the $J/\psi K^*$ studies was N=3 tracks and $b_{min} > 3$ which exhibits an even better rejection for light quark events than N=2 and $b_{min} > 4$ used in the $B^o \to \pi^+\pi^-$ studies.

Other approaches to the Level I trigger are possible and are being investigated. Some of these are discussed in Section 2 above.

4.7 Tagging

For charged B mesons, the flavor of the heavy quark (b or $\bar{b}$) is determined by the charge of the B mesons. For neutral B mesons (B_d and B_s) the quark flavor can usually be determined from the flavor of the decay products, for example by the charge of the kaon in $B_s \to \psi \bar{K}^*$, $\bar{K}^* \to K^- \pi^+$ decay. These modes can be used to measure $B_s \leftrightarrow \bar{B}_s$ and $B_d \leftrightarrow \bar{B}_d$ oscillations (sensitive to V_{ts} and V_{td} respectively), if the flavor of the b quark at the production point is determined independently. Decays to CP-eigenstates do not identify the b quark flavor. In fact, amplitudes for these decays interfere with the mixing amplitude producing CP-violating effects. Measurements of CP-asymmetry, resulting e.g. in determination of $\sin 2\alpha$ via $B_d \to \pi^+\pi^-$ and of $\sin 2\beta$ via $B_d \to \psi K^0_S$, again require determination of the b quark flavor at the production point - so called "flavor tagging". Since every tagging method sometimes produces false identification, the effectiveness of flavor tagging is characterized by a product $\epsilon\, D^2$ (hereafter called simply "tagging efficiency"), where $\epsilon = (N_R + N_W)/N$, and D is a "dilution" factor, $D = (N_R - N_W)/(N_R + N_W)$ ($N-$number of reconstructed signal events, N_R-number of right flavor tags in this sample, N_W-number of wrong flavor tags). Since the measurements mentioned above are among the most important goals of the BTeV program, large tagging efficiency is a crucial design criterion for the experiment. The forward detector geometry offers unique advantages for flavor tagging over an experiment operating in the central region.

The charge of the pion in $B^{**\pm} \to \pi^\pm B_d$ decays tags the b flavor. This is the "same-side" tagging method. Measurements of the B^{**} production rates will be one of the physics goals at the initial stage of the experiment. CDF measures $\epsilon\, D^2 = (1.5 \pm 0.4)\%$ for their detector and extrapolates to 2.0% for the CDF-II experiment due to improved tracking with SVX-II [15]. We expect to do even better since the slow pion from B^{**} decays will acquire larger momentum in the forward region decreasing the effect of multiple scattering on tracking performance.

The other methods rely on determination of the flavor of the other b quark in the event, since b quarks are always produced in $b\bar{b}$ pairs ("away-side tagging"). The flavor of the other b can be determined from the charge of the lepton emitted in its semileptonic decay, the overall charge of the b jet, and the charge of the kaon produced in the $b \to c \to s$ cascade.

Wrong-sign background from semileptonic charm decays in $b \to c$ cascade is the main limiting factor in tagging efficiency by leptons. Our simulations indicate $\epsilon\, D^2 \approx 1.5\%$ for muon tagging in BTEV, compared to 1% expected in CDF-II.

CDF measures $\epsilon\, D^2 = (1.0 \pm 0.3)\%$ for jet charge tagging, and extrapolates to 3.0% in CDF-II due to improved vertex resolution in SVX-II. We expect to do much better because of superior vertexing capabilities which will help determine which tracks actually belong to the b jet.

Kaon tagging is the most potent method at e^+e^- B factories. Potentially large backgrounds from the underlying event call for excellence in both particle identification and vertex resolution. Both are strong points of our forward

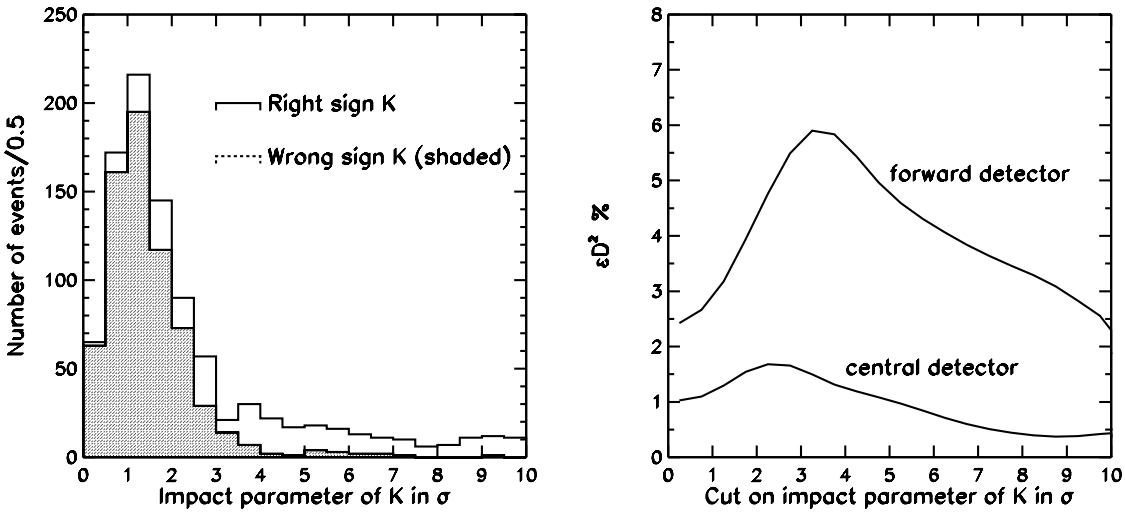

Figure 58:
Left plot: L/σ distribution in BTeV for K impact parameter for right sign (unshaded) and wrong sign (shaded) tags.
Right plot: Kaon tagging efficiency ($\epsilon\, D^2$) as a function of kaon impact parameter cut in units of L/σ. Particle misidentification is neglected. The upper curve respresents BTeV simulation. The lower curve respresents a central detector with a ToF system and vertex detector with SVX-II performance.

detector geometry. As described in the detector design section we are aiming at efficienct kaon identification in the 3-70 GeV/c momentum range. Even with a perfect kaon identification there is a large kaon background from the underlying event which may dilute tagging efficiency. Figure 58 illustrates the importance of a good resolution on the kaon impact parameter at the primary vertex for suppression of this background. In BTeV the tagging efficiency is improved by a large factor when cutting on significance of the impact parameter of the kaon. This figures also illustrates that the impact parameter resolution achievable in a central detector is not sufficient for a large improvement in tagging based on kaon identification. In BTeV, we expect kaon tagging efficiency $\epsilon\, D^2$ in a range of 4.5-6% depending on the exact performance of the particle identification system, especially if the K/p separation extends to the lowest kaon momenta. The baseline CDF-II detector does not include a particle identification device. Our simulation of an excellent ToF system (100 ps resolution) in the central region ($|\eta| < 1$) together with a vertex detector with the SVX-II performance shows that $\epsilon\, D^2$ in such a system would be $< 1.5\%$

4.8 Comparison of BTeV with Central Detectors

In this section the proposed BTeV detector will be compared with the Run II central detectors. The comparison will focus on the physics reach of the experimental programs but will also illustrate the intermediate quantities, such as decay length and decay time resolution, particle ID and trigger efficiency, which contribute to that reach. In all of the quantities compared, the BTeV detector is found to be at least competitive with the central detectors and, in several critical areas BTeV is found to be superior. Those areas in which BTeV is superior are:

- The combination of the B production dynamics and the closeness of the pixel detectors to the beamline results in L/σ_L distributions which favour BTeV. This improved decay length significance allows BTeV to be much more efficient for a given background rejection power.
- The BTeV triggering strategy is more efficient for most signal channels. D0 does not plan to have a vertex/impact parameter trigger. CDF does plan to have an impact parameter trigger but only in Level 2, not in Level 1. Moreover this trigger has a higher p_T threshold than is planned for BTeV.
- BTeV includes a RICH detector which has both a spatial acceptance and momentum acceptance which is well matched to the physics demands of the experiment. Even with the TOF upgrade, the CDF detector will have a weaker particle ID system.
- The resolution on proper decay time is much better in BTeV than in the central detectors. This allows an x_s reach of beyond 40 whereas the central detectors are limited to x_s of about 20.

One of simulations discussed in this EOI was a measurement of $\sin(2\alpha)$ using $B_d \to \pi^+\pi^-$. See section 4.3. With the usual caveats about Penguin pollution, BTeV can acheive $\delta(\sin(2\alpha)) = 0.10$ in one year of running. This is a reach equal to that projected by CDF in two years of running at a four times greater luminosity. In order to acheive this performance, the BTeV detector was able to exploit all of the first three points discussed above.

Another simulation discussed here was the measurement of $\sin(2\beta)$ using $B_d \to \psi K^0_S$. See section 4.4. While it is certain that BTeV will be a second generation experiment for CP violation in this mode, a significant improvement in the measurement is expected: the one year reach of BTeV is three times better than the two year reach of CDF. Table 20 gives an overview of many kinematic properties and how they differ between BTeV and CDF.

In both of the preceding analyses, a critical part of the work is the tagging of the flavor of the initial state. Table 21 summarizes the projections made by CDF and BTeV regarding their respective effective tagging efficiencies. The BTeV effective tagging efficiency is expected to exceed that of CDF by as much as 25%. More importantly, most of the improvement comes in a mode with a low mistag

Table 20: Comparison of B kinematics and of B reconstruction properties between BTeV and a central detector, for $B_d^0 \to J/\psi K_s$. The leftmost of the two BTeV columns gives values which are computed when all four tracks in the final state have been reconstructed by the BTeV detector. The rightmost column gives the same quantities with the additional requirement that the muons penetrate through the fiducial volume of the muon detector. The quantities in the central detector column were computed using an MCFast simulation of a detector which was modelled on the CDF Run II detector [15]. Except for the quoted resolutions, all quantities in the table are median values, not mean values.

	Central Detector	BTeV 4 Tracks recon.	BTeV muons identified
B			
$\beta\gamma$	1.28	8.8	12.8
$\beta\gamma\ c\tau$	$\approx$ 0.4mm	$\approx$ 2.8mm	$\approx$ 4.3mm
Mass resolution	14 MeV/c^2	16 MeV/c^2	13 MeV/c^2
p_B	6.7 GeV/c	48 GeV/c	67 GeV/c
K_s			
p_π	1.25 GeV/c	4.3 GeV/c	
Mass resolution	2.7 MeV/c^2	2.5 MeV/c^2	
J/ψ			
p_μ	2.75 GeV/c	10 GeV/c	16 GeV/c
Mass Resolution	9.5 MeV/c^2	9.5 MeV/c^2	9.5 MeV/c^2
μ transverse Impact parameter resolution	30μm	25μm	
L/σ_L	4.5		17
Tags			
p_{Ktag}	1.4 GeV/c	5.0 GeV/c	
$p_{\mu tag}$	2.1 GeV/c	7.5 GeV/c	8.5 GeV/c

Table 21: Comparison of BTeV and CDF flavor tagging capabilities. The first four lines refer to opposite side tagging techniques. The BTeV estimate for electrons is in progress. Also, because BTeV has not yet made an estimate of its overlap factor, the CDF estimate is used for both detectors. The + signs indicate that BTeV has simply taken the CDF projection as a baseline value and argues that some improvement will come as a result of its superior vertexing capabilities.

Tagging Method	ϵD^2 (%)	
	CDF[15]	BTeV[Section 4.7]
Muon	1.0	1.5
Electron	0.7	-
Jet Charge	3.0	3.0+
Kaon	3.0	4.5 to 6.0
Same Side π	2.0	2.0+
Overlap Factor	0.80	
Total	7.8	8.8 to 10.0

probability — in BTeV, kaon tagging has an extremely low mistag fraction, of around 15%. While the mixing or CP violation reach of an experiment depends only on the product ϵD^2, a mode with a low mistag probability is more robust against poorer than expected performance.

But the RICH detector is not just a tagging device. It is a a powerful tool for the reduction of combinatoric background for all modes containing kaons. For example, in the search for $B^+ \to K^+\mu^+\mu^-$, BTeV projects having much smaller backgrounds. See section 4.5.

Penultimately, the BTeV trigger will also be reasonably efficient for many charm decay modes and, as discussed in section 4.10, BTeV forsees a rich charm physics program. Neither of the central detectors envisage a triggering strategy which will allow them to compete in this field.

While the B physics discussed in this EOI is dependent on a good vertex detector, the resolution of the BTeV pixel detector far exceeds what is required for most of the BTeV physics program. However there are two measurements for which superb lifetime resolution is important. These are the measurement of the B_s mixing parameter, x_s, and the measurement of time dependent CP violating asymmetries in the B_s sector. Table 22 gives a comparison of the proper lifetime resolution for various B_s modes which have been investigated by BTeV and CDF.

The mini-Monte Carlo studies described in section 4.2 showed that, in two years of running, all values of x_s less than about 40 are within the reach of BTeV. The same mini-Monte Carlo was used to estimate the two year x_s reach of the CDF II detector given the time resolution and the yield estimates given in their TDR [15]. The result is that their x_s reach using fullly reconstructed B_s decays is limited to about $x_s = 20$. As descibed in section 4.2, their x_s limit

Table 22: Comparison of B_s lifetime resolution. The CDF number comes from [15] in which they give a resolution of 30 μm. It is converted here to a time using an estimate of the β, which is appropriate for B mesons which pass the CDF trigger and analysis cuts.

Detector	Mode	σ_t (fs)
BTeV	$B_s \to \psi K^{*0}$	45
	$B_s \to D_s^- \pi^+ \pi^+ \pi^-$	65
CDF	All fully reconstructed modes	$90^\ddagger$

is reached when the fluctuations in the negative log likelihood function produce secondary mimima which poorly separated from the global minimum. A large part of this limitation comes from their poorer time resolution.

In summary, BTeV is competitive with the central dectectors in all areas considered and it is superior in several important areas.

4.9 Charm Physics with the BTeV Detector

Searches for mixing, CP violation, and rare and standard model forbidden decays in the charm sector (as discussed in section 1) provide a sensitive and possibly unique window to physics beyond the standard model. At a luminosity of $5 \times 10^{31}\mathrm{cm}^{-2}\mathrm{s}^{-1}$ the Tevatron produces on the order of 5×10^{11} charm quark pairs ($c\bar{c}$) a year (although the $c\bar{c}$ cross section at $\sqrt{s}$=2 TeV is not well known, a relatively conservative estimate for it is 1 mb). Such a sample represents an opportunity unavailable anywhere except at hadron colliders, although this potential has yet to be tapped.

Charm physics simulation studies are not as advanced as the beauty studies presented previously in this section. In addition, no effort has yet been made to optimize triggers for charm modes. These studies are beginning now.

As a first step in studying charm physics in collider mode, we have computed the geometrical and tracking acceptances of the baseline BTeV detector (see section 2) for several charm meson decay modes using the MCFast package. We are interested in: (i) the inclusive acceptance (or "single charm"), which refers to the probability to detect all daughters of a charmed or anti-charmed meson, and (ii) the "associated" acceptance, defined as the probability to detect both secondary (charm and anti-charm) vertices.

At the current time we have only considered all-charged final states such as $D \rightarrow K^- + n\pi$ and $D^0 \rightarrow K^+K^-$. The recoiling anti-charmed (or charmed) hadron decays according to PDG branching ratio values. The QQ package has been used to simulate these decays. To define our acceptance, we require that each daughter in a decay leave a minimum number of hits in the spectrometer, which directly reflects our ability to reconstruct the corresponding tracks. To be considered "accepted", a track must produce at least 4 hits in the vertex detector (which implies that it must pass through at least two stations) and 6 hits in the forward tracker. With this criterion our D mass resolution will be 7 MeV/c^2 or better.

The inclusive acceptance for $D^0 \rightarrow K^-\pi^+$, $D^+ \rightarrow K^-\pi^+\pi^+$ and $D^0 \rightarrow K^-\pi^+\pi^-\pi^+$ is 24%, 15%, and 11%, respectively. While the acceptance does depend on decay multiplicity, it does not depend strongly on the strangeness content of the daughter tracks (e.g., kaons vs pions), so the acceptance for Cabbibo suppressed decays is similar to that for Cabbibo favored ones of equal multiplicity. The acceptance for $D^{*+} \rightarrow D^0\pi^+$, $D^0 \rightarrow K^-\pi^+, K^-\pi^+\pi^-\pi^+$ is noticeably lower than the acceptance for final states of the same multiplicity, due to the much softer momentum of the "bachelor" pion from the D^{*+} decay. This can be mitigated by removing the requirement that this pion reach the forward tracker system. The resolution in $\Delta M = M(D^*) - M(D^0)$ deteriorates due to the diminished momentum resolution for bachelor pions not tracked in the forward tracker (see Fig. 59). The acceptance for these decays is approximately 17%

The associated acceptance is defined to be the probability that one decay vertex is fully reconstructed and the second decay vertex is at least partially reconstructed. To calculate this acceptance we again use Monte Carlo events

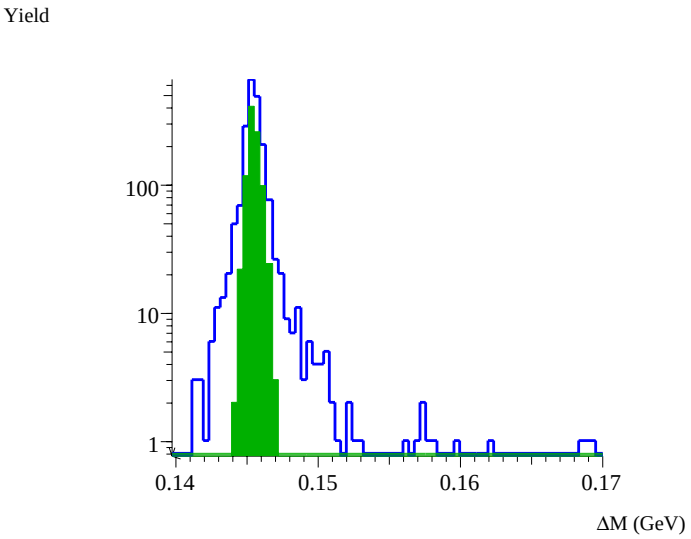

Figure 59: The $\Delta M = M(D^*) - M(D^0)$ mass plot, as estimated by the MC-Fast package, for the baseline detector, where the D^0 decays to $K^-\pi^+$ and $K^-\pi^+\pi^-\pi^+$ (with relative branching ratios according to PDG values). The solid shaded histogram refers to the case where the soft pion from the D^* decays is detected by the forward spectrometer, while the solid line histogram refers to the case where this soft pion is detected only by the pixel detector.

where one daughter decays to all-charged tracks, and the other daughter decays according to PDG branching ratios. We then require that the all-charged track mode be fully reconstructed (just as in the inclusive calculation above). The other charm decay must have at least two tracks reconstructed. These tracks are required to leave at least 9 hits in the vertex and forward trackers. The acceptances for the $K^-\pi^+$, $K^-\pi^+\pi^+$ and $K^-\pi^+\pi^+$ modes are 15%, 12% and 5%, respectively. These acceptances are typically an order of magnitude higher than those observed in fixed target experiments, simply because of the strong kinematical correlation between the $c\bar{c}$ pair (if the charm meson is boosted into one of the arms of the spectrometer, it is likely that the anti-charm also gets a similar boost and is observed in the same arm). One of the benefits is cleaner primary vertices than in a fixed target configuration.

4.9.1 Direct CP Violation in the Charm Sector

In order to estimate the sensitivity of the BTeV spectrometer for a possible observation of Direct CP violation in the charm sector, we have studied in more detail the acceptance and background rejection capabilities for a specific Cabbibo suppressed decay mode: $D^*(2010)^+ \rightarrow D^0\pi^+$, $D^0 \rightarrow K^+K^-$. The geometrical acceptance of the vertexing and tracking systems has already been

presented in the previous subsection. Now, we concentrate on vertexing cuts, overall sensitivity and systematic errors.

Following the constrained vertex reconstruction algorithm, used by the experiment E687 [6] [19], K^+K^- tracks with a relatively large invariant mass are first selected in the event. These are MCFast "offline tracks", i.e. simulated reconstruction tracks for which we have a covariance matrix allowing us to compute a vertex error and χ^2. Note that such tracks are not the outcome of a full pattern recognition package in the forward tracker and the pixels. However, based on studies done for the pixel-based trigger, we know that the level of confusion in this vertex detector is not likely to be a limitation, thanks to its high granularity.

In addition to a minor vertex quality cut on the D^0 candidate vertex, the charged kaons are required to be positively identified as such by the Cerenkov system. We have assumed 97.5% percent positive identification for momenta between 3 and 70 GeV/c and no identification outside this range. Under these conditions, the effective D^0 acceptance is 17.4% (the tracking acceptance for this final state is 25%).

The soft pions from the D^* decays are not required to be reconstructed by the forward tracker and are mostly reconstructed by the vertex detector. At least six hits are required on this soft pion track. No particle identification (P.I.D.) is required. The final tracking and P.I.D. acceptance for the fully reconstructed final state $D^* \rightarrow D^0\pi^+$, $D^0 \rightarrow K^+K^-$ is 11%. The primary vertex is reconstructed with great efficiency independent of the D^0 vertex, due to the relatively large multiplicity in these events (on average, the multiplicity in this reconstructed primary vertex is about 12). The last cut applied in this simple analysis is the usual detachment between the primary and secondary vertices, L/σ_L. The distribution of this quantity for the generated $D^0 \rightarrow K^+K^-$ decay vertices is shown in Fig. 60, and gives us a final acceptance of 4.8%, 3.0%, 1.1% and 0.2% cutting at $L/\sigma_L > 3$, 5, 10 and 20 respectively.

We assume that the dominant background comes from charm. The K^+K^- mass plot corresponding to 100,000 generated charm events is shown in Fig. 61, cutting at moderate values of L/σ_L. The observed signal to noise is acceptable at this stage, and should improve after imposing the following vertex cuts:

- A tighter χ^2 cut on the secondary vertex
- A "point back" cut, requiring that the D^0 track points back to the primary vertex, or conversely, that the distance of closest approach (DCA) to this primary vertex vanishes within measurement errors.
- The K^- and K^+ tracks should not point back to the primary.
- Isolation cut: Since the D^0 decay we are attempting to detect is fully reconstructed, no other tracks should have a significant DCA with respect to this D^0 vertex.

[6] A Charm photoproduction experiment which ran at Fermilab, 1987-1991

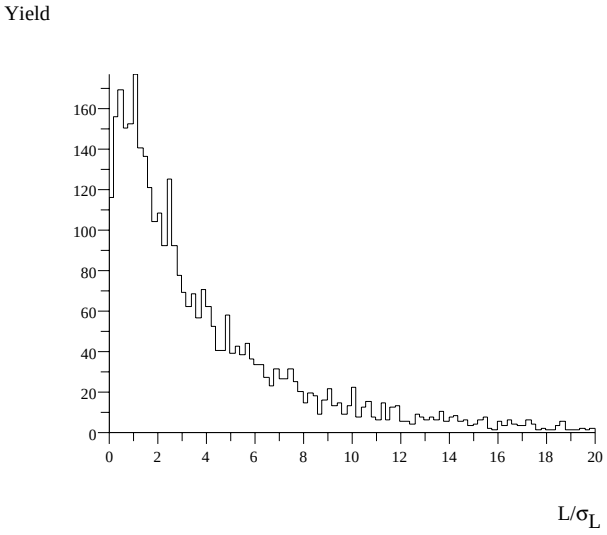

Figure 60: The L/σ_L distribution for the generated $D^0 \to K^+K^-$

- If another secondary vertex is found, make sure that K^+K^- tracks forming the D^0 vertex do not point back to that secondary vertex.

All these cuts have been used in one form or an other by various fixed target experiments for this decay mode and many others.

An effective acceptance of 0.5% could be obtained with acceptable signal to noise. This includes a trigger efficiency of 30% (we hope the trigger efficiency would be better than this). Assuming a total charm D* cross section of 1 mb, BTeV will produce and detect about 7 million such decays in 10^7 seconds running at a luminosity of $5 \times 10^{31}\mathrm{cm}^{-2}\mathrm{s}^{-1}$. In principle, this will give us a statistical error of roughly 5×10^{-4} on a D^{*+} / D^{*-} asymmetry.

We believe a similar level of sensitivity is possible in searches for direct CP violation in D^+ decays as well. Although there is no D^* tag to reduce backgrounds, the longer lifetime of the D^+ allows harder L/σ_L cuts, and you get back the efficiency lost by requiring the bachelor pion to be found.

However, such a proposed improvement in statistical accuracy is meaningless if systematic errors are not seriously taken into account. In photoproduction, the systematic errors were as big as the statistical ones, and were primarily due to uncertainties in estimating the effective acceptance versus true lifetime and to background subtraction. Such uncertainties originate in poorly defined primary vertices, a problem we hope to resolve in a collider environment where the clean track multiplicity is higher. In photoproduction a dominant source of background is secondary interactions in the target, which is not a problem at the collider.

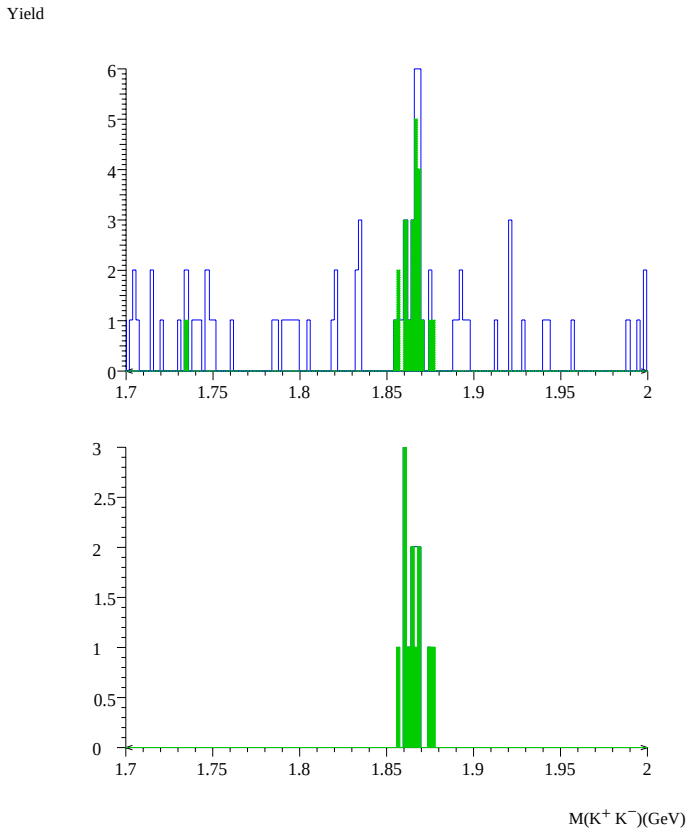

Figure 61: The K^+K^- invariant mass distribution from 100,000 generic Charm events, where the filled histogram contains the signal $D^* \to D^0\pi$, $D^0 \to K^+K^-$ (charge conjugation implied), while the open histogram contains all recorded events in the sample. A $|M(D^*) - M(D^0) - 0.1456| < 2$ MeV cut is imposed. In the top (bottom) plot a requirement of $L/\sigma_L > 0$ ($L/\sigma_L > 3$) is made.

4.10 Charm physics with a wire target

We anticipate that we will be able to run with a wire target before we are able to run in collider mode at C0. This will allow us to take data for charm physics at an earlier date, before the full BTeV detector is ready to install. The charm physics program with the full BTeV detector is discussed in Section 4.9; here we discuss the physics potential of the partially instrumented detector. We consider a thin target in the halo of the proton beam and a vertex detector of some combination of pixel and microstrip planes, covering the same downstream geometrical acceptance as the final detector. Although the full BTeV trigger may not be available at this time, we discuss a possible trigger for this mode of running.

4.10.1 Target and interaction rate

As discussed by Marriner [22], a thin target in the beam halo will intercept beam particles that have large horizontal betatron amplitudes. Such particles will pass through the target a number of times, suffering multiple coulomb scattering until they either have a nuclear interaction in the target, or are scattered so far that they are intercepted at an aperture limit of the accelerator. This analysis suggests it is advantageous to have a low-Z material for the target, eg beryllium or carbon. The interaction rate is then determined not by the thickness of the target, but by the rate at which particles leave the circulating beam. Marriner estimates an interaction rate on the order of $10^5\,\mathrm{s}^{-1}$. This is likely to be a lower limit, which could be increased by a factor of 10 or more if low β is available in C0 at the start of Run II. We propose further study of these considerations jointly with the Beams Division.

4.10.2 Vertex detector and trigger

An advantage of fixed-target mode is that the z-coordinate of the primary interaction is localized to the target. Thus the vertex detector only needs to cover about half the length that it needs in collider mode. The steps of the trigger which find where the interaction took place are also simplified. The algorithms of the full trigger can be tested on a reduced inventory of processors.

We have been studying a simplified trigger based on p_T of the tracks for use in this part of the charm program. It has been established that this is a powerful signal for charm in fixed-target interactions [23], and this is confirmed in our simulations using Pythia and MCFast. It has the following advantages in the early stages of the evolution of the detector and trigger:

- The overall interaction rate may initially be lower than in collider mode, so the requirements on performance of the trigger are reduced, since a more modest rejection is acceptable at Level I.
- Charm hadron mean lifetimes are shorter than B hadrons, so a p_T trigger will be more efficient than a vertex trigger.

- $D^* \rightarrow D\pi$ can be isolated without strong vertexing cuts offline, so it is advantageous not to impose these at the trigger stage.
- Tests of vertexing software can be made on relatively unbiased samples.

We have studied two versions of a p_T trigger: (1) using the track with the highest $|p_T|$ in the event, and (2) using the sum of $|p_T|$ for all reconstructed charged tracks. Each of these can give some rejection of background, but a combination of the two measurements can give an enhanced rejection. For example, a trigger efficiency of 60% for charm can be achieved with a rejection on the order of 10, as shown in figure 62.

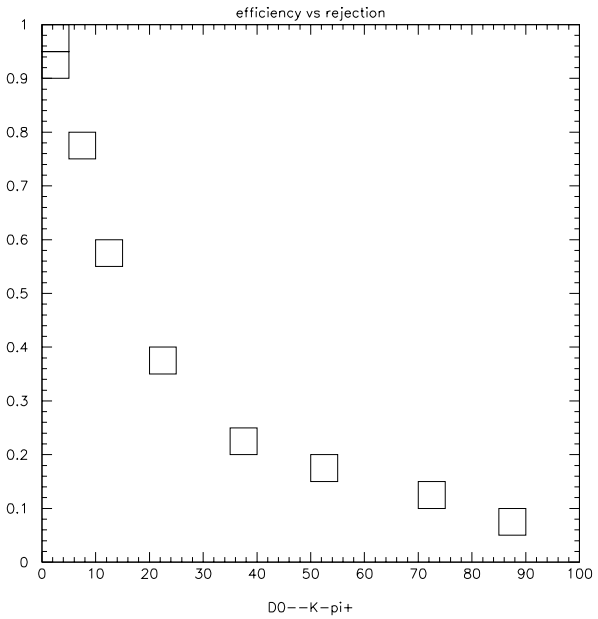

Figure 62: Trigger efficiency for $D^0 \rightarrow K^-\pi^+$ vs non-charm background rejection factor.

4.10.3 Particle ID

It is unlikely that the final BTeV RICH will be available at the start of wire target running. We are investigating the availability and suitability of existing Cherenkov detectors for use in this phase. Such a detector will need to be modified to allow the beam pipe to run through it. The SELEX RICH counter would be a very suitable choice, but the modifications may not be possible or desirable. We are therefore studying the possible use of the threshold Cherenkov detector(s) from the Fermilab E831 experiment.

4.10.4 Reconstruction

Work is continuing on the definition of appropriate analysis cuts and the likely reconstruction efficiency for triggered events: preliminary results suggest this will be on the order of 20% for the more abundant modes. We compare this with the experience of E791, where similar values were achieved.

4.10.5 Physics reach

As an example of the potential of this mode of running, we present an estimate of the annual yield of $D^0 \to K^-\pi^+$ events which could be achieved (Table 23).

Table 23: BTeV/C0 Summary of parameters for wire target running

Property	Value	Comment
Interaction rate	$10^5 - 10^6\,\mathrm{s}^{-1}$	thin C target
Charm cross-section	25μb/nucleon	2×10^{-3} of total for $A = 12$
Charm rate	$200 - 2000\,\mathrm{s}^{-1}$	
Geometrical acceptances:		
$D^0 \to K^-\pi^+$	74%	loss mostly in beam gap
$D^{*+} \to D^0\pi^+ \to K^-\pi^+\pi^+$	61%	
Fraction of total charm which produces accepted $D^0 \to K^-\pi^+$	3.5%	including $\overline{D^0} \to K^+\pi^-$
Trigger efficiency for $D^0 \to K^-\pi^+$	60%	for accepted events
Background rejection	$\times 10$	
Level I trigger rate	$10^4 - 10^5\,\mathrm{s}^{-1}$	
Number of triggered $D^0 \to K^-\pi^+$ events	$3 - 30\,\mathrm{s}^{-1}$	
Offline reconstruction efficiency	20%	
Estimated number of reconstructed $D^0 \to K^-\pi^+$	$10^7 - 10^8$	per 10^7 sec

4.11 Simulation Work Plan

The simulation work has just begun for BTeV. The baseline detector has been modeled and extensively studied. More physics channels will be investigated, but much of the work will be in modeling the details of the detector elements and understanding more complex issues and detector dependent issues such as pattern recognition and trigger rates.

The physics simulations have been based on smeared four vectors. While it takes into account the effects of multiple coulomb scattering and detector resolution, it does not account for many other detector related effects or for processes such as secondary interactions. We will begin more sophisticated modeling of hits in the detector elements. Pattern recognition studies will be completed within the next year.

The trigger simulation includes pattern recognition in tracking the charged particles through the silicon detector. More detailed hit generation and digitization will be required to advance the trigger simulations to more fully understand the efficiencies. We also plan to investigate other trigger algorithms as part of the trigger R&D effort. Further simulations will be required to fully understand the effects of multiple interactions on the tracking and vertexing efficiencies. The tools are already in place to do most of this work.

Detailed simulations of the expected background rates in the C0 hall have not yet been performed. In order to understand the expected backgrounds at C0, four types of beam backgrounds will be studied:

- Backgrounds originating from the halo particles in the final triplet of quadrupoles upstream of the interaction point
- Backgrounds from $\bar{p}p$ collisions
- Backgrounds from halo particles passing through the detectors
- Backgrounds from inelastic beam-gas interactions

There are tools available to study the beam backgrounds [24]. Proton-antiproton collisions are typically simulated with DTUJET93. Beam halo interactions with scrapers and particle tracking through the Tevatron are modeled with STRUCT. Particle loss induced hadronic and electromagnetic showers, and secondary particle transport in accelerator and detector components, including shielding, are simulated using the MARS simulation package. We expect to carry out studies of the beam related backgrounds in cooperation with the Beams Division as the design of the detector and interaction region move ahead.

Other work must be done to complete the tool kit for the simulation effort. We plan to integrate the simulation software for particle identification into the simulation package. We are also improving the global tracing package and will add a Kalman filter to the package. Details of these plans are given in Ref. [24].

Further study of the electromagnetic calorimeter options is required. The fast simulation code that already exists inside MCFast will be very useful to study the reconstruction of electrons and photons in a variety of calorimetry

options. In addition, many more physics studies will be done in the coming months. One example is the investigation of the CP reach for the angle γ. There are several approaches to this measurement, one of which is described in Section 1.

The simulation tools are now in place to study the physics and detector issues that need to be addressed to make the next refinement of the BTeV detector. Over the next year, we expect to investigate a wide variety of physics topics connected with bottom and charm physics and improve the background studies in part by including more "real world" effects. We believe from the studies presented here that the BTeV detector with its superb vertex reconstruction capability, vertex trigger and outstanding particle identification can easily surpass existing central detectors in a variety of physics topics including B_s mixing, CP violation involving B_s decays, rare B decays, as well as all charm studies.

References

[1] H. U. Bengtsson and T. Sjostrand, Comput. Phys. Comun. **46**,43 (1987).

[2] QQ is developed and maintained by the CLEO Collaboration. For the studies reported here, it is used for its model of the decays of hadrons containing heavy flavors.

[3] P. Avery et al, "MCFast: A Fast Simulation Package for Detector Design Studies". in the Proceedings of the International Conference on Computing in High Energy Physics, Berlin, (1997) and http://fnpspa.fnal.gov/mcfast/mcfast_docs.html

[4] P. Billoir, NIM **225**, 352-366 (1984).

[5] Paul Avery http://www.phys.ufl.edu/~avery/fitting.html, Fitting Theory V.

[6] G. Marchesini and B.R. Webber, Nucl. Phys. **B310**, 461 (1988); Nucl. Phys. **B330**, 261 (1988);
I. G. Knowles, Nucl. Phys. **B310**, 571 (1988);
G. Abbiendi, *et al.*, Comp. Phys. Comm. **67**, 465 (1992).

[7] F. Paige and S. Protopopescu, Brookhaven National Laboratory Report BNL-37066(1985)(unpublished).

[8] P. McBride and S. Stone, Nucl.Instrum.Meth. **A**368(1995) 38-40.

[9] F. Abe et al., The CDF Collaboration, Phys. Rev. **D54**, 6596 (1996). FERMILAB-PUB-96/119-E.

[10] R. Kutschke, BTeV Internal Note, 97/9, June 1997.

[11] K.T. McDonald, "Maximum Likelihood Analysis of CP Violating Asymmetries", PRINCETON-HEP-92-04, Sep 1992. 12pp, unpublished.

[12] K. Sterner and W. Selove, Univ. of Pa. Report UPR-237E, May 1997.)

[13] O.R. Long, *et al.*, "Monte Carlo Simulation of $B_d^0 \to \pi^+\pi^-$ from pp Interactions at $\sqrt{s}$ = 40 TeV", UPR/216E, PRINCETON/HEP/92-07, SSCL/PP/139 (1992).

[14] J. Alexander, talk presented at the Hawaii Conference on B Physics and CP Violation, March 1997.

[15] " The CDF II Detector Technical Design Report", CDF collaboration, FERMILAB-Pub-96/390-E (1996).

[16] M. Procario, BTeV Internal Note, 97/10, June 1997.

[17] "J/ψ and $\psi(2S)$ Production in $p\overline{p}$ Collisions at $\sqrt{s}$ = 1.8 TeV", CDF Collaboration, FERMILAB-PUB-97/024-E.

[18] A. Ali, "Rare B Decays in the Standard Model", *Beauty '96*, North Holland Press, 1996, the Netherlands, Table 1, page 13 and references therein.

[19] P.L. Frabetti *et al.*, *Nucl. Instrum. Methods.* **A 320**, 519 (1992).

[20] P.L. Frabetti *et al.*, *Phys. Lett.* **B 323**, 459 (1994).

[21] E. Aitala *et al.*, *Phys. Lett.* **B 371**, 157 (1996).

[22] J.Marriner, "Operation of the C0 experimental region with a fixed (internal) target", April 1997, unpublished.

[23] D.C.Christian, "Triggers for a high-sensitivity charm experiment", in proceedings of CHARM2000 workshop, Fermilab-conf-94/190 (1994).

[24] From the C0 Workshop, Fermilab, Dec 4-6, 1996. See http://fnphyx-www.fnal.gov/conferences/czero/simulations_summary.html

[25] E. Blucher et al, in "Proceedings of the Workshop on B Physics at Hadron Accelerators", Snowmass, Colorado, June 21-July 2, 1993, eds. P. McBride and C.S. Mishra, p.309.

5 BTeV R&D Program

The program described above can only be realized by a very powerful detector which has:

- an excellent high-resolution vertex detector;
- a state-of-the-art triggering and data acquisition system;
- superb charged particle identification;
- excellent electromagnetic calorimetry; and
- outstanding muon detection.

The baseline detector described in section 2 addresses these requirements. In order to realize these systems, a substantial program of research and development is necessary. Some of the work involves R&D because there are no examples of successful solutions in HEP. Others involve systems for which there are working examples in other experiments. Even these will require development if they are to meet the specific requirements of this experiment.

In particular, there are two systems which need R&D work. The vertex detector is based on silicon pixel detectors. It must operate at high rate and must be able to send its data without deadtime to the Level I trigger. It must operate in a hostile radiation environment. A program of R&D to create such a detector is set out below. Since BTeV wants to address a wide range of physics topics which are at a relatively low P_t scale, it must have a relatively unbiased Level I trigger. In section 2, we described a massively parallel, pipelined Level I trigger which moves large quantities of data through a system consisting of thousands of processors. The program of studies, investigations, and prototyping needed to develop such a system is also described below.

Another challenge in the area of particle identification is how to best cover the very low momentum region of the particle spectrum which is simply ignored in the baseline. Many of the kaons that can be used to tag the flavor of the 'signal' B have momentum of between 1 and 3 GeV/c. BTeV would like to be able to identify these particles as kaons but that would require a second particle identification detector based on a different technology. While there are some promising possibilities, we believe that R&D will be needed for this system.

The other detectors need significant development efforts. We have chosen to use a gas Ring Imaging Cerenkov Counter (RICH). Work needs to be done to chose the optimal gas, materials, optics, and photosensors. Effort is needed to design a detector which will fit into the very small space available for it in C0. Similarly, the muon system and the electromagnetic calorimeter need a lot of effort to satisfy the rate, resolution, and space requirements of the experiment.

In addition to R&D to develop the technologies described above, there is also need for R&D into alternatives or systems that are not in the baseline design but could extend the capabilities of the detector. In particular, diamond pixel detectors, which are under development in various places in the world, offer an attractive alternative to silicon pixel detectors.

5.1 Pixel System R&D

At the heart of the BTeV experiment is a very sophisticated tracking system based on pixel detectors that will provide high resolution vertex information and will be the central component of the Level I trigger, providing it with fast and precise vertex information. This system will require an aggressive R&D effort in several respects. The proposed pixel size (30×300 μm^2) poses a great challenge to state of the art bump bonding techniques in order to achieve adequate yields in the hybrid detectors. Furthermore the goal of minimizing the material budget will require great effort in optimizing the thickness of the sensor and readout electronics. In addition, it will require the design of a low mass cooling system and support structure. Finally the goal of including the pixel information in the Level I trigger requires an intense R&D effort in the pixel readout architecture and data flow out of individual pixel and real time tracking processors. Much of the development required can be done in conjunction with the efforts for ATLAS, CMS, and TeV33. Nevertheless, the specific requirements for BTeV will require R&D beyond these solutions.

The following sequence of R&D for the pixel system is only an outline of issues that need to be addressed and solved in order to allow final system engineering to be done. The nearer-term stages are more clearly understood at this time, and fleshed out in more detail. It should be understood that these stages already require significant engineering effort. The amount of engineering and funding must build up in the subsequent stages, briefly sketched in the present report.

5.1.1 Fall 97: Components and process development/testing

The radiation hardness requirements are beyond presently achieved technologies. This is because we need to use detectors after "type-inversion", and therefore we will need to replace the conventional p-side readout with n-side readout. Thus, we will collect electrons instead of holes, changing the polarity of the front-end amplifier. In addition, there need to be "p-stops" between adjacent n-type pixels to prevent shorting the elements out. This takes space, limiting the achievable pitch. The need for other guard rings must be understood and incorporated into the detector design.

The crossing time of not less than 132 nsec allows development of lower power and/or lower noise front-end amplifiers than those needed for LHC. However, the need to have pixel data available for Level I triggering adds requirements to the on-chip data handling and for the overall system architecture. Components need to be developed in ASICs for eventual integration into a single chip consistent with the overall architecture.

The bump-bonding of 30 μm pitch devices is also a challenge. Vendors capable and willing to work on our scale of development and eventual system must be identified and a collaborative effort must be started. The possibility of using specially thinned silicon parts will permit optimizing the detector geometry with less multiple scattering burden. The implications for reliable bonding of

detectors and readout chips with thinned parts must be explored, and again vendors found. The possibility of using large detectors with multiple readout chips bump bonded should be explored. We will need bench tests, beam tests, and radiation hardness exposures at this stage.

5.1.2 Fall 98: System architecture and additional components testing

Some iteration of the initial plans will be required as various parts in the first stage of R&D are successfully completed. The system will need to achieve a balance of performance, reliability (including parts assembly yield) and cost. At this stage, the total system design starts to play a role. The trade-offs among heat load, support mechanisms, cooling technology, detector-readout component thickness/rigidity need to be addressed. In addition, the structures needed for rf shielding and moving the detectors in and out of the beam will affect final choices.

5.1.3 June 99: Full system architecture device sent for fabrication

Although the first such devices are most likely to be in a radiation-soft technology, they will uncover new problems of scale. This might be the first time that 1 cm x 1 cm or so devices are submitted. The overall interconnection scheme, routing control signals and power to the chips and moving the data from individual elements to the 'ϕ slices' sub-units, and processing the individual packets of information in a given station needs to be engineered. The method of getting the data off the readout chips and routed to station level ϕ slices must be engineered. The advantages of various interconnect technologies need to be compared (e.g., kapton with traces, fiber optic cables). Then, there is R&D required here on radiation hard fiber optic components (transmitters, fibers and receivers).

5.1.4 Resource Requirements

We are aware that reaching this stage on such an aggressive schedule will require a significant investment of engineering and technical resources. The lab has recently establsihed a pixel R&D effort in which members of BTeV are playing a significant role. We intend to cooperate and assist in this effort.

5.1.5 Final Stages of Development and Procurement

The final stages of development and the desired time frames include:

- Jan 2000: Fix errors, full system architecture
- June 2000: Radiation hard component prototypes
- Early 2001: Full system order of radiation hard components.

5.2 Trigger R&D

5.2.1 Development of Level I Vertex trigger

The Level I vertex trigger is one of the key features of the BTeV detector design. A proposed scheme for the vertex trigger has been worked out in detail by the Penn group in collaboration with D. Husby at Fermilab. The hardware design for this system is described in detail in references [1] and [2] of Section 2. Although we believe that the trigger processor could be built using CPUs and FPGA's that are available today, an intensive R&D program is needed to develop the complete design and test the viabiltity of the system. The R&D effort has two components:

- Simulations
- Hardware prototyping.

Simulation studies of the trigger algorithm are already underway. The pixel hits are generated inside the simulation program MCFast and are then processed by trigger simulation code. These simulations have shown promising results and we are planning to improve them to include more processes that will more accurately reproduce the expected running conditions. We hope to use the simulations to learn more about the performance of the trigger under routine and extreme running conditions and to develop and test fast tracking and vertexing algorithms. Although much of the trigger algorithm testing can be done with simulations, other questions can only be tested in hardware. The design of There are plans a prototype module which will test the fundamentals of the trigger design is already under way, see Fig. 63.

The trigger prototype is a single-board module that implements most of the data paths and processing that will be used in the trigger system. It includes four hit processors, four track/vertex processors, and the merging and switching circuitry that connects them. It has provision for loading data, that can be generated by the simulation program, into the processor through FIFO's.

The prototype will be used to test data flow through the trigger system. It will help in understanding the processing requirements for each trigger stage and in uncovering bottlenecks and latency problems. It will also create an infrastructure that will allow us to move from the prototype through a phased implementation to the final system with minimum effort.

The first running in the C0 hall will be devoted in part to studies of the vertex trigger. We plan to install a minimal vertex detector system consisting of a few stations of vertex detector planes as early as possible in Run II and will begin tests of the vertex trigger in situ. These tests in a low rate environment will nevertheless provide valuable information on the capabilities of the design at a point when modifications will still be possible. In addition, we will begin to see whether we can handle the kinds of backgrounds which occur in actual running.

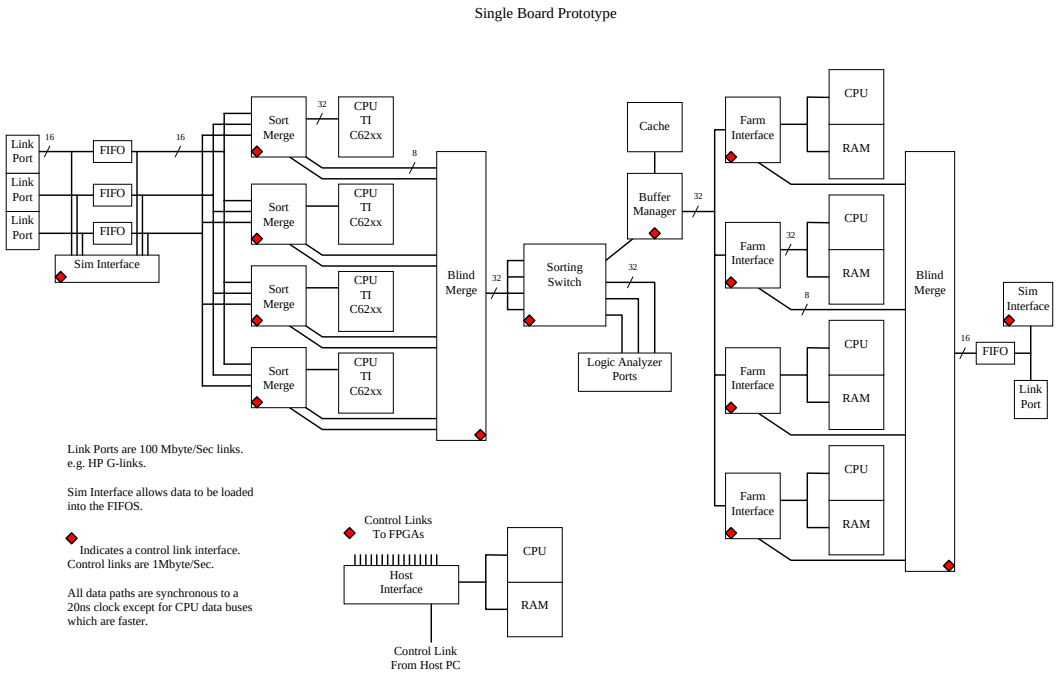

Figure 63: Schematic of Single Board Trigger Prototype

5.2.2 Development of the Level II/III trigger

While the rate and bandwidth requirements at the input to the trigger farm are quite challenging, it is not impossible to build a system operating that will work for the initial running of BTeV with today's technology. Even at the highest luminosities our demands are similar to the LHC-B detector and less than the requirements of the other LHC experiments, Atlas and CMS. Gigabit network technologies such as FibreChannel, Gigabit Ethernet and to some extent ATM can handle transfer rates of 50 - 100 MB/s already today. In a highly parallel system it is hence conceivable to achieve the required throughput of 2 GB/s and more. ATM switches with 96 ports and a total bandwidth of a GB/s can be bought today and in the near future this will increase by a factor of 4. FibreChannel switching fabrics are appearing on the market and will soon meet our bandwidth requirements. A switching network and sophisticated data flow control software are required to assemble the event records at the required rates. This is subject of a major LHC research effort at CERN and we monitor their progress closely. We expect that a solution suitable for BTeV can be derived from this effort.

An estimate of the CPU power requirements can be obtained by scaling from typical fixed target experiments such as FOCUS. On a DEC Alpha computer (200 Specint92) FOCUS fully reconstruct events at a rate of 5 Hz. Assuming a similar reconstruction time for BTeV and an event rate of 3 kHz we need a total processing power in the order of 100,000 SpecInt 92. With the right network infrastructure this can be accomplished cost effectively with a PC based solution

One possible solution for the Level II/III processing farm results from studies undertaken by the PC farms group in the Computing Division. The conceptual design, shown in Fig. 64, consists of a scalable farm of relatively cheap commodity processors, such as the INTEL/Pentium family of processors, running Linux. This solution has not been optimized for BTeV and serves only as starting point for further investigations. An ATM switch receives data at 200-300 MB/s (2-3 kHz of 100 KB events). Current ATM switches provide 24 or 96 input/output ports with total bandwidths of 2.5 Gb/s and 10 Gb/s, respectively. Data leaves the switch and is sent to single CPU "router" processor nodes. These router nodes then pass the data to "worker" nodes along 100 Mb/s fast Ethernet. These worker nodes analyze the data and form the actual Level II trigger decision. Measurements indicate that the router nodes are roughly 25% busy with the data transfers; 5% for the 15 MB/s input ATM transfers and 20% for the 10 MB/s output fast Ethernet transfers. When they identify an idle worker node, they request more data via the ATM switch. If we were doing this today, the worker nodes can be either 2 or 4 CPU INTEL P6's. The number of worker nodes needed depends on the trigger algorithm. Data from events that pass the trigger are collected by a fast Ethernet multiport switch and written to storage at a rate up to 25 MB/s. There are 3 simple yet key features to this proposal: (a) the R&D work is minor since this is work that the PC farms group is already pursuing, (b) the cost of the INTEL solution relative to an equivalent proprietary UNIX workstation solution is today roughly a factor of 3 cheaper, and (c)

the commercial software maintenance costs for the system are minimal due to the freeware being used. Of course, further study must be done to ensure that this is a practical and viable solution. Individual pieces in the design can be upgraded as better devices become available; for example 1 G/s Ethernet can be used when it becomes readily available.

It is the intention of the BTeV collaboration to work with the PC Farms group and the CDF physicists working with them to explore the viability of this approach.

From the Level II/III compute farm the event data are sent to a hierarchical storage system such as IBM's High Performance Storage System, HPSS, or to an event store implemented using an object data base such as Objectivity. Studies and performance measurements done in the Computing Division, at CDF and D0 and at CERN as part of the LHC R&D projects support the feasibility of such a concept. We will work on studies of data storage systems in collaboration with these other groups in order to design the optimal data storage system for BTeV.

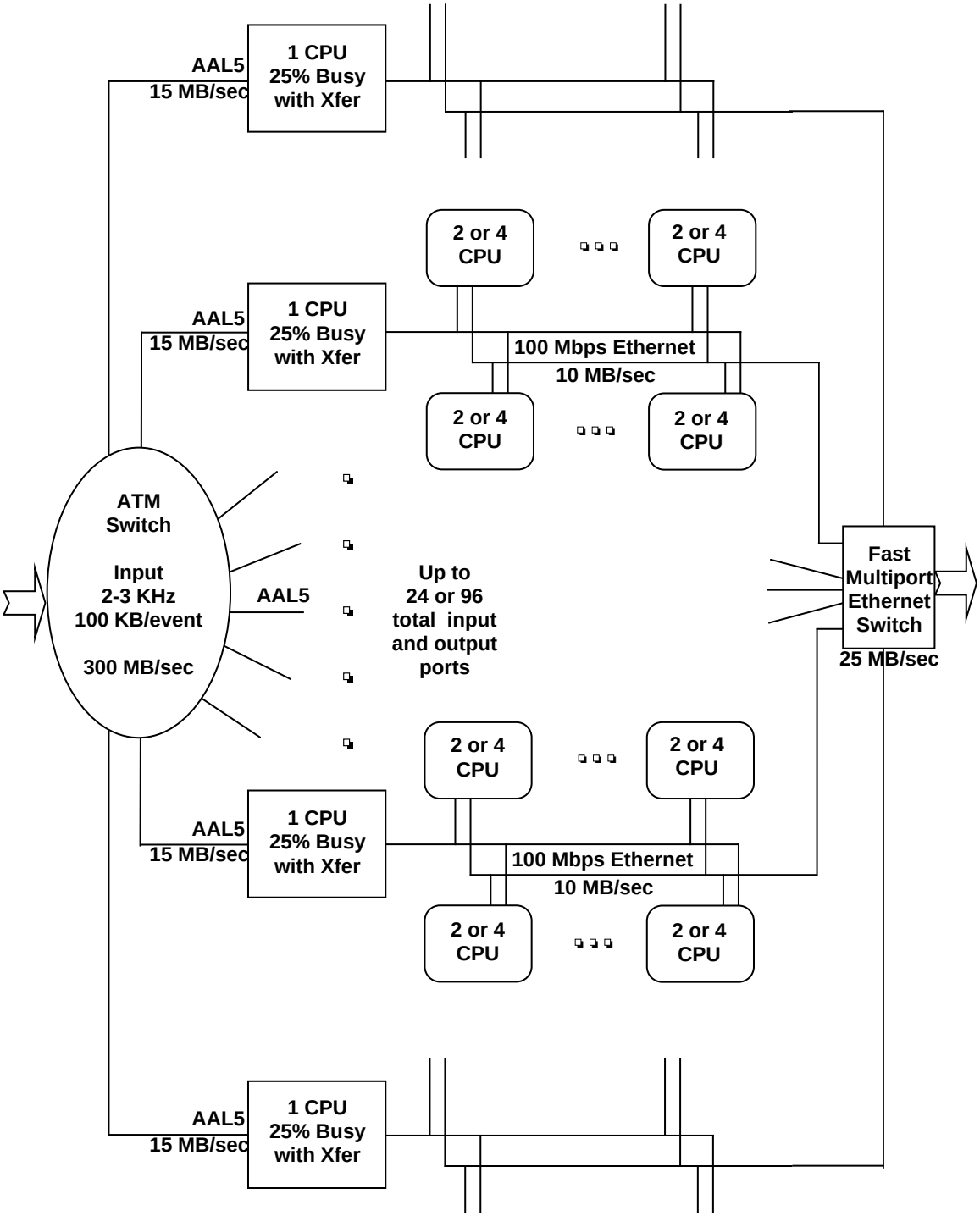

Figure 64: Possible Level II Trigger Architecture for BTeV

5.3 Particle Identification R&D

Particle identification will be based on a mirror focused RICH detector with a gas radiator. An R&D program is needed to select a suitable radiator and photodetection device. Depending on the exact number of detected photo-electrons, the anode size in the multi-anode PMTs from Hamamatsu used in the HERA-B detector might be insufficient. Multipixel hybrid photodiodes such as those being developed for the LHC-B RICH detector offer smaller pixel sizes. Because of the shorter time scale for construction of our experiment and somewhat different detector requirements in the BTEV RICH (larger size) we need to pursue our own R&D in this direction. This should also include studies on the gas radiators. Properties of some gas radiators of interest, like chromatic dispersion, scintillation rate and light transmission are not necessarily well known at the longer wavelengths since most of the previous RICH detectors utilized ultraviolet light. The number of detected photo-electrons with an acceptable chromatic error will be a critical parameter that needs to be demonstrated with a prototype detector.

Even though a single gas radiator like C_4F_{10} can provide π/K separation in a sufficiently large momentum range ($3 - 70$ GeV/c), there are a number of drawbacks of such a system which could be improved to increase the sensitivity of the experiment. One such problem is that there would be no K/p separation at lower momenta (< 9 GeV/c). This necessarily lowers kaon tagging efficiency, since B mesons decay to protons with a rate of about 8%, and these protons, along with protons from b-baryon decay, give false flavor tags. No positive kaon ID below 9 GeV/c could also result in lower kaon efficiency in the busy Tevatron environment. Furthermore, there are some losses of efficiency for two-body B decays like $\pi^+\pi^-$, since the tail of the pion momentum distribution extends beyond 70 GeV/c. Therefore, it will be important to extend the range of positive kaon identification down to about 3 GeV by the use of an additional device. This will not only fix the problems with K/p and K/π separation at lower momenta, but could also allow the possibility of changing the radiator to a gas with a lower index of refraction in order to shift the high end of the momentum coverage upwards to increase the efficiency for rare two-body B decays. Such a gas would also ease requirements for the Cherenkov angle resolution needed to achieve significant K/π separation at 70 GeV/c.

The cost effective solution would be to add an aerogel radiator to the gaseous RICH. There is no experimental proof of this technique, and therefore R&D in this direction is needed. Samples of aerogel with different refractive indices should be acquired from different sources. Light propagation through aerogel should be studied at different wavelengths. This includes transmission measurements and determination of the scattered component. Aerogel quality strongly depends on the details of the production procedure. It is important to establish a reliable source of high quality material. Radiation hardness of the aerogel should be tested. At a later stage of R&D, the aerogel must be tested with the photodetectors in order to match requirements for detection of Cherenkov radiation from both the gaseous and aerogel radiators. Detected Cherenkov photon

yield and Cherenkov angle resolution per photon must be verified.

As a backup option for aerogel as the lower momentum particle identifier we are also considering R&D on ToF and DIRC detectors. Studies of the latter would be mostly concerned with light focusing and photodetection schemes.

6 Personnel, Cost, and Schedule

6.1 Major Tasks

The general features of BTeV have been established: it comprises a two-arm spectrometer with ± 300mr$\times\pm 300$mr acceptance, a pixel detector for high resolution vertex reconstruction, a Level I detached vertex/impact parameter trigger, a RICH, an electromagnetic calorimeter and a muon detector. We have to carry out an ambitious program of optimization studies, R&D, and planning efforts in the next year or two. Simulation is our major tool. Our current simulation has given us a good start but needs to be extended. In the next year, we plan to improve the simulation program to put in more real-world effects to make it more valid. We plan to improve the simulation of the particle identification system and muon system and use the calorimeter simulation to understand whether we have a chance of doing physics that involves π^o's and γ's in the final state. We plan to model more final states. We will also work with the accelerator experts (discussions have already started) to model the background from the machine and its radiation environment in and near the detector.

We need to develop details of the trigger and establish how robust it is with respect to noise, pair conversions, hadronic interactions, and various machine-related backgrounds. We need to study the trigger's ability to deal with beam crossings with multiple interactions. We need to finalize our overall front-end electronics, triggering, and data acquisition systems.

We especially need to optimize the pixel size and arrangement since these have a big impact on the pixel design. Currently we are simulating very small devices (30 μm$\times$300μm) uniformly distributed over the whole area of the pixel planes. We might be able to make them bigger and might gain by varying their size away from the center. By using fewer, larger pixels, we can reduce the overall power consumption and the number of bonds while leaving more area for electronics and more surface to bond to. We need to resolve the importance of pulse height information from the pixels and what range and resolution are required.

Learning how to construct a pixel detector is our most important current effort. We expect that it will take several iterations to develop the type of radiation-hard detector with fast readout that we need. R&D on particle identification is also important.

For all detectors, we need to work to reduce the channel count and complexity without sacrificing physics capability. We also need to begin to understand the mechanical issues associated with constructing, installing, operating, and maintaining these detectors in the C0 Hall.

6.2 Cost and Schedule

6.2.1 Very Preliminary Cost Estimate

At this time it is quite difficult to accurately predict the cost of the two-arm BTeV experiment. However, we make a first estimate based on some assumed

components. These are shown in Table 24.

Table 24: Preliminary BTeV cost estimate ($)

Item	Cost (2 arms)	Cost (1 arm)	comment
Pixels	15 M	15 M	based on CMS and Atlas projections
Trigger Level I	2.5 M	2.5 M	based on 3200 processors
Tracking	3M	1.5M	
RICH	7 M	4 M	based on HERA-B RICH
EM Calorimeter	12 M	6 M	liquid Krypton from NA-48
Muon	2.5 M	1.5 M	based on details in section 2
DAQ+Level II	1.5 M	1.5 M	extrapolated from E831
Infrastructure	5 M	5 M	racks, crates, power supplies, etc...
Off-line computing & data storage	9M	9M	

The total cost of the two-arm system is 57.5 M$, compared with 46 M$ for one arm. We have assumed a liquid Krypton EM calorimeter. If a lead-liquid-Argon system proved to be adequate it would take 9M$ off the two-arm cost.

6.2.2 Schedule

In section 3, we discussed the evolution of the C0 program and in section 5 we presented some details of the R&D plan. Those discussions are summarized in table 25 below.

6.3 Support Required

Simulation has been the key to developing the BTeV design. This will require continuing support of the MCFast effort and will benefit if we are permitted to add one more guest scientist to help with these tasks.

Our plan for BTeV's evolution requires us to make an immediate start on R&D. The pixel R&D has, in fact, already started but must be pursued even more aggressively. Other technologies including trigger and DAQ, particle identification, muon system, and tracking have to be developed and need to begin to address the issues discussed in section 5. The electromagnetic calorimeter is in the earliest conceptual stage and will eventually need some development work.

Our request in calendar 1997 includes $25 k each for trigger/DAQ, particle ID, muon and tracking, a total of $100 k. The pixel effort is undertaken as a lab supported joint R&D project in the Particle Physics Division which will submit its own budget request.

In calendar 1998 we will need to increase the level of funding in these efforts to a total of about $250 k, exclusive of the pixel effort. After the R&D period we will need to begin serious system design and construction at which time we will

need funding and engineering assistance. We would like access (part time) to a mechanical engineer who can help us understand the issues of how we design the mechanical components of the experiment so that they can be installed, supported, and maintained within the C0 hall. We will also need increased electronics engineering support (2 people half time each) for designing the front end electronics (or identifying/specifying commercial options), trigger, and data acquisition system.

6.4 Collaboration structure

We have been asked to describe how the BTeV/C0 collaboration is organized. The collaboration has two elected co-spokespersons, Joel Butler (Fermilab) and Sheldon Stone (Syracuse). The collaboration structure is explained in our goverance document reproduced here:

BTeV GOVERNANCE

1. The collaboration shall be governed by democratic rules and procedures. Leadership will be provided by two elected co-spokespersons. They will be joined by an executive committee which consists of the heads of working groups and standing committees described below. Regular meetings of the full collaboration will be called by the co-spokespersons.

   (a) Procedures for choosing co-spokespersons

      i. The co-spokespersons will be chosen in an election to be held every two years.

   (b) Formal votes

      i. The outcome of votes shall be determined by a simple majority of those voting.

      ii. When votes are proposed at a collaboration meeting, if 10% of those present wish it to be so, a formal e-mail vote by the entire collaboration will be required.

   (c) Procedures for working groups and committees

      i. Working groups and committees will focus the work of the collaboration. The co-spokespersons shall be responsible for establishling working groups and committees and determining their durations. This will be done in consultation with the executive committee.

      ii. Working group heads are responsible to the collaboration for insuring that the group's assigned tasks are completed. They can recruit collaboration members as needed.

      iii. All collaboration members are free to serve on working groups.

      iv. Initially, the following working groups will exist:
      Tracking, Physics and Simulation, Trigger and DAQ, Particle ID, Muon, EM Calorimeter, Detector integration and Interaction Region.

v. There will also be committees which differ from working groups in that their membership will be defined by the committee chair in conjunction with the co-spokespersons and executive committee.

vi. In addition to the executive committee, there will be a membership committee.

2. Initial membership in the collaboration consists of the signers of EOI #1 and EOI #2 and a few other persons who indicated their willingness to join immediately after the C0 workshop in December. The membership list is shown below. All new members must be favorably reviewed by the membership committee and approved by a body widely representative of the collaboration (initially, the executive committee) and by the full collaboration. The rules for membership will be proposed by the membership committee and approved by the collaboration.

3. This document is intended only as a beginning to allow getting started. It is expected that it will be amended as the collaboration grows and the experiment advances.

Table 25: Proposed BTeV/C0 Construction/Installation and Operation Schedule

Activity	date	Comment
R&D:		
Pixels: initial Beam Tests Finalize Specifications	 July 1997 June 1998	
Construction/installation and operations:		
MI shutdown starts C0 enclosure construction Install Background/luminosity monitors Wire Target installation Prototype tracking & Muon chambers Initial test Running Single arm completion (downstream tracking, RICH, EM cal, muon) initial physics run low-β quad installation first $p\bar{p}$ collisions begin installation of part of final pixel detector install second arm muon detector & downstream tracker complete BTeV installlation (2nd RICH/EM cal) First full BTeV collider run	Sept. 15, 1997 completed Oct. 1998 June 1999 June 1999 Sept 1999 Spring 2000 Dec 2000 early 2001 first half 2001 Second half 2001 2002 2002/3 2002 2003 2003-2004	 Includes Magnet and muon steel with microstrip vertex detector for tests sooner if possible partial z coverage